Resonance Parameters from Lattice QCD

by Dehua Guo

B.S. in Physics, June 2011, Huazhong University of Science and Technology

A Dissertation submitted to

The Faculty of
The Columbian College of Arts and Sciences
of The George Washington University
in partial fulfillment of the requirements
for the degree of Doctor of Philosophy

May 20, 2018

Dissertation directed by

Andrei Alexandru
Associate Professor of Physics

The Columbian College of Arts and Sciences of The George Washington University certifies that Dehua Guo has passed the Final Examination for the degree of Doctor of Philosophy as of January 26, 2018. This is the final and approved form of the dissertation.

Resonance Parameters from Lattice QCD

Dehua Guo

Dissertation Research Committee:

Andrei Alexandru, Associate Professor of Physics, Dissertation Director

Frank Lee, Professor of Physics, Committee Member

Michael Doering, Assistant Professor of Physics, Committee Member

Dedicated to my friend,
Jing Ma,
my "son",
Beta
and my parents.

Abstract

Resonance Parameters from Lattice QCD

Hadron-hadron scattering has long served as a tool to investigate the structure and interactions of hadrons and ultimately to understand the nature of the strong force. A large experimental program is dedicated to mapping hadronic resonances. On the theory side, quantum chromodynamics (QCD) which describes the strong interactions of quarks and gluons, is believed to accurately describe all relevant dynamics. Lattice QCD, a non-perturbative formulation, can be used to investigate hadronic physics in terms of quarks and gluons, but only recently it has become possible to use it to extract scattering parameters.

In this work, we use lattice QCD to compute the resonance parameters of ρ and σ mesons. We perform a high-precision calculation of the phase shifts for π-π scattering in the $I = 1$, $J = 1$ and $I = 0$, $J = 0$ channels in the elastic region using elongated lattices with two different pion mass corresponding to $m_\pi = 226\,\text{MeV}$ and $m_\pi = 315\,\text{MeV}$. To finely tune the momentum of the two pions state to map out the resonances accurately, we use both the elongated-box method which adjusts the length of the elongated direction and the boosted-frame method. To determine the resonance parameters, we compute the scattering phase shifts from the two-pion spectrum using Lüscher's formula.

In this work, we employed nHYP-smeared clover fermions with mass-degenerate quark flavors ($N_f = 2$). We parameterize the ρ resonance phase shifts using a Breit-Wigner form and a model from unitarized chiral perturbation theory (UχPT) at two different quark masses and perform an extrapolation to the physical point. We find that the extrapolated value, $m_\rho = 720(1)(15)\,\text{MeV}$, is significantly lower that the physical result and we find evidence that this this shift could be due to the absence of the strange quark in our calculation. The σ resonance is parameterized using UχPT and a

conformal mapping parametrization. The pole for σ-resonance in the parametrization provided by UχPT extrapolated to the physical point is $m_\sigma = (440^{+10}_{-16} - i240^{+20}_{-20})\,\text{MeV}$. This agrees well with estimates in the Particle Data Book based on the analysis of the experimental data. Our results are also compatible with other lattice QCD extractions.

Table of Contents

List of Figures

List of Tables

1 Introduction

1.1 QCD Overview

There are four types of fundamental interactions: gravitational, electromagnetic, strong and weak. All of them are understood as the dynamics of fields. The theory that describes the electromagnetic, strong and weak interactions in subatomic particles is called the Standard Model. This is a theory that combines relativity and quantum mechanics, and describes all observables using a collection of fundamental fields. These fields are the matter fields (quarks and leptons) which are fermionic, and interaction fields (photons, gluons, W and Z bosons) which are bosonic; both electroweak and strong interactions are introduced using gauge theories. There are six leptons and six quarks arranged in three families that are identical in most respects except for their masses. This hints to a further substructure but currently there is no theory that explains this regularity adequately. The dynamics of hadrons is in large part determined by the strong force, with small corrections induced by the electroweak interactions. To a very good approximation the hadrons' spectrum and their interactions can be determined neglecting the electroweak forces and we will do so in this study.

Quantum chromodynamics (QCD) is the generally accepted theory describing the strong interactions between quarks and gluons that make up hadrons. The fundamental degree of freedom of QCD are quarks and gluons. The quarks come in six flavors: up, down, strange, charm, bottom and top. As far as QCD is concerned, the flavors are identical differing only by mass. The Lagrange density of QCD is

$$\mathcal{L}_{QCD} = -\frac{1}{2}\operatorname{Tr} F_{\mu\nu}F^{\mu\nu} - \sum_f \bar{\psi}_f \gamma^\mu \left[\partial_\mu - igA_\mu\right]\psi_f - \sum_f m_f \bar{\psi}_f \psi_f\,, \qquad (1.1)$$

where $F_{\mu\nu} = \partial_\mu A_\nu - \partial_\nu A_\mu + ig[A_\mu, A_\nu]$ is the field strength tensor, $\bar{\psi}_f$ and ψ_f are antiquark and quark fields, A_μ is a gauge field, g is the coupling, m_f is the mass of the

quark, and f is the flavor index. In QCD the gauge field A_μ has values in the $su(3)$ Lie algebra associated with the gauge group $SU(3)$. The quark fields transform under the fundamental representation of the group and the gauge field under the adjoint representation. The charge associated with the gauge group is called color and the basis for the three-dimensional fundamental representation is usually labeled using the primary colors (red, blue and green). Due to the non-abelian structure of the gauge group, the force carriers, the eight types of gluons corresponding to the generators of $SU(3)$, are charged and interact directly with one another.

There are only a few parameters in QCD: the gauge coupling constant g and the quark masses m_f for each flavor. Note that the gauge coupling is scale-dependent, that is, it depends on the energy scale of the experiment used to define the coupling. One important feature of QCD is *asymptotic freedom* - the fact that the coupling constant becomes small at high energies and vanishes in the ultraviolet limit. At very high momentum the coupling constant goes as

$$\alpha_s(Q) = \frac{c_0}{\log(Q/\Lambda_{QCD})} + ... , \qquad (1.2)$$

where c_0 is a constant and Λ_{QCD} is an energy scale. This behaviour of the strong coupling has been verified in high-energy experiments to very high precision, as shown in Fig. 1.1, where Q represents the momentum transfer. This leads to approximative scaling in high-energy scattering and it also enables the use of perturbative methods to estimate the cross sections for energetic collisions. This peculiar behavior of the coupling constant is due to the anti-screening of color charges, which in turn is due to the contribution of gluons to the vacuum polarization.

On the other hand, the coupling constant becomes strong at low energies. Since the coupling constant depends on the energy scale, the overall scale of the theory can be set either by specifying the renormalized coupling at a given energy or by
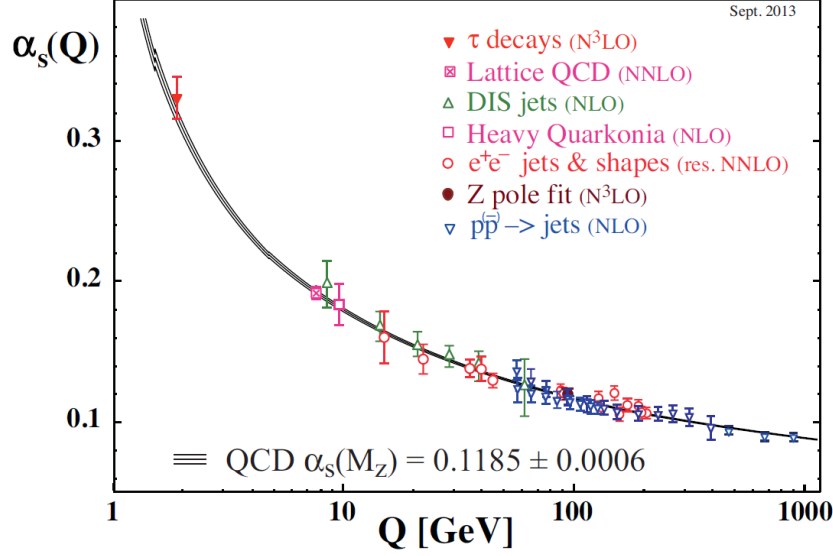
Figure 1.1: The running of coupling constant α_s as a function of momentum transfer.

indicating the energy scale where the coupling becomes strong. This latter parameter is denoted by Λ_{QCD} and its value is about 200–300 MeV (the precise value depends on the definition). This is the scale where non-perturbative effects become important. At this scale, the hadronic scale, the interaction becomes very strong and the quarks and gluons become *confined* which leads to another important feature of QCD called *quark confinement*. Experimentally this is signaled by the lack of colored states: no free quarks or gluons have been observed. All states observed experimentally are color neutral. From a quark model point of view, they are either mesons (quark-anti-quark states) or baryons (states with three valence quarks). This can be understood using the *static quark* potential which shows the energy of a static quark-antiquark pair. The static quark potential as a function of distance r between quark and anti-quark is well described by the Cornell potential:

$$V(r) = A + B/r + \sigma r \,, \tag{1.3}$$

where A is an irrelevant constant determined by the normalization condition. The
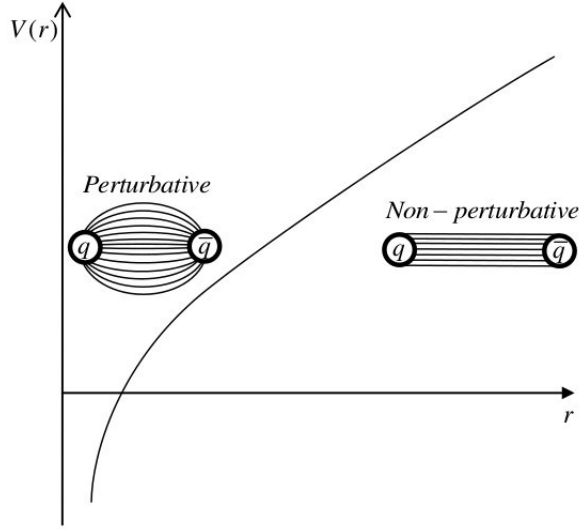
Figure 1.2: A schematic representation of static quark potential.

second term represents the Coulomb part of the interaction between color charges. The last term is linear in r and contributes to the confining part of the potential that is controlled by the so called *string tension* parameter σ. Fig. 1.2 is a schematic representation of the static quark potential in short and long distance. For short distances between quarks, the Coulomb term dominates the interaction. As the distance between quark and anti-quark increases, the linear term in the potential becomes larger. When $r > 1\,\mathrm{fm}$, the energy of the quark-antiquark pair increases linearly with the distance. If we keep increasing the distance so that the energy is large enough, it is more favorable to create a new quark-antiquark pair which forms a mesonic bound state. This is an efficient parameterization of observation for why all states observed from experiment are color neutral.

Another important feature of QCD is the *spontaneous breaking of chiral symmetry*. From the QCD Lagrangian listed in Eq. 1.1, one can show that if the quarks are massless, the QCD Lagrangian is invariant under a chiral transformation

$$\psi \rightarrow \psi' = e^{i\alpha\gamma_5}\psi\,, \quad \overline{\psi} \rightarrow \overline{\psi}' = \overline{\psi}e^{-i\alpha\gamma_5}\,. \tag{1.4}$$

4

However, the lowest energy state of QCD which is called QCD vacuum is not invariant under the chiral transformation. This is due to the fact that there is a chiral condensate (a non-vanishing vacuum expectation value for the quark-antiquark pair) in QCD. As a result, the chiral symmetry group of QCD vacuum is different from the chiral symmetry group of the QCD Lagrangian which leads to the spontaneous chiral symmetry breaking. In a theory with $SU(2)_L \times SU(2)_R$ chiral symmetry where we only consider u and d quarks, this leads to three massless particles (the *Goldstone bosons*) which correspond to π^+, π^-, π^0. In fact, the quarks are massive in Nature. The lightest quarks u and d have a mass about $5\,\mathrm{MeV}$ which is much smaller that the hadronic scale. The non-zero mass of the quarks explicitly breaks the chiral symmetry of the Lagrangian and gives masses to the three pions.

1.2 Lattice QCD overview

Due to asymptotic freedom, the coupling is small at high energies and perturbative methods can be used to explore QCD properties. At low energies, relevant for hadronic physics, this is no longer possible. Non-perturbative methods like chiral perturbation theory or lattice QCD are required. In this work we will use lattice QCD to determine hadrons' properties directly in terms of the quark-gluon interactions. We will discuss the lattice formulation of QCD in detail in Chapter 2.

Typical lattice QCD calculations relevant for nuclear physics use either two mass-degenerate quark flavors ($N_f = 2$) corresponding to u and d quarks or they also include the strange quark flavor ($N_f = 2 + 1$). The heavy quarks—charm, bottom, and top—produce only tiny corrections for nuclear physics and they can be safely disregarded. We point out here that while in Nature the up and down flavors are not mass-degenerate (isospin symmetry is explicitly broken) the leading corrections due to this mass difference are of the order $(m_u - m_d)/\Lambda_{QCD}$, usually smaller than the precision of our calculations. In this work we use $N_f = 2$ simulations: the theory is

simpler in this case with fewer open channels for the resonances, making our analysis easier. By comparing our results with experimental ones and with $N_f = 2+1$ lattice QCD calculations, we can gauge the importance of the strange quarks in determining the resonance properties.

1.3 Hadron scattering

We obtain information about the hadrons' strong interaction dynamics through scattering experiments. However, the vast majority of hadronic states produced in collisions are not stable. As a result, the intermediate particles, so called resonances, do not live long enough to reach and interact with particle detectors. In this case, one has to measure the dynamical enhancement of scattering amplitudes of their decay products after scattering. Collecting the result of the scattering event gives us insight into the underlying dynamics.

In order to test the validity of QCD and its predictive power, one should compute scattering observables from QCD so that they can be compared with the experimental results. In lattice QCD, scattering observables such as phase shifts cannot be computed directly. We need some method to relate the energy spectrum computed from lattice QCD to phase shifts. The details are discussed in Chapter 4. In this study, we are interested in the elastic scattering of two pions in the $I(J^{PC}) = 1(1^{--})$ and $I(J^{PC}) = 0(0^{++})$ channel.

1.3.1 The $\rho(770)$ meson

My first project focused on the $\rho(770)$ resonance which is the the lowest resonance in the $I(J^{PC}) = 1(1^{--})$ two-pion scattering channel. Its mass m_ρ and decay width Γ are well determined from several scattering experiments. For example, its properties can be extracted from the $e^+ e^- \to \pi^+ \pi^-$ reaction, schematically shown in Fig. 1.3, by computing the form factor for the pion from the cross section and fitting it to
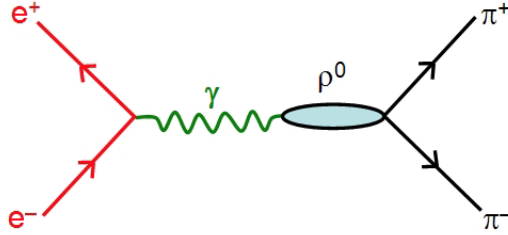
Figure 1.3: $e^+e^- \to \pi^+\pi^-$ reaction.

a model [5]. The mass m_ρ and decay width Γ have values of $775.26(25)\,\text{MeV}$ and $147.8(9)\,\text{MeV}$ [6],respectively.

The ρ resonance was the subject of a number of lattice QCD calculations [7–18], with the results for phase shifts becoming more and more precise and the quark masses getting closer to the physical point. In this study, we use elongated boxes and extract phase shifts both for zero-momentum states and for boosted states, i.e., states with a moving center-of-mass, so that we can finely scan the phase shift pattern around the resonance region. This study extends a previous calculation of our group [11] by adding a larger base of interpolator fields and a set of ensembles at lower pion masses. Using two different quark masses allows us to extrapolate to the physical point.

1.3.2 The σ-meson

The σ-meson is the most controversial light meson since several decades ago because of its mass uncertainties and with a decay width comparable to its mass. It has been listed in the Review of Particle physics, which considered it as a "well-established" state despite quoting its mass in a range between $400\,\text{MeV}$ and $1200\,\text{MeV}$. The σ is the lightest scalar-isoscalar meson coupling strongly to π-π. It plays a very important role in the dynamics of the QCD spontaneous chiral symmetry breaking because it is related to the chiral condensate which is studied with different model such as the Linear Sigma Model proposed by Gell-Mann and Levy [19] in 1960. Therefore, the existence and the properties of the σ are very relevant for the understanding of the
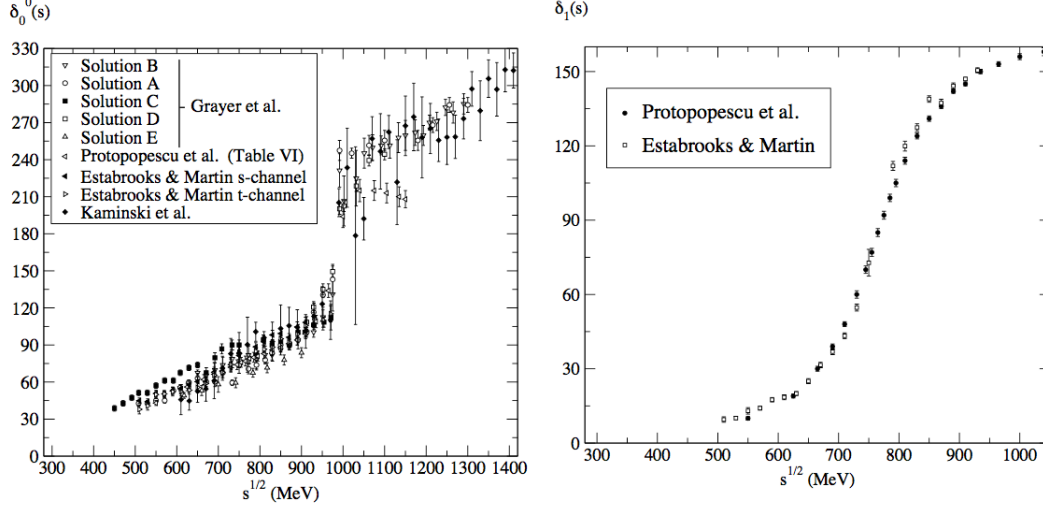
Figure 1.4: Experimental data on $\pi\pi \to \pi\pi$ scattering phase shifts from Ref. [1]. Left panel: The scalar-isoscalare phase shifts. Right panel: vector-isovector phase shifts.

nucleon-nucleon attraction and chiral symmetry in strong interactions. Unlike other mesons, the identification and determination of the σ-meson parameters is hindered by its large decay width and unusual shape as can be seen from Fig. 1.4 which shows the phase shifts comparison between the scalar-isoscalar and vector-isovector two-pion scattering channels. The familiar Breit-Wigner description which is valid for narrow isolated resonances is not appropriate for the σ-meson. A process-independent and mathematically-sound definition of a resonance is made by means of its associated pole of the T-matrix in the unphysical Riemann sheet of the complex energy plane as $\sqrt{s_R} = M_R - i\Gamma_R/2$.

The composition of the σ-meson is also controversial because the σ is not an ordinary meson in the sense that it cannot be interpreted as predominantly made of a quark and an antiquark. Besides the quark-antiquark, meson-meson components, models were proposed that describe it in terms of so called tetraquarks, combinations of diquark anti-diquark states that form almost bound color-neutral states. The various possible components of the σ make the lattice calculation quite challenging. There are several lattice QCD calculations [3, 20–24] relevant for the σ-meson: A

recent study used a large ensemble of small lattices to gauge the importance of the tetraquark interpolators for the isoscalar channel [24]. In another recent study, a variational analysis was performed that included both quark-antiquark and meson-meson interpolators, and the pole-position for σ was extracted [3]. In this study, we apply similar methods as we used for the ρ resonance in order to extract the energy spectrum and use a UχPT model to compute the resonance parameters at two pion masses and to perform an extrapolation to the physical point.

1.4   Dissertation outline

In this dissertation we present the relevant lattice QCD details and the techniques we used to determine the resonance parameters for the ρ and σ mesons. The plan of the presentation is the following:

- In chapter 2, we include an overview of lattice QCD. In section 2.1, we discuss the *Euclidean path integral* formulation and how to compute the basic quantities of interest. In sections 2.2 and 2.3, we explain in detail the lattice formulation of the QCD action and its improvement we use in this work. In section 2.4, we discuss the numerical aspects of simulating an $SU(3)$ gauge theory.

- In chapter 3, we introduce the lattice QCD techniques used for hadron spectroscopy. In section 3.1, we show how to extract energies for QCD states using two-point correlators. In section 3.2, we discuss the symmetry properties on the lattice and their role in hadron spectroscopy. In section 3.4, we illustrate the *variational method* that is used to extract excited state energies. In section 3.3, we introduce the *Laplacian Heaviside smearing* method which enables efficient calculations of a broad range of hadron correlation functions. In section 3.5, we cover fitting and statistical analysis we use in our work.

- In chapter 4, we show how to use lattice data to extract resonance information.

In section 4.1, we discuss the general relations between the energy spectrum of two-particle states in finite volume and the physically-observable phase shifts. In section 4.2, we demonstrate how to apply this relation to the $I(J^{PC}) = 1(1^{--})$ and $I(J^{PC}) = 0(0^{++})$ channels. In section 4.3, we discuss how to extract resonance information from parametrizations of the phase shifts. In section 4.4, we present the numerical procedure we used to carry out the calculation.

- In chapter 5, we present the results of our simulations. In section 5.1, we include the details of the ensembles used in this study. In section 5.2, we discuss the energy spectrum and resonance parameters for the ρ resonance, analyze the $K\overline{K}$ contributions, and compare our results with lattice calculations reported by other groups. In section 5.3, we present the results for the σ resonance including the energy levels extracted from our simulations, the model fits and the extraction of the pole mass, and the extrapolation of the pole mass to the physical point.

2   Introduction to Lattice QCD

Due to asymptotic freedom the effective coupling constant of QCD becomes small at short distances and the theoretical prediction based on perturbation theory can be compared to results from experiments. However, perturbation theory breaks down when the coupling constant becomes strong at low energies (or long distances) relevant for hadron physics. Therefore, non-perturbative methods are needed to calculate the quantities that are sensitive to long distance behavior of QCD. Lattice QCD, formulated in 1974 by Kenneth Wilson [25], is currently the only non-perturbative approach to QCD that allows calculation of hadron properties directly in terms of quark and gluon dynamics. In this formulation a space-time lattice is introduced to regularize QCD and the Feynman path-integral turns into an ordinary, albeit high-dimensional, integral which can be evaluated by numerical means.

In this chapter, we will present a brief introduction to the lattice QCD methods we use to calculate the resonance parameters. The discussion here is somewhat abbreviated; the reader interested in more details is referred to the textbooks written on this topic [26–29]. We start by presenting the Euclidean path integral formulation for quantum field theories in section 2.1. In section 2.2, we introduce the lattice as a regulator for QCD, discuss its continuum limit, and cover the gauge fields and fermion fields discretization. In section 2.3 we discuss the improved actions used in our work. Finally, in section 2.4 we will present sampling methods used to estimate observables in lattice QCD simulations.

2.1   Euclidean path integral formulation

The starting point of lattice formulation for quantum field theory is the path integral approach which was first proposed in 1933 by P.A.M. Dirac [30] and developed by Richard Feynman in the late 1940's. The discussion of the path integral method in the context of quantum mechanics can be found in the book by Feynman and

Hibbs [31], and a good illustration of the derivation for the path integral formulation for quantum field theories can be found in Ref. [26]. In quantum field theories, all physical information can be extracted from the n-point correlation functions:

$$\langle\Omega|\,T[\mathcal{O}_1(x_1)...\mathcal{O}_n(x_n)]\,|\Omega\rangle\,, \tag{2.1}$$

where the $|\Omega\rangle$ represents the vacuum state and $\mathcal{O}_i$ are Heisenberg picture operators with $x_i = (t_i, \boldsymbol{x}_i)$. T is the time ordering for the product of operators $\mathcal{O}_i$ in descending time from left to right. One concrete example is the two-point correlation function which we will use to compute the spectrum of QCD. For numerical evaluation convenience, we use *Euclidean time* for the path integral representation, formally derived by performing a Wick rotation that replaces the real time with imaginary time $(t \rightarrow -it_E)$. The Euclidean two-point correlation function in the Euclidean path integral representation is written as:

$$\langle\Omega|\,\mathcal{O}_1(x_1)\mathcal{O}_2(x_2)\,|\Omega\rangle = \lim_{T\to\infty}\frac{1}{Z}\,\mathrm{Tr}[e^{-(T-t)H}\mathcal{O}_1(\boldsymbol{x}_1)e^{-tH}\mathcal{O}_2(\boldsymbol{x}_2)]\,, \tag{2.2}$$

where H is the Hamiltonian, $t = t_2 - t_1$, and $Z = \mathrm{Tr}[\exp(-TH)]$. The operators $\mathcal{O}_i(x_i)$ in Heisenberg picture can be related to the operators $\mathcal{O}_i(\boldsymbol{x}_i)$ in the Schrödinger picture by

$$\mathcal{O}(t, \boldsymbol{x}) = e^{-Ht}\mathcal{O}(\boldsymbol{x})e^{Ht}\,. \tag{2.3}$$

The two-point function in Eq. 2.2 can be defined using the path integral formulation. For QCD we have:

$$\langle\Omega|\,\mathcal{O}_1(x_1)\mathcal{O}_2(x_2)\,|\Omega\rangle = \lim_{T\to\infty}\frac{1}{Z}\int \mathcal{D}\psi\mathcal{D}\overline{\psi}\mathcal{D}A_\mu\mathcal{O}_1(x_1)\mathcal{O}_2(x_2)e^{-S_{QCD}[\psi,\overline{\psi},A_\mu]}\,, \tag{2.4}$$

with

$$Z = \mathrm{Tr}[e^{-HT}] = \int \mathcal{D}\psi\mathcal{D}\overline{\psi}\mathcal{D}A_\mu e^{-S_{QCD}}\,. \tag{2.5}$$

12

On the right hand side of the equation above ψ and A are classical fields and $\mathcal{O}_i(x_i)$ are composite objects of ψ and A called *interpolating fields*. ψ denotes the quark fields and the gauge fields A are elements of the $SU(3)$ Lie algebra.

The expression in Eq. 2.4 is formally equivalent with a statistical mechanics system in four dimensions with $\exp[-S_{QCD}]$ playing the role of the Boltzmann factor. The two-point function can then be evaluated as the average over fluctuating ψ and A fields. As we will see in the next section, the QCD action S_{QCD} can be separated in a pure-gauge action and a fermionic part:

$$S_{QCD} = \sum_f S_f + S_g \,, \tag{2.6}$$

where S_f represents the contribution from the fermions for the flavor f and S_g denotes the gauge contribution to the action. The details about the QCD action are discussed in section 2.2. The fermionic contribution is quadratic in ψ, that is we can write $S_f = \bar{\psi}_f M_f \psi_f$, and we can integrate the fermionic fields out. If we denote the average over fermionic field fluctuations with

$$\langle \mathcal{O} \rangle_F \equiv \frac{1}{Z_F(A)} \int \mathcal{D}\psi \mathcal{D}\bar{\psi} e^{-S_F[\psi,\bar{\psi},A]} \mathcal{O}[\psi,\bar{\psi},A] \,, \tag{2.7}$$

with the *ferminonic determinant*

$$Z_F[A] = \int \mathcal{D}\psi \mathcal{D}\bar{\psi} e^{-S_F[\psi,\bar{\psi},A]} = \prod_f \det M_f \,, \tag{2.8}$$

and the average over the gauge fields

$$\langle \mathcal{O} \rangle_G \equiv \frac{1}{Z} \int \mathcal{D}A_\mu e^{-S_g[A]} Z_F[A] \mathcal{O}[A] \,, \tag{2.9}$$

we can write the full average as $\langle O \rangle = \langle \langle O \rangle_F \rangle_G$.

2.2 Lattice QCD action

2.2.1 Fermion action

In this section we will discuss the lattice discretization for the fermion action. We first introduce a four-dimensional space-time grid: The fields on the lattice are sampled at

$$x_\mu = a n_\mu \quad \text{with} \quad n_\mu \in \mathbb{Z} \,, \tag{2.10}$$

where a is the lattice spacing. Due to the discretization, the momentum is restrained to a finite range, the Brillouin zone (BZ):

$$-\frac{\pi}{a} \leq p_\mu \leq \frac{\pi}{a} \,. \tag{2.11}$$

The maximum momentum one can achieve on the lattice is $\frac{\pi}{a}$. As a result, the lattice structure automatically introduces an ultraviolet (UV) cutoff $\Lambda = \frac{\pi}{a}$ that serves as a regulator. Physical results are recovered in the *continuum limit*: $a \to 0$. To make sure that a lattice discretization is correct we need to check that the discretized action converges to the continuum action when $a \to 0$ for smooth gauge fields (the naive continuum limit) and that the quantum corrections do not spoil the limit.

To illustrate the discretization procedure let us first consider the Dirac equation in Minkowski space

$$(i\gamma^\mu \partial_\mu - m)\psi(x) = 0 \,, \tag{2.12}$$

where γ_μ are 4×4 Dirac matrices satisfying the anti-commutation relations

$$\{\gamma^\mu, \gamma^\nu\} = 2g^{\mu\nu} \,, \tag{2.13}$$

and ψ is a 4-component field. The equation of motion for ψ and $\overline{\psi}$ follow from the

action

$$S_f[\psi,\overline{\psi}] = \int d^4x \overline{\psi}(x)(i\gamma^\mu \partial_\mu - m)\psi(x)\,. \tag{2.14}$$

To get the Eulidean action, we perform the Wick rotation. Using $\gamma_4^E = \gamma_0, \gamma_i^E = -i\gamma^i$, (with anti-commutation relations $\{\gamma_\mu^E, \gamma_\nu^E\} = 2\delta_{\mu\nu}$), the Euclidean action can be written as

$$S_f^E = \int d^4x \overline{\psi}(x)(\gamma_\mu^E \partial_\mu + m)\psi(x). \tag{2.15}$$

Since we will use Euclidean time throughout this work, we drop the E symbols for convenience.

To write the discretized action, we introduce dimensionless lattice variables, by scaling $M, \psi, \overline{\psi}$ with a according to their canonical dimensions with the replacements as following:

$$
\begin{aligned}
m &\to \frac{1}{a}\hat{m}\,, \\
\psi(x) &\to \frac{1}{a^{\frac{3}{2}}}\hat{\psi}(n)\,, \\
\overline{\psi}(x) &\to \frac{1}{a^{\frac{3}{2}}}\overline{\hat{\psi}}(n)\,, \\
\partial_\mu \psi &\to \frac{1}{2}[\nabla_\mu + \nabla_\mu^*]\hat{\psi}\,.
\end{aligned}
\tag{2.16}
$$

Above $(\nabla_\mu \hat{\psi})(n) \equiv \hat{\psi}(n+\hat{\mu}) - \hat{\psi}(n)$ is the forward derivative and $\nabla_\mu^* = -(\nabla_\mu)^\dagger$ is the backward derivative. With these replacements, Eq. 2.14 can be rewritten as

$$S_f = \sum_{n,m,\alpha,\beta,a,b} \overline{\hat{\psi}}_\alpha^a(n) M_{a\alpha,\beta b}(n,m)\hat{\psi}_\beta^b(m)\,, \tag{2.17}$$

where

$$M_{\alpha\beta}(n,m) = \sum_\mu \frac{1}{2}(\gamma_\mu)_{\alpha\beta}[\delta_{m,n+\hat{\mu}} - \delta_{m,n-\hat{\mu}}] + \hat{m}\delta_{mn}\delta_{\alpha\beta}\,, \tag{2.18}$$

α, β are the spinor indexes, a, b label color and n, m label the positions. For convenience,

Eq. 2.17 can be written in matrix form as

$$S_f = \sum_{m,n} \overline{\hat{\psi}}(n) M(n,m) \hat{\psi}(m) \,. \tag{2.19}$$

According to Wick's theorem, the discrete version of the two-point correlation can be calculated as

$$\left\langle \hat{\psi}(n) \overline{\hat{\psi}}(m) \right\rangle_F = M^{-1}(n,m) \,. \tag{2.20}$$

With this fermion action, the two-point correlation function for the free fermionic fields in the continuum is given by

$$\left\langle \psi(x) \overline{\psi}(y) \right\rangle = \lim_{a \to 0} \frac{1}{a^3} \left\langle \hat{\psi}(x) \overline{\hat{\psi}}(y) \right\rangle = \lim_{a \to 0} \int_{-\frac{\pi}{a}}^{\frac{\pi}{a}} \frac{d^4 p}{(2\pi)^4} \frac{\left[-i \sum_\mu \gamma_\mu \tilde{p}_\mu + m \right]}{\sum_\mu \tilde{p}_\mu^2 + m^2} e^{-ip(x-y)} \,, \tag{2.21}$$

where $\tilde{p}_\mu = \frac{1}{a} \sin(a p_\mu)$. The factor $1/a^3$ arises from scaling the fields according to Eq. 2.16. The details of the derivation can be found in Ref. [26]. In Eq. 2.21, the integration is over the Brillouin zone. When $m = 0$ the integrand has poles for $p = 0$, but also at the edges of the Brillouin zone at $p = \pi/a$ for every direction, which do not disappear as we take the continuum limit; these additional poles correspond to additional fermion species. This is the so called "fermion doubling" problem.

One of the solutions to deal with the doubling problem was proposed by Wilson [32]. He modified the action by adding a term which vanishes in the naive continuum limit but it is not invariant under chiral transformations. The modified action can be written in the form

$$S_f^W = S_f - \frac{r}{2} \sum_n \overline{\hat{\psi}}(n) \hat{\Box} \hat{\psi}(n) \,, \tag{2.22}$$

where r is the Wilson parameter, and $\hat{\Box} = \nabla_\mu \nabla_\mu^*$ is the four-dimensional lattice

Laplacian operator

$$\hat{\Box}\hat{\psi}(n) = \sum_{\mu}(\hat{\psi}(n - \hat{\mu}) + \hat{\psi}(n + \hat{\mu}) - 2\hat{\psi}(n)). \tag{2.23}$$

The two-point correlation function has the same form as Eq. 2.21 with the replacement

$$m \to m(p) = m + \frac{2r}{a}\sum_{\mu}\sin^2(\frac{p_\mu a}{2})\,. \tag{2.24}$$

$m(p)$ approaches m when $a \to 0$ for $p = 0$ but near the edge of the BZ $m(p)$ diverges, making the additional fermion species dynamically irrelevant. The fermion doubling problem is solved at the expense of the breaking the chiral symmetry of the original action in Eq. 2.17 which makes this scheme less attractive for studying the questions related to spontaneously chiral symmetry breaking in QCD.

2.2.2 Gluon action

In this section, we discuss the action for the gluon field in QCD. It is convenient to split the QCD action into a fermionic part which includes quark fields and an interaction term coupling them to the gluons, and a gluonic part that describes the propagation and interaction of only the gluons. A detailed explanation can be found in Ref. [27]. In QCD, the action is invariant under the local gauge transformation:

$$A_\mu(x) \to A'_\mu(x) = \Omega(x)A_\mu(x)\Omega(x)^\dagger + i\Omega(x)\partial_\mu\Omega(x)^\dagger\,,$$
$$\psi(x) \to \psi'(x) = \Omega(x)\psi(x)\,, \tag{2.25}$$
$$\overline{\psi}(x) \to \overline{\psi}'(x) = \overline{\psi}(x)\Omega(x)^\dagger\,.$$

The pure-glue Euclidean action in the continuum is

$$S_g^{\text{cont}} = \frac{1}{2g^2}\int d^4x\,\text{Tr}[F_{\mu\nu}(x)F_{\mu\nu}(x)]\,, \tag{2.26}$$

where g is the coupling strength and $F_{\mu\nu}(x)$ is the field strength tensor defined by

$$F_{\mu\nu}(x) = \partial_\mu A_\nu(x) - \partial_\nu A_\mu(x) - i[A_\mu(x), A_\nu(x)]. \qquad (2.27)$$

For the interaction between fermion and gluon, we introduce the covariant derivative

$$D_\mu = \partial_\mu - iA_\mu(x). \qquad (2.28)$$

The fermion action can be written as

$$S_f = \sum_f \overline{\psi}_f(\slashed{D} + m_f)\psi_f. \qquad (2.29)$$

The next step is to figure out how we can construct the gauge action on the lattice. The mass term in Eq. 2.18 is invariant under the gauge transformation. For the discretized derivative term, this is not the case because the bilinear term under a gauge transformation

$$\overline{\psi}(n)\psi(n+\hat{\mu}) \to \overline{\psi}'(n)\psi'(n+\hat{\mu}) = \overline{\psi}(n)\Omega(n)^\dagger\Omega(n+\hat{\mu})\psi(n+\hat{\mu}) \qquad (2.30)$$

is not invariant. To solve this problem, we introduce a field $U_\mu(n)$ with a directional index μ to the bilinear term

$$\overline{\psi}'(n)U'_\mu(n)\psi'(n+\hat{\mu}) = \overline{\psi}\Omega(n)^\dagger U'_\mu(n)\Omega(n+\hat{\mu})\psi(n+\hat{\mu}). \qquad (2.31)$$

This bilinear becomes gauge invariant if the gauge transformation of U field satisfy the relation

$$U_\mu(n) \to U'_\mu(n) = \Omega(n)U_\mu(n)\Omega(n+\hat{\mu})^\dagger. \qquad (2.32)$$

Since the $U_\mu(n)$ field are oriented and attached to the links of the lattice, they are
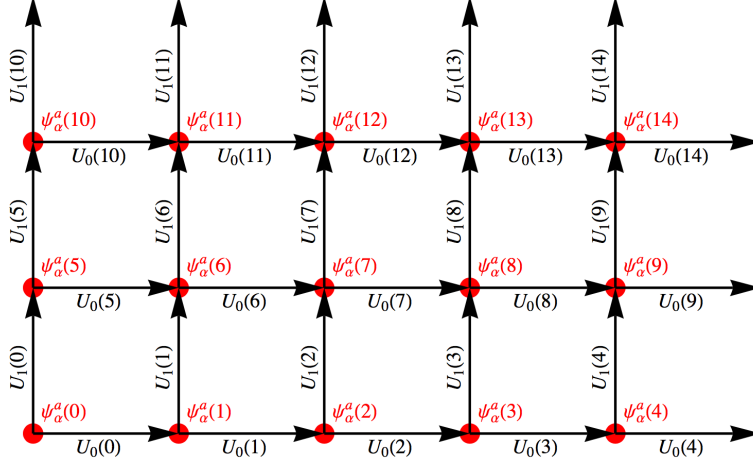
Figure 2.1: A two-dimensional schematic representation of the fermion fields $\psi(n)$ and the gauge links $U_\mu(n)$.

called *link variables* which live on the link and connect the sites n and $n + \hat{\mu}$. The fermions can be thought as living on the sites of the lattice, each of which is represented by a 4×3 spin-color matrix, and the gauge links $U_\mu(n)$ are viewed as the links of the lattice connecting the neighboring sites (see Fig. 2.1). The next step is to relate the link variables to gauge field in the continuum. In the continuum an object with the transformation behaviour as Eq. 2.25 is known. It is the path-ordered exponential integral of the gauge field A_μ along some path $C_{x,y}$ from x to y as

$$G(y, x) = P \exp \left(i \int_{C_{xy}} A \cdot ds \right) , \qquad (2.33)$$

where $G(x, y)$ has the gauge transform behaviour

$$G(y, x) \rightarrow G'(y, x) = \Omega(y)G(y, x)\Omega(x)^\dagger . \qquad (2.34)$$

The transformation properties of $G(y, x)$ are similar to the link variables $U_\mu(n)$. Therefore, we can interpret the link variable $U_\mu(n)$ as a lattice version of the $G(n, n+\hat{\mu})$ connecting the points n and $n + \hat{\mu}$. We introduce the algebra-valued (a function of)

lattice gauge field $A_\mu(n)$ as

$$U_\mu(n) = \exp(-iaA_\mu(n)) \,. \tag{2.35}$$

We can see that there is an approximation of the integral along the path from $n + \hat{\mu}$ to n as $-aA_\mu(n)$ which is good to $\mathcal{O}(a)$. For small a, the link variable becomes

$$U_\mu(n) = \mathbf{1} - iaA_\mu(n) + \mathcal{O}(a^2) \,. \tag{2.36}$$

According to Eq. 2.18, 2.19 and the property of the link variable, we can make the Wilson fermion action locally gauge invariant by inserting the gauge links in between bilinear term as

$$S_f^W = (\hat{m} + 4r) \sum_n \overline{\hat{\psi}}(n)\hat{\psi}(n) \tag{2.37}$$
$$- \frac{1}{2} \sum_{n,\mu} [\overline{\hat{\psi}}(n)(r - \gamma_\mu)U_\mu(n)\hat{\psi}(n + \mu) + \overline{\hat{\psi}}(n + \hat{\mu})(r + \gamma_\mu)U_\mu^\dagger(n)\hat{\psi}(n)] \,.$$

After introducing the link variables on the lattice, we can now construct lattice gauge actions in term of the link variables. To start with, let's introduce the *plaquette* variable which is the product of four link variables defined as

$$U_{\mu\nu}(n) = U_\mu(n)U_\nu(n + \hat{\mu})U_\mu(n + \hat{v})^\dagger U_\nu(n)^\dagger \,. \tag{2.38}$$

One can show that the trace of the plaquette variable is gauge-invariant. The Wilson gauge action is constructed as a sum over all plaquettes, with each plaquette counted with only one orientation:

$$S_g^W[U] = \frac{2}{g^2} \sum_{n \in \Lambda} \sum_{\mu < \nu} \operatorname{Re} \operatorname{Tr}[\mathbf{1} - U_{\mu\nu}(n)] \,. \tag{2.39}$$

20

Now we can check its continuum limit by expanding the link variables in the form of Eq. 2.35 for small a with the help of the Baker-Campbell-Hausdorff formula for the product of exponentials of matrices:

$$\exp(A)\exp(B) = \exp\left(A + B + \frac{1}{2}[A, B] + ...\right),\tag{2.40}$$

together with the Taylor expansion for the gauge field

$$A_\mu(n + \hat{\mu}) = A_\nu(n) + a\partial_\mu A_\nu(n) + \mathcal{O}(a^2).\tag{2.41}$$

The plaquette variable can then be written as

$$U_{\mu\nu}(n) = \exp(-ia^2 F_{\mu\nu}(n) + \mathcal{O}(a^3)).\tag{2.42}$$

Note that the corrections above $\mathcal{O}(a^3)$ have a purely imaginary trace, since $U_{\mu\nu}$ is a unitary matrix. As such when $a \to 0$,

$$\operatorname{Re}\operatorname{Tr} U_{\mu\nu} = \operatorname{Tr} \mathbf{1} - \frac{1}{2}a^4 \operatorname{Tr}[F_{\mu\nu}(n)^2] + \mathcal{O}(a^5),\tag{2.43}$$

and Eq. 2.39 can be simplified as

$$S_g^W = \frac{a^4}{2g^2} \sum_{n\in\Lambda} \sum_{\mu,\nu} \operatorname{Tr}[F_{\mu\nu}(n)^2] + \mathcal{O}(a^5).\tag{2.44}$$

By comparing with Eq. 2.26, the factor a^4 together with the sum over Λ is the discretization of the space-time integral. Therefore the Wilson gauge action is the approximation of the continuum form up to $\mathcal{O}(a)$. The standard Wilson action S_W is then given by

$$S_W = S_f^W + S_g^W,\tag{2.45}$$

21

where S_f^W contains the contribution from all flavors of the fermions and S_g^W denotes the gauge portion of the action. From Eq. 2.37 we can see that each term in the fermionic portion of the action has the form of a Gaussian exponent, therefore, the integral of the fermionic part can be computed analytically. We will discuss how to evaluate numerically the whole integral in section 2.4.

2.3   Improved lattice actions

From the previous section, one can see that the discretization is not unique therefore there is freedom to design some lattice action which can improve the approximation to the continuum form making it approach to the continuum limit faster. Here we review briefly Symanzik improvement program and show how to use it to define an improved fermion action, *clover fermions*, and an improved gauge action, Lüscher-Weisz action.

Additionally, from a numerical point of view, calculations with rough gauge fields are expensive, especially on the fermionic side. One solution to this problem is to use smeared gauge fields in the definition of the fermionic matrix. Here we will present the details for the *nHYP smearing* procedure used in our simulation.

2.3.1   Clover fermions

Wilson fermions have $\mathcal{O}(a)$ discretization errors, which means that the continuum limit is approached linearly. This requires large scale simulations to reliably extract physical results. A significant reduction in the computational cost can be achieved if we reduce the order of the discretization errors. A systematic framework for such improvement was proposed by Symanzik [33]. In this section we will sketch the steps required to develop *clover fermions* that can be tuned to approach the continuum limit quadratically. The strategy is the following:

- Start from a discretized form for the QCD action;

- Identify the correction term using continuum language and order them according to their dimension;

- Choose suitable coefficients for the discretized versions of the correction term so that the corrections up to desired order vanish.

We start from an effective action based on the Wilson fermion action, $S_0 = \int d^4x L_0(x)$ and then add higher order terms to improve its approach to the continuum:

$$S_{\text{eff}} = \int d^4x (L_0(x) + aL_1(x) + a^2 L_2(x) + ...)\,. \tag{2.46}$$

The additional term L_k when $k \leq 1$ are designed to be built from products of quarks and gluon fields to match the dimensions $4 + k$ (L_0 from Eq. 2.37 has dimension 4). This means the additional terms should contain additional derivatives or powers of the quark mass m. Taking into account the proper symmetries of the lattice action, the leading correction term $L_1(x)$ can be written as a combination of 5 dimension-5 operators [34]:

$$
\begin{aligned}
\mathcal{O}_1 &= \overline{\psi}\sigma_{\mu\nu}F_{\mu\nu}\psi \quad \text{where} \quad \sigma_{\mu\nu} = \frac{1}{2i}[\gamma_\mu, \gamma_\nu]\,, \\
\mathcal{O}_2 &= \overline{\psi}\overleftarrow{D}_\mu\overleftarrow{D}_\mu\psi + \overline{\psi}\overrightarrow{D}_\mu\overrightarrow{D}_\mu\psi \quad \text{where} \quad D_\mu = \partial_\mu + igA_\mu\,, \\
\mathcal{O}_3 &= m\,\text{Tr}[F_{\mu\nu}F_{\mu\nu}]\,, \\
\mathcal{O}_4 &= m\overline{\psi}(\overrightarrow{D}_\mu - \overleftarrow{D}_\mu)\gamma_\mu\psi\,, \\
\mathcal{O}_5 &= m^2\overline{\psi}\psi\,.
\end{aligned}
\tag{2.47}
$$

The equation of motion, $(\gamma_\mu D_\mu + m)\psi = 0$, introduces the following constraints:

$$\mathcal{O}_1 - \mathcal{O}_2 + 2\mathcal{O}_5 = 0\,, \quad \mathcal{O}_4 + 2\mathcal{O}_5 = 0\,. \tag{2.48}$$

We can then eliminate two of the operators using these relation and work only with

operators $\mathcal{O}_1$, $\mathcal{O}_3$ and $\mathcal{O}_5$. $\mathcal{O}_3$ and $\mathcal{O}_5$ can be accounted for by a redefinition of the bare parameters m and g. Therefore, we only need to add the Pauli term $\mathcal{O}_1$ to obtain an $\mathcal{O}(a)$ improvement for Wilson fermions. The improved action can be written as

$$S_{\text{clover}} = S_{\text{Wilson}} + c_{sw} a^5 \sum_{n \in \Lambda} \sum_{\mu < \nu} \overline{\psi}(n) \frac{1}{2} \sigma_{\mu\nu} F_{\mu\nu}(n) \psi(n), \tag{2.49}$$

where c_{sw} is Sheikholeslami-Wohlert coefficient [34]. The choice of $F_{\mu\nu}$ is not unique, we can choose a convenient form as

$$F_{\mu\nu}(n) = \frac{-i}{8a^2} \left(Q_{\mu\nu}(n) - Q_{\nu\mu}(n) \right), \tag{2.50}$$

where

$$Q_{\mu\nu}(n) = U_{\mu\nu}(n) + U_{\nu,-\mu}(n) + U_{-\mu,-\nu}(n) + U_{-\nu,\mu}(n). \tag{2.51}$$

The schematic representation of $Q_{\mu\nu}$ is shown in Fig. 2.2. Because the shape of $Q_{\mu\nu}$ resembles a four-leaf clover, this improved action is often referred to as clover improvement action and the additional term is called clover term. The coefficient c_{sw} of the clover term can be computed perturbatively which was shown in [34, 35] as:

$$c_{sw} = 1 + 0.2659 g^2 + \mathcal{O}(g^4). \tag{2.52}$$

The perturbative result is not particular useful in a regime where the coupling g is not small. Non-perturbative methods have been designed for determining c_{sw} [36]. For smeared actions with tadpole improvement [37], c_{sw} is shown to be close to one when using nHYP-smeared links [38]. Therefore, we use $c_{sw} = 1$ in our calculations.

2.3.2 Lüscher-Weisz action

The Wilson gauge action S_g in Eq. 2.39 has a discretization error $\mathcal{O}(a^2)$ (in section 2.2.2 we showed that it is at least $\mathcal{O}(a)$, but symmetries make the action correct to $\mathcal{O}(a^2)$).
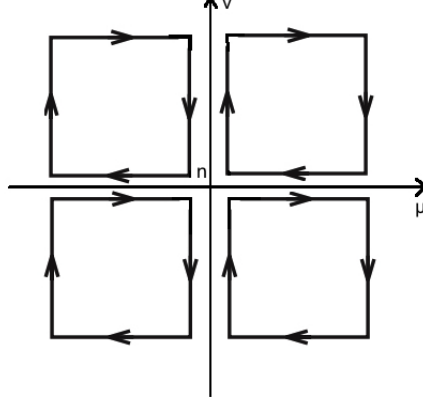
Figure 2.2: Graphical representation of $Q_{\mu\nu}$, the clover term, for $\mathcal{O}(a)$ improved Wilson fermions.

Lüscher and Weiss [39] improved the Wilson gauge action discretization error to $\mathcal{O}(a^4)$ using Symanzik's ideas. This Lüscher-Weisz action is given by

$$S_g^{LW} = \beta_{pl} \sum_{pl} \frac{1}{3} \mathrm{Tr}[1 - U_{pl}] + \beta_{rt} \sum_{rt} \frac{1}{3} \mathrm{Tr}[1 - U_{rt}] + \beta_{pg} \sum_{pg} \frac{1}{3} \mathrm{Tr}[1 - U_{pg}], \quad (2.53)$$

which is depicted in Fig. 2.3. The pl, rt and pg in Eq. 2.53 stands for plaquette, rectangle and parallelogram which correspond to (0), (1) and (3) in Fig. 2.3. The coefficient β_{rt} and β_{pg} can be related to β_{pl} using lattice perturbation theory [40]:

$$\beta_{rt} = -\frac{\beta_{pl}}{20u_0^2}(1 + 0.4805\alpha_s), \quad (2.54)$$

$$\beta_{pg} = \frac{\beta_{pl}}{u_0^2}0.03325\alpha_s, \quad (2.55)$$

$$(2.56)$$

with

$$\alpha_s = -\frac{\ln(\frac{1}{3}\,\mathrm{Re\,Tr}\,\langle U_{pl}\rangle_U)}{3.06839}. \quad (2.57)$$
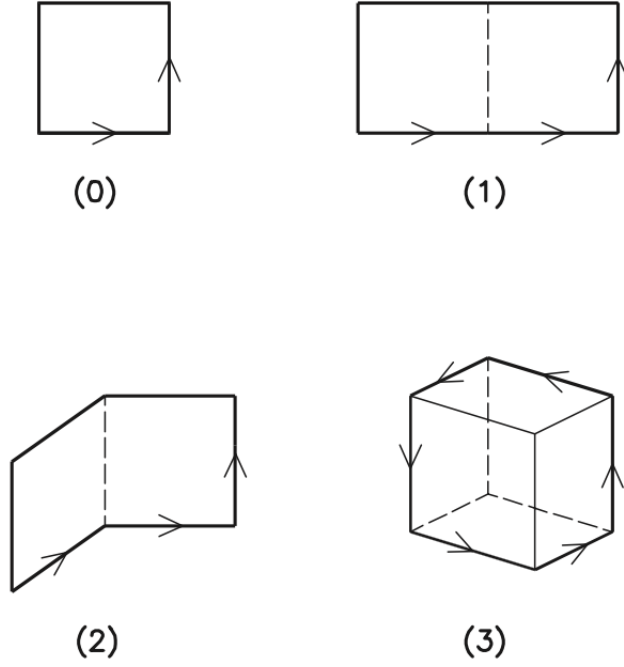
Figure 2.3: The set of 4- and 6-links loops used to construct the $\mathcal{O}(a^4)$ Lüscher-Weiss gauge action.

The coefficient u_0 in equations above is related to tadpole improvement introduced by Lepage and Mackenzie [37]

$$u_0 = \left[\frac{1}{3} \operatorname{Re} \operatorname{Tr} \langle U_{pl} \rangle \right]^{\frac{1}{4}} . \tag{2.58}$$

2.3.3   n-HYP smearing

Smeared gauge configurations suppress the short distance fluctuations, leading to better numerical properties, in particular a better conditioning number for the fermionic matrix which significantly improves in the convergence time for inverters used in lattice QCD calculations. HYP smearing was first introduced by Hasenfratz and Knechtli [41] as a more local variant of repeated APE smearing [42]. The staple sum

$\Gamma_{n,\mu} = \sum_{\nu \neq \mu} U_{\mu,\nu} U_{n+\nu,\mu} U^\dagger_{n+\mu,\nu}$ is added to the original link $U_{n,\mu}$ as

$$\Omega_{n,\mu} = (1-\alpha)U_{n,\mu} + \alpha' \Gamma_{n,\mu}, \tag{2.59}$$

where $\alpha' = \alpha/m$ and m is the number of staples included in the staple sum. Then the smeared link can be obtained by projecting Ω back to $SU(3)$ using

$$V_p = \max_{V \in SU(3)} \operatorname{Re} \operatorname{Tr}(V\Omega^\dagger). \tag{2.60}$$

This link construction is known as projected- or p-APE. With these building blocks, the HYP smearing is constructed using three consecutive projected APE type smearing steps but only links within the hypercubes attached to the original link are included. The schematic representation for the HYP smearing is shown in Fig. 2.3.3. Here, the fat links are the smeared links and thin links are the original links. Three consecutive smearing levels are constructed as:

$$V_{n,\nu} = \operatorname{Proj}_{SU(3)} \left[(1-\alpha_1)U_{n,\mu} + \frac{\alpha_1}{6} \sum_{\pm\nu\neq\mu} \tilde{V}_{n,\nu;\mu} \tilde{V}_{n+\hat{\nu},\mu;\nu} \tilde{V}^\dagger_{n+\hat{\mu},\nu;\mu} \right], \tag{2.61}$$

$$\tilde{V}_{n,\mu;\nu} = \operatorname{Proj}_{SU(3)} \left[(1-\alpha_2)U_{n,\mu} + \frac{\alpha_2}{4} \sum_{\pm\rho\neq\nu,\mu} \overline{V}_{n,\rho;\nu,\mu} \overline{V}_{n+\hat{\rho},\mu;\rho\nu} \overline{V}^\dagger_{n+\hat{\mu},\rho;\nu\mu} \right], \tag{2.62}$$

$$\overline{V}_{n,\mu;\nu\rho} = \operatorname{Proj}_{SU(3)} \left[(1-\alpha_3)U_{n,\mu} + \frac{\alpha_3}{2} \sum_{\pm\eta\neq\rho,\nu,\mu} U_{n,\eta} U_{n+\hat{\eta},\mu} U^\dagger_{n+\hat{\mu},\eta} \right]. \tag{2.63}$$

Here, the $U_{n,\mu}$ represented as the thin links from site n in direction μ, the smeared link $V_{n,\mu}$ are the resulting HYP blocked fat links. $\tilde{V}$ and $\overline{V}$ are the intermediate fields constructed in a way so that the contribution to the smeared link V are restricted to the attached hyper-cube, see Fig. 2.3.3. In Fig. 2.3.3, the fat link is built from the four double-lined staple. Each of the double-lined links is built from the two staples which extend only in the hypercubes attached to the original link. These three consecutive projections to $SU(3)$ ensure that there are only small distorted for the short distance
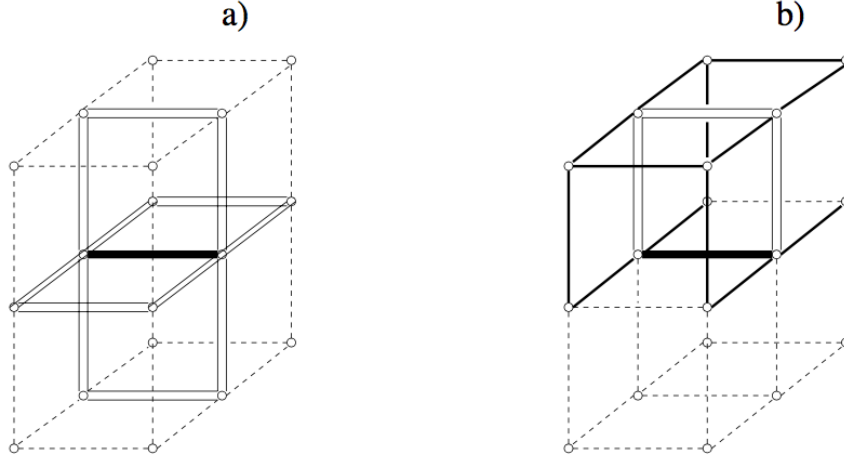
Figure 2.4: Schematic representation of the average procedure in HYP smearing.

properties of the configurations. However, the $SU(3)$ projections makes the HYP links difficult to use in dynamical simulations due to lack of analyticity. An analytic projection is used to define normalized- or n-APE smeared links. Instead of projecting the Ω matrix to $SU(3)$ using Eq. 2.60, the smeared links can be projected using

$$V_n = \Omega(\Omega^\dagger\Omega)^{-1/2}. \tag{2.64}$$

$\Omega^\dagger\Omega$ is Hermitian and positive definite and $(\Omega^\dagger\Omega)^{-1/2}$ is well defined unless $\det\Omega = 0$. The smeared link V_n is unitary but not in $SU(3)$. One can show that the $U(N)$ element V_n link is as effective as the projected smeared link. Finally, the nHYP smeared links is obtained by projecting the Ω matrix back onto $U(3)$ using Eq. 2.64. The projection to U(3) is analytical and makes the nHYP smearing procedure suitable for molecular dynamics gauge generation.

We are now ready to write down the action used in our calculation:

$$S_{\text{QCD}}[U, \psi, \bar\psi] = S_g^{LW}[U] + S_{\text{clover}}[V(U), \psi, \bar\psi], \tag{2.65}$$

where $V(U)$ represents the nHYP-smeared links. Note that the gauge action is expressed in terms of the thin links U, whereas the fermionic part is the clover action described earlier but using the nHYP-smeared links $V(U)$.

2.4 Monte-Carlo sampling for Lattice QCD

In this section we review the techniques used to evaluate numerically observables in lattice QCD. As discussed earlier, the central task is to sample the equivalent statistical mechanics partition sum:

$$Z = \int \mathcal{D}U \det M e^{-S_g[U]} , \qquad (2.66)$$

where $\mathcal{D}U = \prod_{n,\mu} dU_\mu(n)$ and $\det M = \prod_f \det M_f$. To evaluate this integral, we use stochastic methods. We show how to setup a process that samples *gauge configurations* U with the probability density

$$P(U) = \frac{1}{Z} \det M e^{-S_g[U]}. \qquad (2.67)$$

We will discuss first the Markov chains and how observables are estimated, then present the Metropolis methods, a generic method for sampling arbitrary probability distributions, and conclude with a presentation of the hybrid Monte-Carlo, the method of choice for sampling the probability distribution relevant for lattice QCD. The presentation here follows the discussion in Computational Strategies in Lattice QCD by M. Lüscher [43, 44].

2.4.1 Markov chains

To sample gauge configurations we start from an arbitrary configuration and then construct a stochastic sequence of configurations that eventually follows an equilibrium

distribution given by $P(U)$ in Eq. 2.67. This is completed with a *Markov process*

$$U_0 \rightarrow U_1 \rightarrow U_2 \rightarrow ... \rightarrow U_n.... \tag{2.68}$$

The index n labels the order of the configuration it appears in the chain. Each change of a field configuration to a new one is called a Monte Carlo step or an *update*. The update is controlled by a *transition probability* denoted as $T(U'|U)$. In order generate U according to $P(U)$, the transition probability should satisfy the following conditions:

1. $T(U'|U) \geq 0$ for all U, U' and $\sum_{U'} T(U'|U) = 1$ for all U;

2. $\sum_U P(U)T(U'|U) = P(U')$ for all U';

3. $T(U|U) > 0$; (*aperiodicity*)

4. For any non-empty proper subset of states S, there exist two states $U \in S$ and $U' \notin S$ such that $T(U'|U) > 0$ (*ergodicity*).

Under these conditions, $P(U)$ is preserved by the update process. The third and fourth conditions guarantee that the process is aperiodic and every configuration can be eventually reached. The probability for the kth element with starting state U_1 is given by

$$P_k(U) = \sum_{U_2, U_3, ..., U_{k-1}} T(U_2|U_1)T(U_3|U_2)...T(U|U_{k-1}) . \tag{2.69}$$

One can show that for any U_1 we have

$$P_k(U) \underset{k \rightarrow \infty}{\sim} P(U) + \mathcal{O}(e^{-k/\tau}) , \tag{2.70}$$

where τ is called *exponential autocorrelation time*. When k is large, each element is distributed as the equilibrium probability and has no memory of the initial state in the Markov chain. In practice we run the process long enough so that the initial state

memory is lost, we say that the process has *thermalized*, and then collect configurations separated by a number of updates larger that autocorrelation time τ.

After generating an ensembles of configurations $U_1, \ldots, U_N$, an observable $\mathcal{O}$ can be estimated using

$$\langle \mathcal{O} \rangle \approx \frac{1}{N} \sum_{k=1}^{N} \mathcal{O}(U_k) \,. \tag{2.71}$$

The estimator for $\mathcal{O}$ will fluctuate with a standard deviation

$$\sigma_{\mathcal{O}} \propto \frac{1}{\sqrt{N}} \,. \tag{2.72}$$

The standard deviation of the estimator becomes smaller when enlarging the sample size at the cost of extra compute time.

2.4.2 Sampling algorithms

Most algorithms designed for lattice QCD calculations are based on a Markov chain process. To make sure that the process converges to the desired probability density, we have to ensure that the probability density is a fixed point for the transition probability: $\sum_U P(U)T(U'|U) = P(U')$ for all U'. This is automatically satisfied if the transition probability satisfies the *detailed balance* condition

$$T(U'|U)P(U) = T(U|U')P(U') \,. \tag{2.73}$$

The correctness of most sampling algorithms used in lattice QCD—*Metropolis, Heat bath, Overrelaxation, Microcanonical* and *Hybrid Monte Carlo*—is established using detailed balance.

In the following section, we will focus on discussing the Metropolis algorithm which is the most generic (and typically quite inefficient) sampling method. We will then discuss the Hybrid Monte Carlo (HMC) the method of choice for generating dynamical

gauge configurations.

Metropolis algorithm

The Metropolis-Hastings method [45, 46] relies on a transition probability T_0 which is presumably simple to implement and not expected to satisfy the detailed balance with respect to $P(U)$. The method proposed by Metropolis et al. generates a Markov chain with correct probability distribution $P(U)$ using the following procedure:

Step 1: Choose some candidate configuration U' according to transition probability $T_0(U'|U)$, where $U = U_{n-1}$.

Step 2: Accept the candidate configuration U' as the new configuration U_n with the acceptance probability

$$T_A(U'|U) = \min\left(1, \frac{T_0(U|U')\exp(-S[U'])}{T_0(U'|U)\exp(-S[U])}\right), \tag{2.74}$$

otherwise set $U_n = U_{n-1}$.

One can show that the transition probability fulfills the detailed balance condition with respect to $P(U)$. A detailed implementation using this method for pure-glue $SU(3)$ configurations can be found in Ref. [27].

HMC algorithm

The efficiency of the HMC algorithm [47] comes from the fact that it updates all the links at once, it moves large distances in the configuration space, and it scales better with the lattice volume. HMC algorithm samples $P(U) \propto \exp[-S_{\text{QCD}}(U)]$ by generating an ensemble distributed over an extended space. Each link in the configuration $U_\mu(n)$ is parameterized by a set of generalized coordinates $q_\mu^\alpha(n)$ with $\alpha = 1, ..., 8$. We extend the configuration space by pairing each $q_\mu^\alpha(n)$ with a conjugate momentum $p_\mu^\alpha(n)$. $p_\mu(x)$ is interpreted as the canonical momentum of the gauge field.

The probability on this extended space is

$$P_{\text{HMC}}(U,p) \propto \exp(-H(U,p)) \quad \text{where} \quad H(U,p) = \sum_{\mu,n,\alpha} \frac{1}{2}[p_\mu^\alpha(n)]^2 + S_{\text{QCD}}(U). \quad (2.75)$$

One can show for observables that only depend on U, we have

$$\langle O(U) \rangle_P = \langle O(U) \rangle_{P_{\text{HMC}}}. \quad (2.76)$$

HMC algorithm use an interleaved process to generate (U,p) configurations:

Step 1: The new momenta field p are generated according to a Gaussian distribution with probability density proportional to $e^{-p^2/2}$, where $p^2 = \sum_{n,\mu,a} p_\mu^a(n)p_\mu^a(n)$.

Step 2: Integrate the equation of motions generated by $H(U,p)$ to some later time τ to a new position in phase space (U',p').

Step 3: Due to discretization errors the Hamiltonian is not conserved. Compute the Hamiltonian change $\Delta H = H(U',p') - H(U,p)$.

Step 4: Apply a Metropolis accept-reject procedure to the new gauge field U' with probability

$$P_{acc} = \min\{1, e^{-\Delta H}\}. \quad (2.77)$$

One can show that, when the discrete time integrator is time-reversible and symplectic, this procedure satisfies the detailed-balanced condition

$$T(U',p'|U,p)P_{\text{HMC}}(U,p)dUdp = T(U,p|U',p')P_{\text{HMC}}(U',p')dU'dp'. \quad (2.78)$$

This guarantees that the process generates (U,p) samples with the correct distribution, $P_{\text{HMC}}(U,p)$. When disregarding the momenta p, the probability distribution for U is the desired one, $P(U)$. For integrating numerically the equations of motion we use a variant of the leap-frog integrator, the Omelyan integrator. To take into account the fermion determinant, we use pseudo-fermions, and Hasenbush trick to improve the

efficiency. The details of the implementation used in our calculations can be found in Ref. [48].

3 Hadron Spectroscopy

For our project, the basic input from lattice QCD is the mass of the hadrons and the energy of the two-hadron states in a periodic box. In this chapter we will discuss the methods used to extract this information from the two-point correlation functions. We start with an outline of the basic method for extracting the energy spectrum. Then we discuss the symmetries of lattice QCD and how to use them to design interpolators with the right quantum numbers. Finally we cover three technical developments: *variational method* that allows us to extract a set of excited states by fitting simultaneously a set of similar interpolators, *Laplacean Heaviside smearing* which is instrumental to efficiently generate a large set of correlators, and then discuss correlated fitting and jackknife resampling, standard statistical techniques used to compute the energies from correlators and extract reliable error estimates.

3.1 Hadron interpolators and correlators

In the operatorial picture the relation between the two-point functions and the energy eigenstates of the Hamiltonian is easy to see. Consider the correlation function for the operator $\hat{O}$ (or its corresponding interpolator O); if we insert a complete set of states we have

$$C(t) = \left\langle O(t)O^\dagger(0)\right\rangle = \langle \Omega \,|\hat{O}e^{-tH}\hat{O}^\dagger|\,\Omega\rangle = \sum_n |\langle n\,|\hat{O}^\dagger|\,\Omega\rangle|^2\, e^{-E_n t}\,, \qquad (3.1)$$

where n labels the eigenstates of the Hamiltonian and E_n the corresponding eigenvalues. For large times the correlator is dominated by the slowest decaying term

$$C(t) \propto |\langle 0\,|\hat{O}^\dagger|\,\Omega\rangle|^2\, e^{-E_0 t}[1 + \mathcal{O}(e^{-\Delta E t})]\,, \qquad (3.2)$$

where we assume that $n = 0$ correspond to the state that has the lowest energy among those that have a non-zero *overlap* coefficient, that is $\langle n\,|\hat{O}^\dagger|\,\Omega\rangle \neq 0$. The

correction is driven by the gap to the next state with non-zero overlap, say E_1, so that $\Delta E = E_1 - E_0$. Thus, to be able to extract reliably the energy of state $|0\rangle$, E_0, we need to compute the correlator accurately for large time, that is $t \gg 1/\Delta E$.

The interpolators are built from quark and gluon fields with the quantum numbers of the state one is interested in. They are built by constructing gauge-invariant color singlets. The candidate for interpolators include:

- Local meson operators such as $O(n) = \overline{\psi}(n)\Gamma\psi(n)$, consisting of quarks and antiquarks or baryons operators made out of threes quarks;

- Extended interpolators such as $\overline{\psi}(n)U_\mu(n)\psi(n+\hat{\mu})$;

- Pure gauge field interpolators, like the plaquette, for gluonic obejects such as glueballs;

- More exotic color-singlet combinations of quarks and antiquarks like $\overline{\psi}\overline{\psi}\psi\psi$.

In this study, our interest is studying resonance in meson-meson scattering, therefore, we focus on discussing meson interpolators on the lattice.

3.2 Symmetries on the lattice

In order to obtain the energy spectrum of interest from lattice QCD, one needs to construct the corresponding interpolating field with correct quantum numbers and symmetries. In this section, we will show that by a careful choice of interpolating fields it is possible to restrict the energy spectrum from a particular symmetry sector. In the following, we refer to a transformation as a symmetry when it leaves the lattice Hamiltonian invariant. For convenience, it is possible to classify two types of symmetries in QCD theory, *spatial symmetries* and *internal symmetries*. Spatial symmetries contain translational and rotational symmetries which bring the lattice back into coincidence with itself; internal symmetries leave the space-time coordinates unchanged and they are independent of translations and rotations.

3.2.1 General considerations

All symmetries form a group, which we will denote with G in the following. These transformations commute with the Hamiltonian and, as a consequence, any subspace generated by applying symmetry transformations to an eigenstate of the Hamiltonian form a degenerate subspace. These subspaces are invariant subspaces of the symmetry group and, bearing any accidental degeneracies, a basis in this subspace furnishes a basis for an irreducible representation (or *irrep*) of the group.

Assume $T(g)$ is the unitary operator on the Hilbert space of states that correspond to symmetry transformation $g \in G$. We say of a vector $|\mu, i\rangle$ belonging to a multiplet $|\mu, j\rangle$ with $j = 1, \ldots, n$ that it changes under the ith row of the n-dimensional μ irrep if

$$T(g) |\mu, i\rangle = \sum_{\mu,j} |j\rangle D_{ji}^{\mu}(g), \quad \text{for all } g \in G. \tag{3.3}$$

The unitary matrices D^{μ} corresponding to the irreducible representation satisfy the orthogonality relations [49]:

$$\sum_{g \in G} D_{ij}^{\mu} (D_{i',j'}^{\mu'})^* = \frac{|G|}{n} \delta^{\mu,\mu'} \delta_{i,i'} \delta_{j,j'} . \tag{3.4}$$

Using the orthogonality relations, we can then show that

$$\langle \mu, i \, | \mu', i' \rangle = \delta^{\mu,\mu'} \delta_{i,i'} . \tag{3.5}$$

In quantum mechanics μ and i usually labels the quantum numbers of the state (for example for rotations we have J and J_z).

Similarly, for an operator $\hat{O}_i$ belonging to a set of operators O_j, with $j = 1, \ldots, n$, we say that it transforms under the ith row of irrep μ if

$$T(g)\hat{O}_i^{\dagger}T(g)^{\dagger} = \sum_j O_j^{\dagger} D_{ji}^{\mu}, \quad \text{for all } g \in G. \tag{3.6}$$

We assume that the vacuum state is invariant under the symmetries, that is $T(g)\,|\Omega\rangle = |\Omega\rangle$. In this case the kets $\hat{O}_j^\dagger\,|\Omega\rangle$ for $j = 1,\ldots,n$, forms a n-dimensional multiplet, that is a basis for the μ irrep. As such, using the orthogonality properties above, the overlap $\langle n\,|\hat{O}_i^\dagger|\,\Omega\rangle$ is non-zero only if n belongs to a multiplet that has the same quantum numbers, that is $|n\rangle = |\mu, i\rangle$.

Thus, if we are interested in generating states with quantum numbers μ, i, we have to prepare an operator $\hat{O}_i^\dagger$ that transform appropriately. The task is then to design such a set of such operators. Recalling that the operators are built as combinations of the elementary fields, which have well defined transformation properties under the symmetry operations, such multiplets can be built using the appropriate rules for splitting tensor product representations into the direct sum of irreps (using tabulated values for Clesch-Gordan coefficients, etc). Another possibility, is to start with an operator that has some of the desired properties, and use the following *projectors* [49]

$$P_i^\mu \hat{O}^\dagger \equiv \frac{n_\mu}{|G|}\sum_{g\in G} D_{ii}^*(g)T(g)O^\dagger T(g)^\dagger\,, \quad P_i^\mu\,|n\rangle \equiv \frac{n_\mu}{|G|}\sum_{g\in G} D_{ii}^*(g)T(g)\,|n\rangle\,. \qquad (3.7)$$

If the operator $\hat{O}$ or state $|n\rangle$ overlap with the ith row of irrep μ, the projectors will generate a good candidate, otherwise the projector vanishes and we need to find a better operator (or ket).

3.2.2 Isospin symmetry

From a historical point of view, the iso-spin concept was introduced by Werner Heisenberg to explain the apparent symmetry between the masses and nuclear interactions of the proton and neutron. Today we know that the origin of the symmetry is related to the flavor symmetry between up and down quarks. If their masses were exactly equal and the effect of electromagnetic interaction was neglected, the symmetry would be exact. However, their mass splitting is small compared to the QCD scale and the

deviations from the exactly symmetric case are at percent level. In our calculations, we use mass degenerate flavors, so the symmetry will be exact.

In QCD, the u and d quarks form an isospin doublet. An up-quark u has isospin $I = \frac{1}{2}, I_z = +\frac{1}{2}$ and charge $Q = \frac{2}{3}e$. The down quark has $I = -\frac{1}{2}, I_z = -\frac{1}{2}$ and $Q = -\frac{1}{3}e$. We can arrange the two quark flavors in a two-component object

$$\psi = \begin{pmatrix} u \\ d \end{pmatrix}, \tag{3.8}$$

which transforms under isospin rotations as

$$\psi \to D\psi, \quad \overline{\psi} \to \overline{\psi}D^\dagger, \quad \text{where } D \in SU(2). \tag{3.9}$$

Isospin is a good symmetry so its irreps labels are good quantum numbers for states in our theory.

Since we are interested in the resonance in the pion-pion scattering channel in this study, we will first focus on the pions. The interpolators used to create mesons have the general structure

$$O_M = \overline{\psi}^{(f_1)} \Gamma \psi^{(f_2)}, \tag{3.10}$$

where f_1 and f_2 are the flavor indices. We have then to combine an isospin-1/2 dublet with the antiquark counter-part. As it turns out, the antiquark doublet $\overline{\psi}$ changes under an irrep that is equivalent with the fundamental irrep. This is a special property of $SU(2)$, for higher dimensional $SU(n)$ groups the fundamental irrep and its complex conjugate are not equivalent. To see this, consider that a generic $SU(2)$ matrix is $D = \exp(i\boldsymbol{\alpha}\boldsymbol{\sigma}) = \cos\alpha + i\hat{\boldsymbol{\alpha}}\boldsymbol{\sigma}\sin\alpha$. Then we can show that $D^* = A^{-1}DA$ with $A = i\sigma_2$, so that $A\overline{\psi}^T$ changes under the fundamental irrep. The doublet of

anti-quarks that changes under the fundamental irrep is

$$A\bar{\psi}^T = i\sigma_2\bar{\psi}^T = \begin{pmatrix} \bar{d} \\ -\bar{u} \end{pmatrix}.$$

(3.11)

We can then use the usual Clebsch-Gordan coefficients to combine two isospin-1/2 doublets. Combining $u, d, \bar{u}, \bar{d}$ quarks we get an isotriplet $(I = 1)$ containing π^+, π^-, π^0 and isosinglet $(I = 0)$ containing the η meson. The π^+ and π^- have zero spin $(J = 0)$, negative parity $(P = -1)$, isospin $I = 1, I_z = \pm 1$, and electric charge $Q = \pm e$. The flavor content for these mesons is listed in Tab. 3.1.

Table 3.1: Meson operator fields

particle	flavor content	I	I_z
π^+	$u\bar{d}$	1	1
π^0	$\frac{1}{\sqrt{2}}(u\bar{u} - d\bar{d})$	1	0
π^-	$-d\bar{u}$	1	-1
η	$\frac{1}{\sqrt{2}}(u\bar{u} + d\bar{d})$	0	0

Parity and charge-parity (or G-parity) of the interpolators in Eq. 3.10 also needs to be considered. For these local interpolators, the parity and total angular momentum J are controlled by the Γ matrix. The quantum numbers generated by different Γ choices is listed in Table 3.2. For charged pions we have

$$\mathcal{O}_{\pi^+}(n) = \bar{d}(n)\gamma_5 u(n) = \bar{d}(n)_{\alpha c}(\gamma_5)_{\alpha\beta} u(n)_{\beta c},$$
$$\mathcal{O}_{\pi^-}(n) = \bar{u}(n)\gamma_5 d(n) = \bar{u}(n)_{\alpha c}(\gamma_5)_{\alpha\beta} d(n)_{\beta c}.$$

(3.12)

Above, n is a position index, α and β are spinorial indices, and c is the color index. Similarly, the interpolator for the $I_z = 0$ component of the isotriplet π^0 is given by

$$\mathcal{O}_{\pi^0}(n) = \frac{1}{\sqrt{2}}[\bar{u}(n)\gamma_5 u(n) - \bar{d}(n)\gamma_5 d(n)].$$

(3.13)

Table 3.2: Quantum number of commonly used meson interpolators

State	J^{PC}	Γ	Particles
Scalar	0^{++}	$\mathbf{1}, \gamma_4$	$f_0, a_0, K_0^*, ...$
Psudoscalar	0^{-+}	$\gamma_5, \gamma_4 \gamma_5$	$\pi^\pm, \pi^0, \eta, K^\pm, K^0, ...$
Vector	1^{--}	$\gamma_i, \gamma_4 \gamma_i$	$\rho^\pm, \rho^0, \omega, K^*, \phi, ...$
Axial vector	1^{++}	$\gamma_i \gamma_5$	$a_1, f_1, ...$
Tensor	1^{+-}	$\gamma_i \gamma_j$	$h_1, b_1, ...$

For the ρ meson, a vector meson with $I = 1$ and $J = 1$, we have

$$\mathcal{O}_{\rho^+}(n)_i = \bar{d}(n)\gamma_i u(n) \,, \mathcal{O}_{\rho^-}(n)_i = \bar{u}\gamma_i u(n), i = 1, 2, 3\,, \tag{3.14}$$

and

$$\mathcal{O}_{\rho^0}(n) = \frac{1}{\sqrt{2}}[\bar{u}\gamma_i u(n) - \bar{d}(n)\gamma_i d(n)] \quad i = 1, 2, 3\,. \tag{3.15}$$

The σ meson has $I = 0$, $J = 0$, $P = 1$ and, according to Tab. 3.2, the local σ meson interpolator can be constructed as

$$\mathcal{O}_\sigma(n) = \frac{1}{\sqrt{2}}\left[\bar{u}(n)u(n) + \bar{d}(n)d(n)\right]\,. \tag{3.16}$$

For completeness, as an example, we derive the correlation function for one of the pion interpolator in Eq. 3.12:

$$
\begin{aligned}
C_{\pi \leftarrow \pi} &= \left\langle \mathcal{O}_{\pi^+}(n)\mathcal{O}_{\pi^+}^\dagger(m) \right\rangle_F = \left\langle \bar{d}(n)\gamma_5 u(n)\bar{u}(m)\gamma_5 d(m) \right\rangle_F \\
&= -(\gamma_5)_{\alpha_1\beta_1}(\gamma_5)_{\alpha_2\beta_2} \left\langle u(n)_{\beta_1 c_1}\bar{u}(m)_{\alpha_2 c_2} \right\rangle_u \left\langle d(m)_{\beta_2 c_2}\bar{d}(n)_{\alpha_1 c_1} \right\rangle_d \\
&= -(\gamma_5)_{\alpha_1\beta_1}(\gamma_5)_{\alpha_2\beta_2} M_u^{-1}(n|m)_{\beta_1 c_1; \alpha_2 c_2} M_d^{-1}(m|n)_{\beta_2 c_2; \alpha_1 c_1} \\
&= -\text{Tr}[\gamma_5 M_u^{-1}(n|m)\gamma_5 M_d^{-1}(m|n)]\,.
\end{aligned}
\tag{3.17}
$$

Above we used Wick's theorem (see for example Ref. [27]) and expressed the correlator

as a function of the quark propagator:

$$\left\langle \psi_{\alpha a}^{f}(y)\overline{\psi}_{\beta b}^{f}(x) \right\rangle_{F} = (M^{f})^{-1}[U](y,x)_{\alpha a,\beta b}\,. \tag{3.18}$$

Above we made explicit the dependence of the quark-propagator on the gauge field U, and the relevant spinoral (α, β) and color indices (a, b).

3.2.3 Rotational symmetry

The full rotational symmetry group in 3 dimensions is $SO(3)$, the group of orthogonal matrices with determinant 1, and $O(3)$ if we include reflections. The irreps of $SO(3)$ are labeled by the integer angular momentum J which have dimension $2J+1$. Here we consider only the integral-spin particles, so we do not have to consider half-integral irreps. On the lattice, the symmetry is broken to the cubic subgroup by the discretization. Further breaking is possible when taking into account the geometry of the box used in our calculations. When using periodic boundary conditions, any rotation allowed must preserve the periodicity:

$$R\psi(\mathbf{x}) = \psi(R^{-1}\mathbf{x}) = \psi(R^{-1}(\mathbf{x}+\mathbf{L})) \quad R \in SO(3)\,, \tag{3.19}$$

For cubic boxes, $L_x = L_y = L_z$, the symmetry group is the cubic group O (also called the octahedral group). The other case we will consider, is when one of the sides of the box is elongated $L_x = L_y = L$ and $L_z = \eta L$ with $\eta \geq 1$. In this case the symmetry group is reduced to the dihedral group D_4. If we consider reflections (or inversions) the relevant symmetry groups are O_h and D_{4h}, respectively. Both O_h and D_{4h} are products of the original group with the two-element group $\{E,P\}$, where E is the identity and P the spatial inversion, and the irreps of the enlarged groups are generated by extending the original group irreps with the parity of the representation.

In this study, we used for our calculation both the cubic and elongated boxes. The

reason of this will be discussed in section 4.2. In the following discussion, we focus on listing the representations for cubic and elongated box, and the relation of the irreps of these two symmetry groups to the $2J + 1$ irreps of $SO(3)$.

First, let us consider the *octahedral* symmetry group O; the group contains 24 rotations in 5 conjugacy classes:

E: Identity.

C_4: rotations around the three 4-fold axes through an angle of $\pm\pi/2$.

C_4^2: rotations around the three 4-fold axes through an angle of π.

C_2: rotations around the six 2-fold axes (face diagonals) by π.

C_3: rotations around the four 3-fold axes (body diagonals) by $\pm\frac{2\pi}{3}$.

The n-fold we used above means that the object rotating around a given axes n times will be coincident with its original status. Above C_n^l denotes the rotation through $2\pi/n$ and l means the l times successive applications of the C_n transformation. In contrast to the $SO(3)$ group which has an infinite number of irreps denoted by the angular momentum J, the O group only has 5 irreps. The characters (trace) of the matrices representing the transformations, differ for each irrep. For example, the dimension of an irrep is the character of the identity E. The orthogonality property in Eq. 3.4 leads to an orthogonality property for the irrep characters [49]:

$$\sum_{g \in G} \chi^\mu(g)^* \chi^{\mu'}(g) = \delta^{\mu\mu'} |G|. \tag{3.20}$$

The characters for each conjugacy class for the O group are listed in Table 3.3.

Each multiplet of $SO(3)$ forms a basis for a reducible representation of the O group. The decomposition of this representation into the irreps for O can be determined using the orthogonality relation above. Considering the basis provided by the Y_{lm} functions,

Table 3.3: Character table for the irreducible representations of cubic-holohedral symmetry group. The number of elements in each class is included in parenthesis.

Irrep	E	$C_2(6)$	$C_4^2(3)$	$C_4(6)$	$C_3(8)$
A_1	1	1	1	1	1
A_2	1	-1	1	-1	1
E	2	0	2	0	-1
F_1	3	-1	-1	1	0
F_2	3	1	-1	-1	0

we find that characters for the J angular momentum irrep, for a rotation with angle ϕ is

$$\chi^J(\phi) = \sum_{m=-J}^{J} e^{-im\phi} = \frac{\sin(J+1/2)\phi}{\sin\phi/2} \,. \tag{3.21}$$

The resolution for a representation with class characters χ_k ($k = 1, \ldots, 5$), can be computed using $n_\mu = \sum_k n_k (\chi_k^\mu)^* \chi_k / |G|$, where n_k is the number of elements in class k. For example, for $J = 2$ the characters for the 5 conjugacy classes are $5, 1, 1, -1, -1$ and we have

$$A_1: \quad 1 \times 1 \times 5 + 6 \times 1 \times 1 + 3 \times 1 \times 1 + 6 \times 1 \times (-1) + 8 \times 1 \times (-1) = 0 \,,$$

$$A_2: \quad 1 \times 1 \times 5 + 6 \times (-1) \times 1 + 3 \times 1 \times 1 + 6 \times (-1) \times (-1) + 8 \times 1 \times (-1) = 0 \,,$$

$$E: \quad 1 \times 2 \times 5 + 6 \times 0 \times 1 + 3 \times 2 \times 1 + 6 \times 0 \times (-1) + 8 \times (-1) \times (-1) = 24 \times 1 \,,$$

$$F_1: \quad 1 \times 3 \times 5 + 6 \times (-1) \times 1 + 3 \times (-1) \times 1 + 6 \times 1 \times (-1) + 8 \times 0 \times (-1) = 0 \,,$$

$$F_2: \quad 1 \times 3 \times 5 + 6 \times 1 \times 1 + 3 \times (-1) \times 1 + 6 \times (-1) \times (-1) + 8 \times 0 \times (-1) = 24 \times 1 \,,$$

$$\tag{3.22}$$

so that the $J = 2$ quintet splits into a E doublet and F_2 triplet. The resolution of the $SO(3)$ multiplets up to $J = 5$ is included in Table 3.4.

For elongated boxes the relevant group is the *dihedral group* D_4. The symmetry group has five irreducible representations, and eight transformations in five classes:

E: Identity.

Table 3.4: The decomposition of spherical harmonics into 5 irreducible representations of the cubic-holohedral group.

	O group elements characters					Resolution into the $2J + 1$
J	E	C_2	C_4^2	C_4	C_3	
0	1	1	1	1	1	A_1
1	3	-1	-1	1	0	F_1
2	5	1	1	-1	-1	$E \oplus F_2$
3	7	-1	-1	-1	1	$A_2 \oplus F_1 \oplus F_2$
4	9	1	1	1	0	$A_1 \oplus E \oplus F_1 \oplus F_2$
5	11	-1	-1	1	-1	$E \oplus 2F_1 \oplus F_2$

Table 3.5: Angular momentum mix among 5 irreducible representations of octahedral and tetragonal group

Octrahedral group		Dihedral group	
irrep	J	irrep	J
A_1	$0, 4, 6, ...$	A_1	$0, 2, 4, ...$
A_2	$3, 6, ...$	A_2	$1, 3, 4, ...$
F_1	$1, 3, 4, 5, 6$	B_1	$2, 3, 4, ...$
F_2	$2, 3, 4, 5, 6, ...$	B_2	$2, 3, 4, ...$
E	$2, 4, 5, 6, ...$	E	$1, 2, 3, 4, ...$

C_4: rotation around z-axis through an angle $\pm\frac{\pi}{2}$.

C_4^2: two successive C_4 around z-axis.

C_2: rotation around the two 2-fold axis perpendicular to the z-axis.

$C_{2'}$: rotation around the two 2-fold axis at the bisectors of the angles between the above axes through an angle π.

For this group a similar decomposition of the $SO(3)$ multiplets as for the cubic group can be worked out. We will now focus on the reverse process, which is to find the correspondence between the lattice group irrep and the infinite volume one. In Table 3.5 we show the $SO(3)$ multiplets, up to $J = 6$, that overlap with the lattice irrep for both cases. For the ρ case we will construct operators that transform under A_2^- irrep on elongated boxes, which overlap with $J = 1$, the relevant angular

momentum for ρ-resonance. Note that these operators also overlap with $J = 3, 5, \ldots$, so we have to assume that the higher partial waves can be safely neglected for the energies relevant to our study.

3.3 Laplacean Heavside smearing

Laplacian Heaviside (LapH) smearing [50, 51] addresses two challenges that appear in lattice QCD calculations for spectral quantities. Firstly, as we mention in section 3.2.2, the $\bar{q}q$ interpolators are local operators which have significant overlap with many high energy states making the extraction of the lowest states in the spectrum difficult. A possible solution to this problem is to construct *smeared* operators, that is operators that have a smoother spatial profile. The purpose of building a smeared quark field is to reduce the component of the fields close to the cutoff because those high frequency modes do not have significant contribution to the low-lying energy states.

The second reason is that when we calculate the two-point correlation functions for interpolators that create two-meson states, the correlation functions require quark propagators that propagate between four different space-time points. While the correlation functions generated by $\bar{q}q$ to $\bar{q}q$ interpolators can be evaluated cheaply by computing the quark propagator from one point on the lattice and using translational invariance, this is not possible for the meson-meson to meson-meson correlation functions. In this case, the all-to-all propagators is required, but this is numerically impractical. One possibility is to use stochastic estimators for these correlation functions or, as we do in this project, the projection of the all-to-all propagator to the low-momentum space spanned by the LapH vectors.

The smearing is constructed using the eigenvectors of the three-dimensional covariant Laplace operator,

$$\Delta_t = -\sum_{k=1}^{3} \nabla_k(t)\nabla_k(t)^\dagger \,, \tag{3.23}$$

46

with the components

$$\Delta_t^{ab}(\boldsymbol{x}, \boldsymbol{y}) = \sum_{k=1}^{3} [U_k^{ab}(\boldsymbol{x}, t)\delta(\boldsymbol{x} + \hat{k}, \boldsymbol{y})$$
$$+ U_k^{ba}(\boldsymbol{y}, t)^*\delta(\boldsymbol{x} - \hat{k}, \boldsymbol{y}) - 2\delta^{ab}\delta(\boldsymbol{x}, \boldsymbol{y})]. \tag{3.24}$$

This operator is negative-definite and its eigenvalues are all negative. We sort the eigenvalues so that $\lambda_1(t) > \lambda_2(t) > \dots$. Using the eigenvectors $|s; t\rangle$ of Δ_t corresponding to eigenvalue $\lambda_s(t)$, we define the smearing operator:

$$\mathcal{S}(t) \equiv \sum_{s=1}^{N_v} |s; t\rangle \langle s; t|, \tag{3.25}$$

which is the projector on the space spanned by the N_v lowest frequency eigenmodes of the Laplacean operator. The smearing operator only acts on the spatial and color space. The smeared quark field is

$$\tilde{q}(t) \equiv \mathcal{S}(t)q(t). \tag{3.26}$$

The bilinears $\tilde{\bar{q}}\Gamma\tilde{q}$ have the same transformation properties as $\bar{q}\Gamma q$ and we can use them as building blocks for the ρ and $\pi\pi$ interpolators defined in the previous section. The advantage of this substitution is that, on one hand, the correlation functions will be less noisy, since the overlap of these interpolators with the physical states is better when we choose N_v appropriately. On the other hand, as we will show below, the calculation of all the correlation functions requires only the evaluation of the quark propagators from $4 \times N_v \times N_t$ sources, which is a significant improvement over evaluating the all-to-all propagator when $4N_v \ll N$.

After Wick contractions, the correlation functions are identical in form with the original correlation functions in Eq. 3.17, with the quark propagator replaced with a

smeared version

$$\langle q(t)\bar{q}(t')\rangle \rightarrow \langle \tilde{q}(t)\tilde{\bar{q}}(t')\rangle = \mathcal{S}(t)M^{-1}(t,t')\mathcal{S}(t')\,. \tag{3.27}$$

We define $\tilde{M}$ matrices as

$$\tilde{M}^{-1}(t,t')^{\alpha\beta}_{s,s'} \equiv \left\langle s;t \left| M^{-1}(t,t')^{\alpha\beta} \right| s';t' \right\rangle, \tag{3.28}$$

which are $(4N_v) \times (4N_v)$ matrices. Above, s, s' are eigenvector indices and α, β are spinorial indices. These relations can be easily derived using the definition of the smearing operator and the cyclic property of the trace. We note then that the we only require the evaluation of the smeared all-to-all propagator $\tilde{M}^{-1}$ which only requires $4N_v \times N_t$ inversions compared to $N \times N_t$ for the all-to-all propagator, where $N = 12 \times N_x \times N_y \times N_z$. For example, even on the smallest lattice used in this study $N = 12 \times 24^3 = 165,888$ whereas $4N_v = 400$, a significant reduction.

We also note that the traces are over square-matrix products with dimension $4N_v$. When evaluating a large number of diagrams, the bottleneck becomes the matrix-matrix products. It is then advisable to carefully examine the required products to reduce the calculation. One such simplification can be implemented for matrices in this $4N_v$ space that factorize in a tensor product between the spinorial and Laplacean subspaces. For example

$$\tilde{\Gamma}(\boldsymbol{p};t) = \gamma_3 \tilde{e}^{i\boldsymbol{p}}(t)\,, \tilde{e}^{i\boldsymbol{p}}(t)_{s,s'} \equiv \left\langle s;t \left| e^{i\boldsymbol{p}} \right| s';t \right\rangle\,. \tag{3.29}$$

The multiplication with this matrix can be implemented four times more efficient than when using a full $(4N_v) \times (4N_v)$ representation for the $\tilde{\Gamma}$ matrix.

The action of the smearing operator $\mathcal{S}$ can be illustrated by acting on a point source. The magnitude of $\|(\mathcal{S}\delta_{\boldsymbol{x}})(\boldsymbol{y})\|$ decays like a gaussian away from the source,
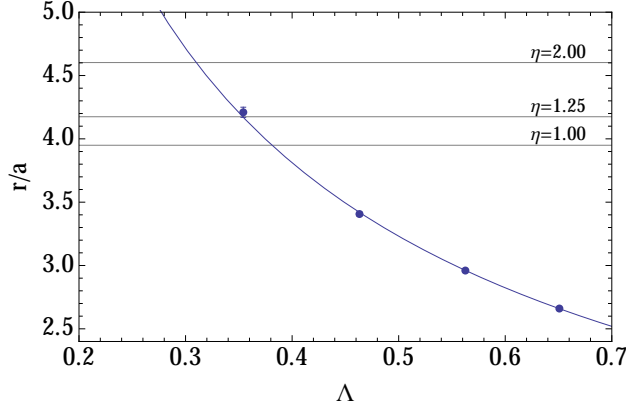
Figure 3.1: Smearing radius for pion mass $m_\pi = 315\,\mathrm{MeV}$ and lattice spacing $a \approx 0.121\,\mathrm{fm}$.

$\exp(-\|\boldsymbol{x} - \boldsymbol{y}\|^2 / r^2)$. The smearing radius r depends of the on the energy cutoff, $\Lambda = -\lambda_{N_v}(t)$. We can determine the optimal Λ by tuning individual operators to minimize the errorbars of the effective mass at a fixed time [50]. In this study, we fix the number of Laplacean eigenvectors to $N_v = 100$. Since the volume varies with the ensemble, the energy cutoff and the smearing radius change with the ensemble too. In Fig. 3.1 we plot the smearing radius as a function of Λ for the higher mass ensembles. The radius is evaluated on a $16^3 \times 32$ ensembles for $N_v = 25$, 50, 75, and 100 and the line represents a power law fit. The horizontal lines indicate the smearing radius corresponding to $N_v = 100$ on ensembles $\mathcal{E}_1$, $\mathcal{E}_2$, and $\mathcal{E}_3$ (see Tab. 5.1). We indicate in the figure the smearing radius for $\eta = 1$, 1.25, and 2. Note that the change in the smearing radius from the smallest to the largest volume is about 10%, so the smearing is very similar on all ensembles, with $r \approx 0.5\,\mathrm{fm}$ which is comparable to the radius of the ρ meson.

Besides the fact that the LapH smearing filters the high frequency mode contribution to the low-lying energy states, it has several benefits in the numerical calculation. One benefit of this method is that we can separate the calculation of the smeared quark propagator $\tilde{M}^{-1}$ from computing the correlation functions. This is very important when using a large set of interpolators (see the discussion of the variational method

in the next section), especially since it allows to add other interpolating fields to the basis without having to redo the inversions. Another point that we want to stress is that the smearing employed here does not represent an approximation. The smeared interpolating fields have the right symmetry properties even when the number of Laplacean eigenvectors N_v is very small. If the number is too small the overlap with the physical states is poor and the signal-to-noise ratio will be bad. Finally, even though the number of inversions is much smaller than the total number required for the all-to-all propagator, we still need to compute $4N_v \times N_t$ inversions for each configuration: 19,200 and 25,600 inversions per configuration for the $m_\pi = 315\,\text{MeV}$ and $m_\pi = 226\,\text{MeV}$ ensembles, respectively (the difference is due to the fact that we use $N_t = 48$ on the larger mass ensembles, and $N_t = 64$ for the lower mass ones).

To show the improvement due to the LapH smearing, we compare the correlators of the smeared and unsmeared interpolators. To better observe this difference, in Fig. 3.2 we plot the *effective mass*, that is the logarithmic derivative of the correlator

$$m_{\text{eff}}\left(n_t + \frac{1}{2}\right) = \log \frac{C(n_t)}{C(n_t + 1)},$$
(3.30)

which is expected to plateau when the correlator is dominated by a single exponential. The value of the effective mass at the plateau corresponds to the energy of the ground state. We can see that the effective mass approaches the ground state energy faster with LapH smearing which helps us extract the energy with increased precision. This is because we can fit the correlator from an earlier time where the signal-to-noise ratio is better.

3.4   Variational method

As we discussed in section 3.1 two-point correlators are a sum of multiple exponentials with their spectral coefficient, each exponentials has its own decay rate. We can extract
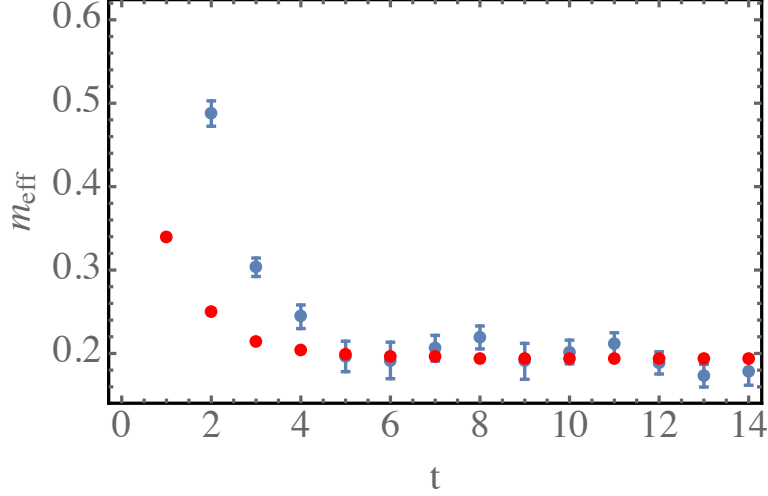
Figure 3.2: Comparison of pion effective mass on $16^3 \times 32$ $m_\pi \approx 300\,\mathrm{MeV}$ ensemble. Red: with LapH smearing; Blue: without LapH smearing.

the ground state energy by fitting the correlator at large times when the contributions from the higher energy levels is suppressed. However, it is often desirable to extract excited states energies, in order to access the kinematic region where the resonance are located. In principle, a direct multi-exponential fit of the correlation function would work if the number of data points was large and precise enough. However, data from Monte Carlo simulations have stochastic fluctuation and in practice a direct fit leads to results with large stochastic errors.

One possible solutions to this problem is to fit several correlators, generated by interpolators with the same quantum numbers, simultaneously. This is accomplished using the *variational method* proposed by Lüscher and Wolff [52]. The idea is to construct a correlation matrix using a set of interpolating fields with the same quantum numbers and extract the energy levels by solving an eigenvalue problem. Choosing a set of interpolating fields with different couplings to the eigenstates of the Hamiltonian helps to resolve energy states that are nearly degenerated. In our case the interpolating field set will include both quark-antiquark (single-hadron) and multi-hadron interpolating fields.

The correlation matrix is constructed from two-point functions of all the interpo-

lating fields in the basis. If we denote the N interpolators in the basis with $\mathcal{O}_i$ with $i = 1, \ldots, N$, the elements of the correlation matrix are

$$C_{ij}(t) = \left\langle \mathcal{O}_i(t) \mathcal{O}_j^\dagger(0) \right\rangle . \tag{3.31}$$

We compute the eigenvalues of the correlation matrix by solving the generalized eigenvalue problem

$$C(t)\psi^{(n)}(t, t_0) = \lambda^{(n)}(t, t_0) C(t_0)\psi^{(n)}(t, t_0) , \tag{3.32}$$

or equivalently

$$C(t_0)^{-\frac{1}{2}} C(t) C(t_0)^{-\frac{1}{2}} \psi^{(n)}(t, t_0) = \lambda^{(n)}(t, t_0)\psi^{(n)}(t, t_0) , \tag{3.33}$$

for a particular initial time t_0 and for each time slice t. For $t \in [t_0, 2t_0]$ the eigenvalues were shown to behave as [52, 53]

$$\lambda^{(n)}(t, t_0) \propto e^{-E_n t}[1 + \mathcal{O}(e^{-\Delta E_n t})], \quad n = 1, \ldots, N , \tag{3.34}$$

where the correction is driven by the energy difference $\Delta E_n = E_{N+1} - E_n$. This long-time behavior shows that the larger interpolating basis we use, the faster the correction for the low energy states vanishes. The interpolators in the basis should be independent and have good overlap with the eigenstate of the problem. However, since the energy eigenstates get denser in the higher-energy part of the spectrum, the payoff of the variational method decreases as the size of the correlation matrix increases. In realistic calculations, including more interpolators enhances the statistical noise and thus affects the diagonalization. It is better to choose the operators which are close to the expected physical content of the eigenstates.

3.5 Data analysis

Resonance parameters extracted from lattice QCD are functions of the energies extracted from correlators. The energies are, in turn, extracted from fits of exponential functions of the correlators computed using stochastic methods. To estimate the errors for the parameters extracted from the fits, including the correlation between the fluctuations of these parameters, we rely on the theory behind the *correlated fits* that take into account the cross-correlation between the values of the correlators at different times. Moreover, in a realistic calculation, the extraction of the energy levels is only the first step in the procedure. The physical quantities of interest which will be discussed in chapter 4 are usually complex functions of the measured correlation functions. Therefore, it is non-trivial to estimate the errors through a direct error propagation approach. In our analysis, we used the data resampling method to evaluate the parameters errors and correlations. In particular, we used the *jackknife* method to solve this problem. In this section we discuss the extraction of energy levels from correlated fits and error propagation using the jackknife resampling method.

Correlated χ^2-fits

As discussed in earlier sections, the first step in our calculations is to compute the matrix of correlators $C(t_i)$. We then solve the generalized eigenvalue problem to extract the eigenvalues as a function of time. We label them as

$$\lambda_k(t_i), \quad k = 0, 1, 2, ..., N, \quad i = 0, ..., T-1. \tag{3.35}$$

where k labels the energy level (assume we have an ordering relation for the eigenvalues for a fixed t_i) and i is the temporal index. The eigenvalue problem cannot really be solved configuration-by-configuration, so we have to use a resampling method to estimate the errors and cross-correlations between λ's. We will use jackknife here,

a method described later in this section. We will focus on fitting one particular eigenvalue, that is we fix k and fit $\lambda_k(t_i)$ to a model $f(t)$. Assume for now that we have an estimate of the *covariance matrix*

$$\widehat{\text{Cov}}_{ij} \approx \langle (\lambda_k(t_i) - \langle \lambda_k(t_i) \rangle)(\lambda_k(t_j) - \langle \lambda_k(t_j) \rangle) \rangle \, . \tag{3.36}$$

In our study we use for f either a single exponential function $f(t) = e^{-E(t-t_0)}$, or a double exponential $f(t) = ce^{-E(t-t_0)} + (1-c)e^{-E'(t-t_0)}$. These choices are imposed by the fact that the eigenvalues are expected to all be equal to 1 when $t = t_0$. For the discussion here, we denote the *fit parameters*—E in the first case, or E, E', and c in the second case—with $\boldsymbol{\alpha}$. For a choice $\boldsymbol{\alpha}$, the *residues* $\delta_i = \lambda_k(t_i) - f_{\boldsymbol{\alpha}}(t_i)$ are expected to be distributed normally

$$P(\delta) \propto e^{-\frac{1}{2}\delta_i \widehat{\text{Cov}}_{ij}^{-1}\delta_j} \, . \tag{3.37}$$

The best fit parameters are extracted using the *maximum likelihood* hypothesis. The estimators for $\boldsymbol{\alpha}$ are the ones that maximize $P(\delta)$, or equivalently minimize the χ^2-function:

$$\chi^2 = \delta_i \widehat{\text{Cov}}_{ij}^{-1}\delta_j \, . \tag{3.38}$$

The fit parameters that minimize χ^2-function will be denoted by $\hat{\boldsymbol{\alpha}}$. We can estimate the errors for the fit parameters using standard propagation of errors [54]:

$$\sigma(\hat{\alpha}_a)^2 = \sum_{c,d,i,j} 4H_{ac}^{-1}\frac{\partial f(t_i)}{\partial \alpha_c}(\hat{\boldsymbol{\alpha}})\widehat{\text{Cov}}_{ij}^{-1}\frac{\partial f(t_j)}{\partial \alpha_d}(\hat{\boldsymbol{\alpha}})H_{da}^{-1} \, , \tag{3.39}$$

Above H is the Hessian matrix

$$H_{ab} = \frac{\partial^2 \chi^2}{\partial \alpha_a \partial \alpha_b}(\hat{\boldsymbol{\alpha}}) \, . \tag{3.40}$$

Finally, the *goodness of the fit*—a measure of how likely it is that the model f describes the stochastic data—is estimated using the value of χ^2-function at the minimum and the number of degrees of freedom, that is the difference between the data-points used in the fit and the numbers of parameters in the fit. Assuming that the residues are normally distributed and the model is correct, the χ^2-value is expected to follow the distribution

$$P(\chi^2, d) = \frac{(\chi^2)^{d/2-1}}{2^{d/2}\Gamma(d/2)} e^{-\chi^2/2} , \tag{3.41}$$

where d is the number of degrees of freedom. The mean value of χ^2 is d and its variance is $2d$. Therefore, we expect that for a typical fit the χ^2-value is in the range $d \pm \sqrt{2d}$. A common rule-of-the-thumb is to call the fit good when χ^2/d is around 1. However, this criterion depends on the number of degrees of freedom in the fit. A more detailed estimate is provided by the *confidence level*

$$Q(d) = 1 - \int_0^{\chi^2_{meas}} P(\chi^2, d) d\chi^2 . \tag{3.42}$$

The confidence level represents the possibility, under the assumption that the fit function is good, of getting a value of χ^2 larger than the minimum value determined from the fit. We assume that the model is bad when $Q \leq 0.05$. Note that if Q is very close to 1, say $Q \geq 0.95$, this is also very unlikely. In this case, it is likely that the errorbars used in the fit were overestimated.

Jackknife resampling method

The raw input to our analysis, gauge configurations generated using HMC, are samples from a stochastic process. The final results of our project are complex functions of this raw input. To estimate the errors, we use *jackknife resampling*. Conceptually, the errors are defined as fluctuations of the final result with respect to resampling the

original raw input, that is a measure of how much the results are expected to vary if we were to generate a new set of configurations and repeat the measurement. Since this is impractical, the error estimate is produced by using an approximate (and cheap) resampling. Standard resampling methods used in error analysis are *bootstrap* [55] and *jackknife* [56].

To be specific, assume that the raw input are gauge configurations U_i, with $1 \leq i \leq N_{\text{conf}}$. The result of the analysis consists of a set of functions $\phi_k(\{U\})$ and we want to estimate the covariance matrix $C_{k,l} = \langle\!\langle \delta\phi_k \delta\phi_l \rangle\!\rangle$, where $\langle\!\langle \cdot \rangle\!\rangle$ is the average with respect to resampling and $\delta\phi_k = \phi_k(\{U\}) - \langle\!\langle \phi_k \rangle\!\rangle$. In particular, the error estimate for ϕ_k will be $\sqrt{C_{kk}}$. For example, ϕ_k's could be the energies E_k extracted by fitting eigenvalues of the correlation matrix $\lambda_k(t_i)$ to a single exponential fit $f(t) = \exp[-E(t - t_0)]$.

Binned jackknife resampling works the following way: We assume that the configurations are ordered according to the "simulation time", that is sequentially as they were produced by the stochastic process. We separate the sequence of configurations into N_{blocks} of size N_{bin} such that $N_{\text{blocks}} \times N_{\text{bin}} = N_{\text{conf}}$. For each $j = 1, \ldots, N_{\text{blocks}}$ we generate a sample $\{U\}_j$ by eliminating block j, that is configurations U_i with $(j-1) \times N_{\text{bin}} \leq i \leq j \times N_{\text{bin}}$ from the set $\{U\}$. We then compute the values of the functions ϕ_k's on these samples: $\phi_k^{(j)} \equiv \phi_k(\{U\}_j)$. Using these values, the covariance matrix is estimated by

$$C_{k,l} \approx \frac{N_{\text{blocks}} - 1}{N_{\text{blocks}}} \sum_{j=1}^{N_{\text{blocks}}} (\phi_k^{(j)} - \langle \phi_k \rangle)(\phi_l^{(j)} - \langle \phi_l \rangle), \quad \text{with} \quad \langle \phi_k \rangle \equiv \frac{1}{N_{\text{blocks}}} \sum_{j=1}^{N_{\text{blocks}}} \phi_k^{(j)}.$$
$$(3.43)$$

The bin size N_{bin} is chosen to be larger than the autocorrelation length. Measuring autocorrelation length is difficult, so in practice we increase the bin size until the error estimates stop increasing. Note that the size of the bin size should be relatively small, since the number of eigenvectors of the covariance matrix should be significantly larger

than the number of samples, in this case the number of bins. If we use too large a bin size, some of the eigenvalues of the covariance matrix become abnormally small leading to a breakdown in the χ^2-function minimization.

4 Scattering from Lattice QCD

Direct extraction of the scattering information from lattice QCD is impossible according to the "Maiani-Testa no-go theorem" [57]: In Euclidean field theories the long-time behavior of the relevant correlation functions is dominated by off-shell amplitudes and, as a result, the physical matrix elements cannot be extracted from Euclidean correlation functions with multi-hadron states. Two general approaches have been developed to evade the Mainai-Testa no-go theorem. Instead of directly calculating scattering amplitudes from lattice QCD, these two methods find a way to relate the discrete spectrum for two-particle states in finite volume to the phase shifts and the continuum scattering amplitude in the elastic region. The first method was proposed by Lellouch and Lüscher [58]. They found the relations between the Euclidean matrix elements measured in a finite volume and the continuum matrix elements of weak decays in Minkowski space. The other method was worked out by Lüscher [59]. He derived a formula connecting two-particle energy spectrum in a cubic box with periodic boundary conditions to scattering phase shifts in the continuum.

The plan for this chapter is the following: In Section 4.1 we will present a brief derivation of Lüscher formula. In Section 4.2 we will discuss how to choose a symmetry sector which couples to the channels we are interested in: the two-pion scattering channels $I(J^{PC}) = 1(1^{--})$ and $I(J^{PC}) = 0(0^{++})$. In addition, we discuss the extension to elongated boxes and states with non-zero total momentum. In section 4.3, we discuss the strategies used to fit the phase shifts to compute the resonance parameters. Finally, in Section 4.4 we present the interpolator basis for computing the two-pion

energy spectrum and the correlation functions that need to be evaluated.

4.1 Relation between two-particle spectrum and scattering phase shifts

In Ref. [59], Lüscher derived relations between the scattering phase shifts and the two-particle energy spectrum of a pair of spinless bosons on a 3D torus. The generalization of this relation for asymmetrical tori were introduced in Ref. [60]. To briefly demonstrate the derivation of Lüscher formula, let us consider a box with spatial volume

$$V = L \times L \times \eta L \,, \tag{4.1}$$

where η is real positive number controlling the elongation in one spatial direction. Periodic boundary conditions are imposed in all directions. Now we consider two spinless bosons in the box with identical mass m and zero total momentum. We can assume that they have short-range interaction with the potential satisfying

$$V(r) = 0 \quad \text{for} \quad r > R \,, \tag{4.2}$$

where r is the distance between the two particles. The Hamiltonian of this system is given by

$$H = -\frac{1}{2\mu}\Delta + V(r) \,, \tag{4.3}$$

where $\mu = \frac{m}{2}$ is the reduced mass of these two particles and Δ is the Laplacian with respect to $\mathbf{r}$, the relative position of the particles. We study the spectrum of these two particles in a finite volume box which is large enough to contain the interaction region. We solve the stationary Schrödinger equation

$$H\psi = E\psi \,, \tag{4.4}$$

where the state of this system is described by a scalar wave function $\psi(\mathbf{r})$. The potential that enters the Hamiltonian is a sum over all periodic images

$$V_L(\mathbf{r}) = \sum_{n \in \mathbb{Z}^3} V(|\mathbf{r} + n_i L_i|), \tag{4.5}$$

and the wave-function is periodic $\psi(\mathbf{r} + n_i L_i) = \psi(\mathbf{r})$. The wave function can be expanded into spherical harmonics

$$\psi(\mathbf{r}) = \sum_{l=0}^{\infty} \sum_{m=-l}^{l} Y_{lm}(\theta, \phi) \psi_{lm}(r). \tag{4.6}$$

In the non-interacting region Ω, where the potential is 0, the eigenfunctions obey the Helmholtz equation

$$(\Delta + k^2)\psi = 0, \quad \text{where} \quad E = \frac{k^2}{2\mu}. \tag{4.7}$$

After separating the variables, the radial part of Schrödinger equation is given by

$$\left(\frac{d^2}{dr^2} + \frac{2}{r}\frac{d}{dr} - \frac{l(l+1)}{r^2} + k^2 - 2\mu V(r) \right) \psi_{lm}(r) = 0, \tag{4.8}$$

The radial solution has only one linearly independent solution $u_l(r; k)$ which is normalized by imposing the boundary condition

$$\lim_{r \to 0} r^{-l} u_l(r; k) = 1. \tag{4.9}$$

For $r > R$, $u_l(r; k)$ is a linear combination of the spherical Bessel function of first kind $j_l(kr)$ and of second kind $n_l(kr)$ as

$$u_l(r; k) = \alpha_l(k) j_l(kr) + \beta_l(k) n_l(kr). \tag{4.10}$$

60

The whole solution for the Schrödinger equation can be written as

$$\psi_{lm}(r) = b_{lm}[\alpha_l(k)j_l(kr) + \beta_l(k)n_l(kr)], \quad r > R, \tag{4.11}$$

for some constants b_{lm}. In Ref. [59], it is shown that there is an one-to-one correspondence between a smooth periodic solution of the Helmholtz equation in region Ω and the eigenfunction of H in Ω. As a result, the eigenfunction of the Hamiltonian operator are entirely determined by their properties in the exterior region Ω. The general singular periodic solution of the Helmholtz equation are

$$G(\mathbf{r}, k^2) = \sum_{l=0}^{\infty} \sum_{m=-l}^{l} v_{lm} G_{lm}(\mathbf{r}, k^2), \tag{4.12}$$

with undetermined coefficients v_{lm}. G_{lm} is given by

$$G_{lm}(\mathbf{r}; k^2) = \frac{(-1)^l k^{l+1}}{4\pi} \left[Y_{lm}(\Omega)n_l(kr) + \sum_{l'm'} \mathcal{M}_{lm;l'm'} Y_{l'm'}(\Omega)j_{l'}(kr) \right]. \tag{4.13}$$

The matrix $\mathcal{M}_{lm,l'm'}$ plays a central role in analysis of the two-particle spectrum in finite volume, it is given by

$$\mathcal{M}_{lm,js} = \sum_{l'm'} \frac{(-1)^s i^{j-l} \mathcal{Z}_{l'm'}(1, q^2; \eta)}{\eta \pi^{3/2} q^{l'+1}} \sqrt{(2l+1)(2l'+1)(2j+1)}$$

$$\times \begin{pmatrix} l & l' & j \\ 0 & 0 & 0 \end{pmatrix} \begin{pmatrix} l & l' & j \\ m & m' & -s \end{pmatrix}, \tag{4.14}$$

where the standard Wigner $3j$ symbol is used, and $q = \frac{kL}{2\pi}$. The modified zeta functions considering the elongation effect in one direction of the box, are defined by

$$\mathcal{Z}_{lm}(s, q^2; \eta) = \sum_{\mathbf{n} \in \mathcal{Z}^3} \frac{\mathcal{Y}_{lm}(\tilde{\mathbf{n}})}{(\tilde{\mathbf{n}} - q^2)^s}, \tag{4.15}$$

61

where the harmonic polynomials are

$$\mathcal{Y}_{lm}(\tilde{\boldsymbol{n}}) = \tilde{n}^l Y_{lm}(\Omega_{\tilde{\boldsymbol{n}}}), \tag{4.16}$$

with $\mathbf{n} \in \mathbb{Z}^3$, $\tilde{\mathbf{n}} = (n_1, n_2, n_3/\eta)$. For real $k > 0$ and angular momentum l, the associated scattering phase is given by

$$e^{2i\delta_l(k)} = \frac{\alpha_l(k) + i\beta_l(k)}{\alpha_l(k) - i\beta_l(k)}. \tag{4.17}$$

As mention before, there is a one-to-one correspondence between the eigenfunction of the Hamiltonian and the solution of the Helmholtz equation in the non-interaction region Ω. Matching the coefficients in Eq. 4.11 with the coefficients in Eq. 4.13, one finds

$$
\begin{aligned}
b_{lm}\alpha_l(k) &= \sum_{l'=0}^{\infty} \sum_{m'=-l'}^{l'} v_{l'm'} \frac{(-1)^{l'} k^{l'+1}}{4\pi} \mathcal{M}_{l'm',lm}, \\
b_{lm}\beta_l(k) &= v_{lm} \frac{(-1)^l k^{l+1}}{4\pi}.
\end{aligned}
\tag{4.18}
$$

We can use the second equation to eliminate v_{lm}. Then one is left with a homogeneous linear system for coefficients b_{lm}. Since the number of equations is equal to the number of unknowns, a non-zero solution exists if and only if the associated determinant vanishes. Finally, we obtain the general relation between the two-particle spectrum and the scattering phase shifts which is given by

$$\det\left[e^{2i\delta} - U\right] = 0, \quad \text{where} \quad U = (\mathcal{M} + i)/(\mathcal{M} - i), \tag{4.19}$$

where $e^{2i\delta}$ is a diagonal matrix with elements $e^{2i\delta_l}$. We notice that this relation contains the phase shifts for different angular momenta. A truncation is required, usually justified by the assumption that the phase shift for higher partial waves are

negligible at small energy.

4.2   Symmetry reduction

In this section, we mainly focus on discussing how to apply Eq. 4.19 to match our energy spectrum so as to derive a simple relation between the low-lying energy levels in the elongated box and scattering phase shifts. In particular, we are interested in the $I(J^{PC}) = 1(1^{--})$ and $I(J^{PC}) = 0(0^{++})$ channels for two-pion scattering.

As mentioned in section 3.2, the D_{4h} group has five irreps. The energy eigenfunctions calculated on the lattice belong to one of the five irreps, and couple to an infinite number of angular momentum J (see Table 3.5). For the ρ meson which is in $1(1^{--})$ channel of two-pion scattering, we want to pick up one of the five irreps which overlaps with $J = 1$ and higher partial-waves. From Table 3.5, we see that A_2 and E irreps satisfy this condition.

The two-pion states represent particles moving back-to-back since the total momentum is zero. The lowest energy states in the A_2 and E channels represent particles moving with one unit of momentum along the elongated direction for A_2 and along the transversal direction for E (there are two such states, hence the irrep is two-dimensional). We used the A_2 irrep since the momentum along the elongated direction changes as we increase the elongation, allowing us to scan the resonance region in detail. In addition, the parity of the representation also needs to be taken into consideration. Since ρ meson has odd parity, we work out the scattering formula in the A_2^- representation.

It is sufficient to consider the system with a finite angular momentum cutoff $J \leq \Lambda$. One can show that after introducing a finite angular momentum cutoff, the relation between the scattering phase shifts and energy spectrum, as shown in Eq. 4.19, is unchanged. In this case, instead of studying Eq. 4.19 in angular momentum J representation space, now we study it in reduced representation space $\mathcal{H}_\Lambda$ which has

$(\Lambda + 1)^2$ dimensions. The finite number of J representation in $\mathcal{H}_\Lambda$ can be decomposed into irreducible representations in the O_h or D_{4h} group which is shown in Table 3.4. We label the basis for the nth occurrence of the representation Γ as

$$|\Gamma, \alpha; J, n\rangle \text{ with } \alpha = 1, ..., \dim \Gamma, \tag{4.20}$$

where $n = 1, 2, ..., N(\Gamma, J)$ and $N(\Gamma, J)$ represents the multiplicity of the irreducible representation Γ in the decomposition of the reduced space $\mathcal{H}_\Lambda$. The reason we choose to use this basis is that the transformation matrices representing the action of the O or D_{4h} group are independent of J and n. Now Eq. 4.19 can be studied in the reduced space $\mathcal{H}_\Lambda$

$$\det\left[e^{2i\delta} - U\right] = 0, \quad \text{where } U = (M(\Gamma) + i)/(M(\Gamma) - i), \tag{4.21}$$

and $M(\Gamma)$ is the reduced matrix. Its elements can be written in terms of $\mathcal{M}_{lm,l'm'}$ as

$$\langle \Gamma, \alpha, n | M(\Gamma) | \Gamma, \alpha', n'\rangle = \sum_{J=0}^{\Lambda} \sum_{J'=0}^{\Lambda} \sum_{m=-J}^{J} \sum_{m'=J'}^{J'} \langle \Gamma, \alpha, n | J, m\rangle \langle J'm' | \Gamma, \alpha', n'\rangle \mathcal{M}_{Jm,J'm'}. \tag{4.22}$$

For practical calculation, we assume that the lowest angular momentum in the channel dominates. Because of this, we can first consider the case where only the lowest two angular momenta contribute and then check whether we need to consider the contribution of the second lowest angular momentum. In the A_2^- representation, the lowest two angular momentum are $J = 1$ and $J = 3$ (see Table 3.5). If we include the partial waves for $J = 1$, and 3 we have

$$M(\Gamma) = \begin{pmatrix} m_{11} & m_{13} \\ m_{31} & m_{33} \end{pmatrix}, \tag{4.23}$$

where $m_{JJ'}$ in this case represents the matrix element $M(A_2^-)_{J1,J'1}$. In this case, Eq. 4.19 is written out as

$$\begin{vmatrix} e^{2i\delta_1}(m_{11} - i) - (m_{11} + i) & (e^{2i\delta_1} - 1)m_{13} \\ (e^{2i\delta_3} - 1)m_{31} & e^{2i\delta_3}(m_{33} - i) - (m_{33} + i) \end{vmatrix} = 0 . \quad (4.24)$$

Using $m_{JJ'} = m_{J'J}$, the equation can be further simplified to

$$\left[e^{2i\delta_1}(m_{11} - i) - (m_{11} + i)\right]\left[e^{2i\delta_3}(m_{33} - i) - (m_{33} + i)\right] = m_{13}^2(e^{2i\delta_1} - 1)(e^{2i\delta_3} - 1) . \quad (4.25)$$

In practice, the phase shifts for $J = 3$ are very small when we consider the low-lying energy spectrum. Therefore, we can safely assume that $\delta_3 = 0$. The equation above becomes

$$e^{2i\delta_1} = \frac{m_{11} + i}{m_{11} - i} , \quad (4.26)$$

which can be simplified as

$$\cot\delta_1 = m_{11} = \mathcal{W}_{00} + \frac{2}{\sqrt{5}}\mathcal{W}_{20} , \quad (4.27)$$

where

$$\mathcal{W}_{lm}(1, q^2; \eta) = \frac{\mathcal{Z}_{lm}(1, q^2; \eta)}{\pi^{3/2}\eta q^{l+1}} . \quad (4.28)$$

The normalized pion momentum q is defined in terms of the pion momentum k,

$$q = \frac{kL}{2\pi} \quad \text{with} \quad E = 2\sqrt{m_\pi^2 + k^2} , \quad (4.29)$$

where E is the energy of the system and m_π is the pion mass.

Similarly, we work out Lüshcer's formula for studying σ resonance phase shifts in $I(J^{PC}) = 0(0^{++})$ scattering channel. The corresponding irreps for the s-wave scattering channel is the A_1^+ in both the O_h and D_{4h} group. The A_1^+ in D_{4h} couples to

angular momentum $J = 0, 2, 4....$ Using the same argument for the angular momentum cutoff we discussed above, we assume that the contribution from the $J > 0$ is negligible. As a result, we consider the A_1^+ irrep under the condition that it is dominated by $J = 0$. The Lüscher's formula in A_1^+ is given by

$$\cot \delta_0 = \mathcal{W}_{00} = \frac{\mathcal{Z}_{00}(1, q^2; \eta)}{\pi^{3/2} \eta q} . \tag{4.30}$$

Each box geometry can be used to compute the phase shift at a two-three kinematic points when we consider only zero-momentum states. To add more data points we consider two-particle state with non-zero momentum. This requires a slight modification of the quantization condition derived above (Lüscher's formula). For boosted states with total momentum $\boldsymbol{P}$, the relativistic effects contract the box along the boost direction [61]. In the case of an elongated box, a boost in a generic direction will further reduce the symmetry group from D_{4h} to a subgroup which depends on the direction of the boost. In this study, we consider states that have a non-zero momentum parallel with the elongated direction. In this case, the length contraction affects only the elongated direction. Therefore the boost does not change the rotational symmetry group which is still D_{4h}. As a result, we can still focus on the A_2^- irrep and use the same phase shifts formula as in Eq. 4.27 with a slight modification.

For the boosted states in a cubic box with momentum $\boldsymbol{P} = (2\pi/L)\boldsymbol{d}$, where $\boldsymbol{d}$ is a triplet of integers, the relevant zeta function is

$$\mathcal{Z}_{lm}^{\boldsymbol{d}}(s; q, \gamma) = \sum_{\boldsymbol{n} \in P_{\boldsymbol{d}}(\gamma)} \frac{\mathcal{Y}_{lm}(\boldsymbol{n})}{(\boldsymbol{n}^2 - q^2)^s}, \tag{4.31}$$

where

$$P_d(\gamma) = \left\{ \boldsymbol{n} \in \mathbb{R}^3 \mid \boldsymbol{n} = \hat{\gamma}^{-1} \left(\boldsymbol{m} + \frac{\boldsymbol{d}}{2} \right), \boldsymbol{m} \in \mathbb{Z}^3 \right\} . \tag{4.32}$$

The projector $\hat{\gamma}^{-1}$ is defined as

$$\hat{\gamma}^{-1}\boldsymbol{n} = \boldsymbol{n}_\parallel/\gamma + \boldsymbol{n}_\perp, \boldsymbol{n}_\parallel = \boldsymbol{v}(\boldsymbol{n}\cdot\boldsymbol{v})/\boldsymbol{v}^2 \text{ and } \boldsymbol{n}_\perp = \boldsymbol{n} - \boldsymbol{n}_\parallel. \tag{4.33}$$

The Lorentz boost factor γ can be obtained from the velocity of the boost: $\gamma = 1/\sqrt{1-\boldsymbol{v}^2}$, where $\boldsymbol{v} = \boldsymbol{P}/E$. The energy in the center-of-mass frame is related the energy in the lab frame

$$E_{\mathrm{CM}} = E/\gamma. \tag{4.34}$$

The phase shift formula is the same as in Eq. 4.27 but with a modified $\mathcal{W}$

$$\mathcal{W}_{lm}(1,q^2;\gamma) = \frac{\mathcal{Z}_{lm}^{\boldsymbol{d}}(1,q^2;\gamma)}{\pi^{\frac{3}{2}}\gamma q^{l+1}}. \tag{4.35}$$

We extend now the phase shift formula to boosted states in an elongated box, with the boost in the elongated direction. The only effect of the elongation is that the summation region $P_{\boldsymbol{d}}(\gamma)$ changes to

$$P_{\boldsymbol{d}}(\gamma,\eta) = \left\{\boldsymbol{n}\in\mathbb{R}^3 \mid \boldsymbol{n} = \hat{\gamma}^{-1}\hat{\eta}^{-1}(\boldsymbol{m}+\frac{1}{2}\boldsymbol{d}), \boldsymbol{m}\in\mathbb{Z}^3\right\}, \tag{4.36}$$

with $\hat{\eta}^{-1}\boldsymbol{m} = (m_x, m_y, m_z/\eta)$, assuming that the boost and elongation are in the z-direction.

To evaluate the phase shift formula in Eq. 4.27, we need to compute $\mathcal{Z}_{00}^{\boldsymbol{d}}(s=1)$ and $\mathcal{Z}_{20}^{\boldsymbol{d}}(s=1)$. The zeta functions as defined in Eq. 4.15 and Eq. 4.31 diverge at $s=1$ and we need to compute them via an analytical continuation. The details for evaluating these functions are presented in the Appendix A.

4.3 Resonance parametrization

Lüscher's formula allows us to compute phase shifts using the two-particle finite volume energies extracted from Lattice QCD. To extract the resonance parameters, we have to parametrize these phase shifts as a function of energy. In this section we discuss first the general framework for such parametrizations and then specific models.

The extracted phase shifts carry in principle full information about the interaction of (unphysically heavy) pions at discrete values of energy (or momentum) above and even below the corresponding $\pi\pi$-threshold. From the point of view of scattering theory these points are interconnected by a function of energy which carries specific analytic properties. These properties are the guiding principle for the construction of fit functions to extract its parameters from lattice data. Specifically, given the S-matrix and scattering amplitude T for two-to-two scattering with $S = 1 + i\,T$, the unitarity constraints the imaginary part of the scattering amplitude to

$$\operatorname{Im} T_{IL}^{-1}(s) = \frac{\rho(s)}{16\pi} \,, \tag{4.37}$$

where the projection to definite isospin (I) and angular momentum (L) is assumed (see Appendix B for projection formulas). Here s denotes the square of the total four-momentum of the system and $\rho(s) = \sqrt{1 - 4M_\pi^2/s}$ is the two-pion phase-space factor. The equation above does not fix the amplitude entirely, but only up to a real-valued function

$$T_{IL}(s) = \frac{16\pi}{K_{IL}^{-1}(s) + i\,\rho(s)} \,, \quad \text{or} \quad \tan\delta_{IL} = -\rho(s)K_{IL}(s) \,, \tag{4.38}$$

where $K_{IL}(s)$ is called K-Matrix, referring to the possibility of multiple interaction channels involved in the scattering process. In this work we will use a number of different versions of the K-Matrix to gauge the systematic uncertainty tied to a

particular choice.

The parameters for these models can be constrained using our lattice data by fitting the energies directly using the following method: The energies E_k satisfying both equations Eq. 4.38 and Eq. 4.27 are the expected eigenvalues of the Hamiltonian on periodic boxes with geometry $L^2 \times \eta L$. These solutions are functions of the geometry of the box η and the parameters of the given model, we will denote them with $E_k(m_\rho, g_{\rho\pi\pi}; \eta)$. To determine the fit parameters we minimize the χ^2-function

$$\chi^2(m_\rho, g_{\rho\pi\pi}) = \sum_e \delta_e^T C_e^{-1} \delta_e \,, \tag{4.39}$$

where the sum runs over the statistically independent ensembles with different elongations and the residue vector is given by

$$(\delta_e)_k = E_k(m_\rho, g_{\rho\pi\pi}; \eta_e) - E_k^{(e)} \,. \tag{4.40}$$

Above we denote with $E_k^{(e)}$ the kth energy extracted from ensemble e and with C_e the covariance matrix for these energies. Note that the residue vector includes the residues for both zero-momentum states and boosted-states and thus it has between 6 and 8 entries depending on the ensemble considered. The details for the energy levels for each ensemble will be discussed in Chapter 5. The energies are extracted using individual correlated fits and the covariance matrices are estimated using a jackknife analysis.

Breit Wigner form for resonance

Assuming we have finished calculating the phase shifts pattern, the next step is to find a physical model to parameterize the phase shifts pattern. To extract the mass and width of the resonance we need to fit the phase-shift data using a phase-shift parametrization in the resonance region. For the ρ-resonance a Breit-Wigner

parametrization

$$\tan\delta(E) = \frac{E\,\Gamma(E)}{m_\rho^2 - E^2} \quad \text{with} \quad \Gamma(E) = \frac{g_{\rho\pi\pi}^2}{6\pi}\frac{p^3}{E^2} \tag{4.41}$$

describes the phase shift well enough, in the energy region close to the resonance. For a given box geometry, this parametrization can be used to estimate the eigenvalues of the Hamiltonian using Lüscher's formula for the A_2^- irrep in Eq. 4.27.

Conformal mapping

When we study the σ resonance, it is difficult to use the Breit-Wigner form to describe its resonance behavior. The difficulty comes from the especially short life time the σ which cause it to lack the simple narrow "bump" signature associated with longer-lived resonance. In this section, we will discuss another approach, *conformal mapping*, to parameterize the σ-resonance.

First, we assume the most general form of K-Matrix as an analytic (polynomial) function of energy. However, as discussed in Ref. [62, 63] the convergence of a power series in energy variable can be strongly improved, mapping it conformally onto the interior of a disk. The expansion variable reads in this case

$$\omega(s) = \frac{\sqrt{s} - \alpha\sqrt{4M_\circ - s}}{\sqrt{s} + \alpha\sqrt{4M_\circ - s}}, \tag{4.42}$$

where α and $M_\circ$ are internal parameters of the mapping. α is fixed by fitting to the data and $M_\circ$ can be set conveniently (for example $M_\circ$ is set to m_K^2, the kaon mass, in Ref. [62]). Furthermore, for the scalar, isoscalar channel ($I = J = 0$) chiral symmetry dictates that $T_{00}(s)$ must vanish for a $s \equiv s_A < 4M_\pi^2$. To account for this the form of the K-Matrix in this channel reads

$$K_{00}^{-1}(s) = \frac{M_\pi^2}{s - s_A}\left(\frac{2s_A}{M_\pi\sqrt{s}} + \sum_{i=1}^{3} B_i\omega^i(s)\right), \tag{4.43}$$

70

where throughout the further calculations s_A is set to its leading chiral order value, i.e. $2s_A = M_\pi^2$.

In principle the number of polynomial terms in the latter equations ($\sim B_i$) is not restricted a priori. For the present case of the σ resonance three polynomial terms turn out to give sufficient flexibility in the energy variable $\omega(s)$. The four free parameters (α, B_1, B_2, B_3) are adjusted to reproduce the obtained lattice data at each pion mass separately.

UχPT formalism

The Breit Wigner and conformal mapping parameterizations have an important disadvantage when describing lattice result. Namely that neither extrapolation between different pion masses nor combined description of different interaction channels (e.g. σ and ρ) is possible. For this reason, the use of information from Chiral Perturbation Theory [64, 65] is advantageous.

Technically, the K-Matrix is derived in this case from the next-to-leading chiral order. Therefore, it can be expected that it has the correct behavior as a function for small pion mass. Furthermore, since it relies on a Lagrangian theory it is capable of universally describing various channels of the $\pi\pi$ system. In other words, data from ρ and σ channels can be fitted by the same free parameters. Such a treatment has been employed in many analyses, such as the so-called Unitarized Chiral Perturbation Theory (UχPT), see e.g. Refs. [2, 66]. Additionally, an extension to three-flavor sector allows to use such a parametrization to estimate the size of the corrections associated with the missing strange quark in our calculation.

In the language of UχPT the manifestly unitary scattering amplitude for $\pi\pi$-scattering reads

$$T_{IL}(s) = \frac{1}{V_{IL}^{-1}(s) - G(s)}, \qquad (4.44)$$

71

where $V(s)$ is the chiral potential and $G(s)$ is the two-pion loop function defined via

$$G(s) = i \int \frac{d^4 q}{(2\pi)^4} \frac{1}{q^2 - m_\pi^2 + i\epsilon} \frac{1}{(P - q)^2 - m_\pi^2 + i\epsilon}, \tag{4.45}$$

where P is the total four-momentum of the system. Note that this equation corresponds exactly to the parametrization Eq. 4.38 after re-shuffling the real part of the loop-function G into the K-Matrix and making the appropriate normalization. The chiral potential including contract terms up to next-to-leading order (NLO) reads for the two channels

$$V_{11}(s) = \frac{4m_\pi^2 - s}{6(f_\pi^2 - 8\,\hat{l}_1 m_\pi^2 + 4\,\hat{l}_2 s)}, \tag{4.46}$$

$$V_{00}(s) = \frac{3(m_\pi^2 - 2s)^2}{6f_\pi^2(m_\pi^2 - 2s) + 8(L_a m_\pi^4 + s(L_b m_\pi^2 + L_c s))}. \tag{4.47}$$

Here $p = \sqrt{s/4 - m_\pi^2}$ is the magnitude of the center-of-mass three momentum, and f_π denotes the pion decay constant that itself is a function of the pion mass. Furthermore, $\hat{l}_1, \hat{l}_2, L_a, L_b, L_c$ are linear combinations (see Appendix B) of the next to leading chiral order low-energy constants $\{L_i | i = 1, .., 8\}$.

4.4   Interpolators and correlation functions

In this section, we concentrate on constructing the interpolators we used in the variational basis and work out their corresponding two-point correlation functions. We will first present the details for the ρ resonance in $I(J^{PC}) = 1(1^{--})$ channel and then the σ-meson channel, $I(J^{PC}) = 0(0^{++})$.

$I(J^{PC}) = 1(1^{--})$ **channel**

As we explained earlier we focus on the states in the A_2^- irrep, mainly because the lowest states in this channel correspond to scattering states where the pions move in

the elongated direction of the box. The energy of these states changes as we increase the elongation and we can scan the resonance region. For the volumes considered in this study, the elastic region, $E < 4m_\pi$, contains only the lowest three or four states and our focus will be on designing a set of interpolators that allows us to compute the energies of these states accurately. Note that as the pion mass becomes lower and the volume is increased there are more multi-hadron states in the elastic scattering energy region and the basis would need to be adjusted accordingly.

To extract these states we need a basis that overlaps both with the resonance state, which is expected to have mainly a quark-antiquark content, and also with the states that have a dominant two-pion content. From a numerical point of view, the quark-antiquark interpolators are advantageous, since they lead after Wick contraction to two-point quark-correlation functions which can be evaluated cheaply using lattice QCD techniques. The four quark-antiquark interpolators are of the form

$$\rho^0(\Gamma_i(\boldsymbol{p}), t) = \frac{1}{\sqrt{2}}\left[\bar{u}(t)\Gamma_i(\boldsymbol{p})u(t) - \bar{d}(t)\Gamma_i(\boldsymbol{p})d(t)\right]. \tag{4.48}$$

Here we consider $u(t)$ and $d(t)$ to be the quark field on the entire t time slice, a column vector of size $N = 12 \times N_x \times N_y \times N_z$, and $\Gamma_i(\boldsymbol{p})$ to be $N \times N$ matrices. To help with notation we define $\Gamma_i'(\boldsymbol{p})$ using

$$[\rho^0(\Gamma_i(\boldsymbol{p}), t)]^\dagger = \rho^0(\Gamma_i'(\boldsymbol{p}), t). \tag{4.49}$$

The structure of $\Gamma_i(\boldsymbol{p})$ for the quark-antiquark interpolators is listed in the first four rows of Table 4.1. The first four rows are used for the quark-antiquark interpolators and the last row is used for the pion-pion interpolators. The elongation is assumed to be in the z-direction and the interpolators are chosen so that the ρ polarization is longitudinal: γ_3 and ∇_3 need to be changed accordingly if the elongation direction is changed. Two of the $q\bar{q}$ interpolators are point-like and differ only in the gamma-matrix

i	$\Gamma_i(\boldsymbol{p})$	$\Gamma'_i(\boldsymbol{p})$
1	$\gamma_3 e^{i\boldsymbol{p}}$	$\gamma_3 e^{-i\boldsymbol{p}}$
2	$\gamma_4\gamma_3 e^{i\boldsymbol{p}}$	$\gamma_4\gamma_3 e^{-i\boldsymbol{p}}$
3	$\gamma_3\nabla_j e^{i\boldsymbol{p}}\nabla_j$	$-\gamma_3\nabla_j e^{-i\boldsymbol{p}}\nabla_j$
4	$\frac{1}{2}\{e^{i\boldsymbol{p}},\nabla_3\}$	$-\frac{1}{2}\{e^{-i\boldsymbol{p}},\nabla_3\}$
5	$\gamma_5 e^{i\boldsymbol{p}}$	$-\gamma_5 e^{-i\boldsymbol{p}}$

Table 4.1: Interpolator structure for the quark bilinears used in this study.

structure and the other two involve a covariant derivative

$$(\nabla_k)^{ab}_{x,y} = U_k^{ab}(x)\delta_{x+\hat{k},y} - \delta^{ab}\delta_{x,y}\,, \tag{4.50}$$

and they involve quark-antiquark pairs separated by one lattice spacing.

Unfortunately, the quark-antiquark interpolators overlap very poorly with the multi-hadron state (the overlap is suppressed by a power of the lattice volume [14]). Therefore we have to include also pion-pion interpolators in our basis. The pion-pion interpolators are constructed to have isospin $I = 1$ and $I_3 = 0$, corresponding to ρ^0:

$$\pi\pi(\boldsymbol{p}_1,\boldsymbol{p}_2) = \frac{1}{\sqrt{2}}\{\pi^+(\boldsymbol{p}_1)\pi^-(\boldsymbol{p}_2) - \pi^-(\boldsymbol{p}_1)\pi^+(\boldsymbol{p}_2)\}\,. \tag{4.51}$$

Here we use

$$\pi^-(\boldsymbol{p},t) = \sum_{\boldsymbol{x}} \bar{u}(\boldsymbol{x},t)\gamma_5 d(\boldsymbol{x},t)e^{i\boldsymbol{p}\boldsymbol{x}} = \bar{u}(t)\Gamma_5(\boldsymbol{p})d(t)\,,$$
$$\pi^+(\boldsymbol{p},t) = \sum_{\boldsymbol{x}} \bar{d}(\boldsymbol{x},t)\gamma_5 u(\boldsymbol{x},t)e^{i\boldsymbol{p}\boldsymbol{x}} = \bar{d}(t)\Gamma_5(\boldsymbol{p})u(t)\,. \tag{4.52}$$

To construct interpolators transforming according to the A_2^- representation, we can start with any interpolator that has some A_2^- component and projects onto the

relevant subspace:

$$\pi\pi(\boldsymbol{p}_1, \boldsymbol{p}_2)_{A_2^-} = \frac{1}{|D_{4h}|} \sum_{g \in D_{4h}} \chi_{A_2^-}(g) \pi\pi(R(g)\boldsymbol{p}_1, R(g)\boldsymbol{p}_2), \qquad (4.53)$$

where $R(g)$ implements the rotation associated with the symmetry transformation g, and $\chi_{A_2^-}$ is the character of g in the A_2^- irrep.

For states with zero total momentum, $\boldsymbol{P}_0 = \boldsymbol{p}_1 + \boldsymbol{p}_2 = 0$ and for non-zero momentum states with $\boldsymbol{P}_1 = (0, 0, 1)$ we use the following interpolators

$$\begin{aligned}
\pi\pi_{001}^{(i)} &= \pi\pi(\boldsymbol{p}_1 = (0, 0, 1), \boldsymbol{p}_2 = \boldsymbol{P}_i - \boldsymbol{p}_1), \\
\pi\pi_{002}^{(i)} &= \pi\pi(\boldsymbol{p}_1 = (0, 0, 2), \boldsymbol{p}_2 = \boldsymbol{P}_i - \boldsymbol{p}_1), \qquad (4.54) \\
\pi\pi_{011}^{(i)} &= \frac{1}{2} \sum_{p_1 \in \mathcal{P}} \pi\pi(\boldsymbol{p}_1, \boldsymbol{p}_2 = \boldsymbol{P}_i - \boldsymbol{p}_1),
\end{aligned}$$

where $\mathcal{P} = \{(0, 1, 1), (1, 0, 1), (-1, 0, 1), (0, -1, 1)\}$, is the set of momenta generated by symmetry transformations $R(g)\boldsymbol{p}$ from $\boldsymbol{p} = (0, 1, 1)$ which have $p_z > 0$. The latter condition is imposed for different reasons for the $\pi\pi^{(0)}$ and $\pi\pi^{(1)}$ interpolators. In the zero momentum case we impose it because the interpolators $\pi\pi(\boldsymbol{p}, -\boldsymbol{p})$ and $-\pi\pi(-\boldsymbol{p}, \boldsymbol{p})$ are identical. The details for the Clebsch-Gordan coefficients for different scattering momentum combination can be found in the Appendix of Ref. [67].

For non-zero momentum, the symmetry group transformations mix states with different total momentum, $\boldsymbol{P}_1$ and $-\boldsymbol{P}_1$. When computing the correlation functions of such interpolating fields, the correlation functions between sink and source of different momentum vanish. The non-vanishing contributions connect states with the same total momentum. The expectation values for correlations functions associated with momentum $\boldsymbol{P}_1$ and $-\boldsymbol{P}_1$ are the same due to symmetry, so we only need to evaluate the contributions due to momentum $\boldsymbol{P}_1$.

The same interpolators for the non-zero momentum case can also be derived using

an analysis based on symmetries of the Poincare group on the lattice [68]. In our case the little group for states with momentum $\boldsymbol{P}_1$ is C_{4v} and the relevant irrep is A_1 since the longitudinal states have projection 0^+ in the momentum direction. We prefer to derive them from projections onto the A_2^- irrep of D_{4h} to make clear that the connection between energies and phase shifts is provided by the relation in Eq. 4.27.

To summarize, we use four quark-antiquark interpolators and two pion-pion interpolators for most ensembles to form a 6×6 variational basis. The correlation matrix is constructed from interpolators ρ_k, with $k = 1, \ldots, 4$ corresponding to the first four rows of Table 4.1, $\pi\pi_{001}$, and $\pi\pi_{011}$. For some ensemble, we add a third pion interpolator $\pi\pi_{002}$, for reasons that will be explained later. In principle, six or seven energies can be extracted from the correlation matrix. However, we only focus on the first three lowest energy levels that are located in the elastic scattering region with better signal-to-noise ratio.

The next step is to calculate the correlation matrix, which contains all the combination of the two interpolators. As we discussed in section 3.2, the correlation function is calculated using the Wick theorem. In the following, we work out the explicit formula for the correlation matrix. Now we need to evaluate the correlation function with $q\bar{q}$ to $q\bar{q}$, $\pi\pi$ to $q\bar{q}$ and $\pi\pi$ to $\pi\pi$ interpolators. An estimate for $C(t)$ is obtained by taking the average over a representative ensemble of gauge links generated by the method

described in section 2.4. The correlation matrix will have then three types of entries

$$C_{\rho_i \leftarrow \rho_j} = \left\langle \rho_i(\boldsymbol{P}, t_f) \rho_j^\dagger(\boldsymbol{P}, t_i) \right\rangle = - \left\langle [i\boldsymbol{P}f|j'\boldsymbol{P}i] \right\rangle,$$

$$C_{\rho_i \leftarrow \pi\pi} = \left\langle \rho_i(\boldsymbol{P}, t_f) \pi\pi(\boldsymbol{p}, \boldsymbol{P} - \boldsymbol{p}, t_i)^\dagger \right\rangle$$

$$= \left\langle [i\boldsymbol{P}f|5'\boldsymbol{P} - \boldsymbol{p}i|5'\boldsymbol{p}i] - [i\boldsymbol{P}f|5'\boldsymbol{p}i|5'\boldsymbol{P} - \boldsymbol{p}i] \right\rangle,$$

$$C_{\pi\pi \leftarrow \pi\pi} = \left\langle \pi\pi(\boldsymbol{p}', \boldsymbol{P} - \boldsymbol{p}', t_f) \pi\pi(\boldsymbol{p}, \boldsymbol{P} - \boldsymbol{p}, t_i)^\dagger \right\rangle$$

$$= \left\langle [5\boldsymbol{p}'f|5\boldsymbol{P} - \boldsymbol{p}'f|5'\boldsymbol{p}i|5'\boldsymbol{P} - \boldsymbol{p}i] \right.$$

$$\qquad (4.55)$$

$$- [5\boldsymbol{p}'f|5\boldsymbol{P} - \boldsymbol{p}'f|5'\boldsymbol{P} - \boldsymbol{p}i|5'\boldsymbol{p}i]$$

$$+ [5\boldsymbol{P} - \boldsymbol{p}'f|5\boldsymbol{p}'f|5'\boldsymbol{P} - \boldsymbol{p}i|5'\boldsymbol{p}i]$$

$$- [5\boldsymbol{P} - \boldsymbol{p}'f|5\boldsymbol{p}'f|5'\boldsymbol{p}i|5'\boldsymbol{P} - \boldsymbol{p}i]$$

$$+ [5\boldsymbol{p}'f|5'\boldsymbol{p}i][5\boldsymbol{P} - \boldsymbol{p}'f|5'\boldsymbol{P} - \boldsymbol{p}i]$$

$$\left. - [5\boldsymbol{p}'f|5'\boldsymbol{P} - \boldsymbol{p}i][5\boldsymbol{P} - \boldsymbol{p}'f|5'\boldsymbol{p}i] \right\rangle.$$

Above we used the following notation for the traces produced by Wick contractions

$$[i_1\boldsymbol{p}_1 j_1| \ldots |i_k\boldsymbol{p}_k j_k] \equiv \mathrm{Tr} \prod_{\alpha=1}^{k} \Gamma_{i_\alpha}(\boldsymbol{p}_\alpha) M^{-1}(t_{j_\alpha}, t_{j_{\alpha+1}}), \qquad (4.56)$$

where j_{k+1} is defined to be j_1 and $M^{-1}(t, t') = \langle u(t)\bar{u}(t') \rangle$ is the quark propagator between time slices t and t', viewed as a $N \times N$ matrix (for more details about the notation see [11]). Note that $\Gamma_{i'}(\boldsymbol{p})$ is meant to be $\Gamma_i'(\boldsymbol{p})$. In order to discuss each term's contributions to the correlation matrix, we use quark diagrams to visualize the components of the correlation functions (see Ref. [11]). The following diagrams are in one-to-one correspondence to the components in Eq. 4.55:

$$C_{\rho_i \leftarrow \rho_j} = - \left\langle \; \right\rangle, \qquad (4.57)$$

77

$$C_{\rho_i \leftarrow \pi\pi} = \left\langle \; \triangle - \triangle \; \right\rangle , \tag{4.58}$$

$$C_{\pi\pi \leftarrow \pi\pi} = \left\langle \; \boxtimes - \square + \boxtimes - \square + \; \text{◊◊} - \bigotimes \; \right\rangle . \tag{4.59}$$

We notice that when $\boldsymbol{P} = 0$, one can prove using parity symmetry that the counter-clockwise diagrams have the same value as the clockwise diagrams after taking the gauge average:

$$\left\langle \; \triangle \; \right\rangle = - \left\langle \; \triangle \; \right\rangle , \quad \left\langle \; \square \; \right\rangle = \left\langle \; \square \; \right\rangle , \quad \left\langle \; \boxtimes \; \right\rangle = \left\langle \; \boxtimes \; \right\rangle . \tag{4.60}$$

Therefore the number of diagrams that needs to be evaluated is reduced to one for three-point functions and to four for four-point functions.

The two-point quark diagrams can be evaluated cheaply by computing the quark propagator from one point on the lattice and using the translational invariance. This is not possible for three- and four-point diagrams. We use the LapH method mentioned in section 3.3 to solve this problem. The traces in Eq. 4.56 are then replaced with a smeared version

$$[\![i_1 \boldsymbol{p}_1 j_1 | \ldots | i_k \boldsymbol{p}_k j_k]\!] \equiv$$
$$= \mathrm{Tr} \prod_{\alpha=1}^{k} \Gamma_{i_\alpha}(\boldsymbol{p}_\alpha) S(t_{j_\alpha}) M^{-1}(t_{j_\alpha}, t_{j_{\alpha+1}}) S(t_{j_{\alpha+1}}) \tag{4.61}$$
$$= \mathrm{Tr} \prod_{\alpha=1}^{k} \tilde{\Gamma}_{i_\alpha}(\boldsymbol{p}_\alpha, t_{j_\alpha}) \tilde{M}^{-1}(t_{j_\alpha}, t_{j_{\alpha+1}}) ,$$

where

$$\tilde{\Gamma}_i(\boldsymbol{p}, t)^{\alpha\beta}_{s,s'} \equiv \left\langle s; t \left| \Gamma_i(\boldsymbol{p})^{\alpha\beta} \right| s'; t \right\rangle ,$$
$$\tilde{M}^{-1}(t, t')^{\alpha\beta}_{s,s'} \equiv \left\langle s; t \left| M^{-1}(t, t')^{\alpha\beta} \right| s'; t' \right\rangle \tag{4.62}$$

i	$\Gamma_i(\boldsymbol{p})$	$\Gamma'_i(\boldsymbol{p})$
1	$\mathbf{1}e^{i\boldsymbol{p}}$	$\mathbf{1}e^{-i\boldsymbol{p}}$
2	$\gamma_i e^{i\boldsymbol{p}}\nabla_i$	$\gamma_i e^{-i\boldsymbol{p}}\nabla_i$
3	$\nabla_i e^{i\boldsymbol{p}}\nabla_i$	$\nabla_i e^{-i\boldsymbol{p}}\nabla_i$
4	$\nabla_i^4 e^{i\boldsymbol{p}}\nabla_i^4$	$\nabla_i^4 e^{-i\boldsymbol{p}}\nabla_i^4$
5	$\gamma_5 e^{i\boldsymbol{p}}$	$-\gamma_5 e^{-i\boldsymbol{p}}$

Table 4.2: Interpolator structure for the quark bilinears used for $I(J^{PC}) = 0(0^{++})$ in this study.

$I(J^{PC}) = 0(0^{++})$ **channel**

Using similar methodology as for the ρ resonance, we first build up an interpolator basis in A_1^+ irrep for the s-wave scattering channel. For the σ meson study, we constructed 4 different $q\bar{q}$ interpolators. They have the form

$$\sigma(\Gamma_i(\mathbf{p}), t) = \frac{1}{\sqrt{2}}[\bar{u}(t)\Gamma_i(\mathbf{p})u(t) + \bar{d}(t)\Gamma_i(\mathbf{p})d(t)]. \qquad (4.63)$$

The Γ matrices represent the $q\bar{q}$ interpolators structures listed in Table 4.2. The first four rows are used for the quark-antiquark interpolators and the last row is used for the pion-pion interpolators. The $\pi\pi$ operator with $I = 0$ and $I_3 = 0$ can be constructed as[1]

$$\pi\pi(\boldsymbol{p}_1, \boldsymbol{p}_2) = \frac{1}{\sqrt{3}}\{\pi^+(\boldsymbol{p}_1)\pi^-(\boldsymbol{p}_2) + \pi^-(\boldsymbol{p}_1)\pi^+(\boldsymbol{p}_2) + \pi^0(\boldsymbol{p}_1)\pi^0(\boldsymbol{p}_2)\}, \qquad (4.64)$$

---

[1]If we use the Clebsch-Gordan coefficients to compute the $I = 0$ combination of $I_1 + I_2 = 1 + 1$ isospins, the coefficient in front of $\pi^0\pi^0$ would be negative. However, this assumes that the pion fields are defined as in Table 3.1. Note that there is a sign discrepancy for π^- when compared to Eq. 4.52. The expression here is correct when the pion interpolators are defined as in Eq. 4.52.

where $\pi^+(\boldsymbol{p})$ and $\pi^-(\boldsymbol{p})$ are given in Eq. 4.52. To get the π^0 operator, we performed a momentum projection on $\mathcal{O}_{\pi^0}(n)$ in Eq. 3.13

$$
\begin{aligned}
\pi^0(\boldsymbol{p}, t) &= \frac{1}{\sqrt{2}} \sum_{\boldsymbol{x}} \{\bar{u}(,x,t)\Gamma_5 e^{i\boldsymbol{px}}u(\boldsymbol{x},t) - \bar{d}(\boldsymbol{x},t)\Gamma_5 e^{i\boldsymbol{px}}d(\boldsymbol{x},t)\} \\
&= \frac{1}{\sqrt{2}}\{\bar{u}(t)\Gamma_5(\boldsymbol{p})u(t) - \bar{d}(t)\Gamma_5(\boldsymbol{p})u(t)\} \, .
\end{aligned}
\tag{4.65}
$$

Since the σ meson is in the s-wave scattering channel, the lowest scattering momentum is $\boldsymbol{p} = (0,0,0)$ instead of $\boldsymbol{p} = (0,0,1)$ as in the ρ meson case. For some ensembles, we will use additional $\pi\pi$ operators to extract all the low-lying energy states up to a certain energy cutoff. The $\pi\pi$ operators in the rest frame $\boldsymbol{P}_0 = (0,0,0)$ in A_1^+ irreducible representation are as follows:

$$
\begin{aligned}
\pi\pi_{000}^{(0)} &= \pi\pi(\boldsymbol{p}_1 = (0,0,0), \boldsymbol{p}_2 = \boldsymbol{P}_0 - \boldsymbol{p}_1) \, , \\
\pi\pi_{001}^{(0)} &= \pi\pi(\boldsymbol{p}_1 = (0,0,1), \boldsymbol{p}_2 = \boldsymbol{P}_0 - \boldsymbol{p}_1) \, .
\end{aligned}
\tag{4.66}
$$

For the moving states with momentum $\boldsymbol{P}_1 = (0,0,1)$, we use the following interpolators

$$
\begin{aligned}
\pi\pi_{001}^{(1)} &= \pi\pi(\boldsymbol{p}_1 = (0,0,1), \boldsymbol{p}_2 = \boldsymbol{P}_i - \boldsymbol{p}_1) \, , \\
\pi\pi_{002}^{(1)} &= \pi\pi(\boldsymbol{p}_1 = (0,0,1), \boldsymbol{p}_2 = \boldsymbol{P}_i - \boldsymbol{p}_1) \, , \\
\pi\pi_{011}^{(1)} &= \frac{1}{2} \sum_{\boldsymbol{p}_1 \in \mathcal{P}} \pi\pi(\boldsymbol{p}_1, \boldsymbol{p}_2 = \boldsymbol{P}_1 - \boldsymbol{p}_1) \, ,
\end{aligned}
\tag{4.67}
$$

where $\mathcal{P} = \{(0,1,1), (1,0,1), (-1,0,1), (0,-1,1)\}$.

The correlation matrices we built for the σ-meson are similar to the ones used for the ρ meson. We included six interpolators into the variation basis to form a 6×6 correlation matrix. For example, for the zero-momentum states we used four $\bar{q}q$ operators listed in the Table 4.2, $\pi\pi_{000}$, and $\pi\pi_{001}$. The entries of the correlation

matrix are

$$C_{\sigma_i \leftarrow \sigma_j} = \left\langle \sigma_i(\boldsymbol{P}, t_f) \sigma_j^\dagger(\boldsymbol{P}, t_i) \right\rangle = \left\langle -[i\boldsymbol{P}f | j'\boldsymbol{P}i] + 2 \times [i\boldsymbol{P}f][j'\boldsymbol{P}i] \right\rangle,$$

$$C_{\sigma_i \leftarrow \pi\pi} = \left\langle \sigma_i(\boldsymbol{P}, t_f) \pi\pi(\boldsymbol{p}, \boldsymbol{P} - \boldsymbol{p}, t_i)^\dagger \right\rangle$$

$$= \sqrt{6} \times \left\langle [i\boldsymbol{P}f | 5'\boldsymbol{P} - \boldsymbol{p}i | 5'\boldsymbol{p}i] - [i\boldsymbol{P}f][5'\boldsymbol{p}i | 5'\boldsymbol{P} - \boldsymbol{p}i] \right\rangle,$$

$$C_{\pi\pi \leftarrow \pi\pi} = \left\langle \pi\pi(\boldsymbol{p}', \boldsymbol{P} - \boldsymbol{p}', t_f) \pi\pi(\boldsymbol{p}, \boldsymbol{P} - \boldsymbol{p}, t_i)^\dagger \right\rangle$$

$$= \left\langle 3 \times [5\boldsymbol{p}'f | 5\boldsymbol{P} - \boldsymbol{p}'f][5'\boldsymbol{p}i | 5'\boldsymbol{P} - \boldsymbol{p}i], \right.$$

$$+ 1 \times [5\boldsymbol{p}'f | 5'\boldsymbol{p}i][5\boldsymbol{P} - \boldsymbol{p}'f][5'\boldsymbol{P} - \boldsymbol{p}i],$$

$$(4.68)$$

$$+ 1 \times [5\boldsymbol{p}'f | 5'\boldsymbol{P} - \boldsymbol{p}i][5\boldsymbol{P} - \boldsymbol{p}'f | 5'\boldsymbol{p}i],$$

$$- 3 \times [5\boldsymbol{p}'f | 5\boldsymbol{P} - \boldsymbol{p}'f | 5'\boldsymbol{p}i | 5'\boldsymbol{P} - \boldsymbol{p}i],$$

$$- 3 \times [5\boldsymbol{p}'f | 5\boldsymbol{P} - \boldsymbol{p}'f | 5'\boldsymbol{P} - \boldsymbol{p}i | 5'\boldsymbol{p}i],$$

$$\left. + 1 \times [5\boldsymbol{p}'f | 5'\boldsymbol{P} - \boldsymbol{p}i | 5\boldsymbol{P} - \boldsymbol{p}'f | 5'\boldsymbol{p}i] \right\rangle.$$

The differences between the ρ and σ meson correlation functions are more apparent when we draw the quark diagrams corresponding to the terms above:

$$C_{\sigma \leftarrow \sigma} = \left\langle - \bigcirc\!\!\!\!\diagup + 2\, \substack{\bigcirc\\\bigcirc} \right\rangle, \qquad C_{\sigma \leftarrow \pi\pi} = \left\langle \sqrt{6}\, \triangle - \sqrt{6}\, \substack{\bigcirc\\\bigcirc} \right\rangle,$$

$$C_{\pi\pi \leftarrow \pi\pi} = \left\langle 3\, \substack{\bigcirc\\\bigcirc} + \bigcirc\!\!\!\diagup\, \bigcirc\!\!\!\diagup + \bigotimes - 3\, \bowtie - 3\, \square + \bowtie\!\!\!\!\diagup \right\rangle.$$

$$(4.69)$$

Compared to the ρ resonance, in the $I = 0$ channel, each entry of the correlation matrix contains temporally disconnected diagrams. Evaluation of these diagram is difficult. The reason is that this channel has the same quantum numbers as the vacuum and the correlators do not vanish as the time separation is taken to infinity. The constant contribution has to be subtracted in order to get the expected exponential behavior. In our study, we implemented two approaches to subtract the vacuum contribution

81

from the temporal disconnected diagrams. The first method is that we estimate the vacuum contribution by taking the average of the vacuum bubble and subtract these value from the original correlation function as

$$\left\langle \mathcal{O}(t_2)\mathcal{O}^\dagger(t_1)\right\rangle_{\mathrm{sub}} = \left\langle \mathcal{O}(t_2)\mathcal{O}^\dagger(t_1)\right\rangle - \left\langle \mathcal{O}(t_2)\right\rangle\left\langle \mathcal{O}^\dagger(t_1)\right\rangle . \tag{4.70}$$

The second approach to solve this problem is to consider the so called *shifted correlator* instead of the original correlators in the correlation matrix

$$C_{ij}(t) = C_{ij}(t+d) - C_{ij}(t) , \tag{4.71}$$

where d is the time shift between two correlation functions. In this case, since the vacuum contribution is a constant in the correlator, it is subtracted implicitly when taking the difference of correlation functions. We will discuss the numerical results for both methods in next section.

5 Numerical results

In this chapter, we present our results for the resonance parameters for both ρ and σ mesons calculated using the methods we discussed in previous chapters. We first present in Section 5.1 the ensemble used in our simulations and discuss the way we determined the parameters, i.e., the lattice spacing a, pion mass m_π and pion decay constant for each ensemble. In Section 5.2 we focus on our calculation of the ρ-resonance: we discuss the sensitivity of our results on the choice of variational basis, we compare different fitting models for computing the resonance parameters, and we consider the effects due to the absence of the $K\bar{K}$ on the ρ meson. In Section 5.3 we discuss our results for the σ meson, following the same analysis steps.

5.1 Simulation parameters

In this section we discuss the parameters for the ensembles used in our calculations. We have generated configurations using Lüscher-Weiss gauge action [39, 40] and nHYP-smeared clover fermions [48] with two mass-degenerate quark flavors ($N_f = 2$). For each mass we generated three sets of ensembles with different elongations. The elongations were chosen to ensure that the energy spectrum for the zero-momentum states in the A_2^- channel overlaps well with the ρ-resonance region, following the procedure described in a previous study [11].

The parameters for these ensembles are listed in Table 5.1. The lattice spacing a for each ensemble is listed as well as the number of gauge configurations N_{cfg} and the number of eigenvectors used for LapH smearing. am_π, am_K, am_N represent the pion, kaon, and nucleon mass, and af_π, af_K are the pion and kaon decay constants, all quantities expressed in lattice units. Hadron masses were calculated by fitting standard hadron correlation functions. The quark masses were defined using the partially conserved axial current (PCAC) relation. The decay constants were computed using the two-point correlation functions of the pseudoscalar and axial-vector densities (see

ensemble	$N_t \times N_{x,y}^2 \times N_z$	η	$a[\mathrm{fm}]$	N_{cfg}	N_v	am_π
$\mathcal{E}_1$	$48 \times 24^2 \times 24$	1.0	0.1210(2)(24)	300	100	0.1934(5)
$\mathcal{E}_2$	$48 \times 24^2 \times 30$	1.25	–	–	–	–
$\mathcal{E}_3$	$48 \times 24^2 \times 48$	2.0	–	–	–	–
$\mathcal{E}_4$	$64 \times 24^2 \times 24$	1.0	0.1215(3)(24)	400	100	0.1390(5)
$\mathcal{E}_5$	$64 \times 24^2 \times 28$	1.17	–	–	–	–
$\mathcal{E}_6$	$64 \times 24^2 \times 32$	1.33	–	–	–	–

ensemble	am_K	am_N	$am_{u/d}^{pcac}$	af_π	am_s^{pcac}	af_K
$\mathcal{E}_1$	0.3235(6)	0.644(6)	0.01237(9)	0.0648(8)	0.03566(6)	0.1015(2)
$\mathcal{E}_2$	–	–	–	–	–	–
$\mathcal{E}_3$	–	–	–	–	–	–
$\mathcal{E}_4$	0.3124(8)	0.62(1)	0.00617(9)	0.060(1)	0.03358(6)	0.0980(2)
$\mathcal{E}_5$	–	–	–	–	–	–
$\mathcal{E}_6$	–	–	–	–	–	–

Table 5.1: The parameters for the ensembles used in this study.

for example [69]). To fix the strange quark mass in the valence sector, we use the strategy proposed by Fritzsch et al [70]: we fix the ratio m_K/f_K to its physical value, which has the effect of making the kaon mass close to its physical value.

The lattice spacing was determined using an observable based on the Wilson flow [71]: the w_0 parameter [72]. This quantity can be determined with very little stochastic error from a handful of configurations. We used 150 configurations from ensembles $\mathcal{E}_1$ and $\mathcal{E}_4$ and computed $w_0/a = 1.3888(24)$ and $w_0/a = 1.4157(37)$ respectively. These measurements were used to fix the lattice spacing using the conversion factors determined in [73]: we computed the dimensionless quantity $y = m_\pi^2 t_0$, determined $w_0(y)/w_0(y = 0)$ from Fig. 4 in the above reference, and then converted to physical units using $w_0(y = 0) = 0.1776(13)\,\mathrm{fm}$. This value of w_0 was determined from a set of $N_f = 2$ simulations where f_K was used to set the scale [70].

The scale determined this way differs from the scale we used in our previous study [11] by 3.5%, but we attribute this shift to the fact that the value of the Sommer

parameter [74] is difficult to define unambiguously on configurations with light quarks. The value we used in our previous study was $r_0 = 0.5\,\text{fm}$, but recent determinations of r_0 from global fits of the hadronic spectrum favor smaller values [75, 76] and produce values in agreement with the scale determined based on w_0. We decided to adopt the scale determined by w_0 because the method is very straightforward and it has small stochastic errors. Note that at fixed lattice spacing in the presence of lattice artifacts, the lattice spacing determination introduces a systematic error. We estimate that our systematic error associated with the lattice spacing is at the level of 2%. To confirm the correctness of the lattice spacing, we looked at the nucleon mass, pion and kaon decays constants. We computed the nucleon mass m_N and extrapolated to the physical point using an empirically motivated fit form [77]. The extrapolated values agree at the level of 2%, but this may be fortuitous since the error bars of the extrapolation were at the level of 4%. In any case, this error level is in line with the expectation from other studies that used HEX-smeared fermions at similar lattice spacing [78], where the hadronic spectrum was found to be shifted by about 2% relative to the continuum. The values of f_π and f_K were determined using the procedure outlined in [70]. For the masses used in our study, our values for f_K differ by less than 1% from the values determined there at much smaller lattice spacing.

5.2 ρ resonance parameters

Energy spectrum in A_2^- irrep

In this study, we only consider the two-particle scattering. Therefore, for each ensemble we extract the lowest three or four levels in the A_2^- channel, since these levels correspond roughly to the elastic region where the center-of-mass energy is below $4m_\pi$. To extract the energies, we compute the correlation matrix $C(t)$, solve the eigenvalue problem in Eq. 3.33, and fit the extracted eigenvalues to an exponential ansatz. In Fig. 5.1 we show the effective mass computed from the three lowest eigenvalues on the $\mathcal{E}_1$
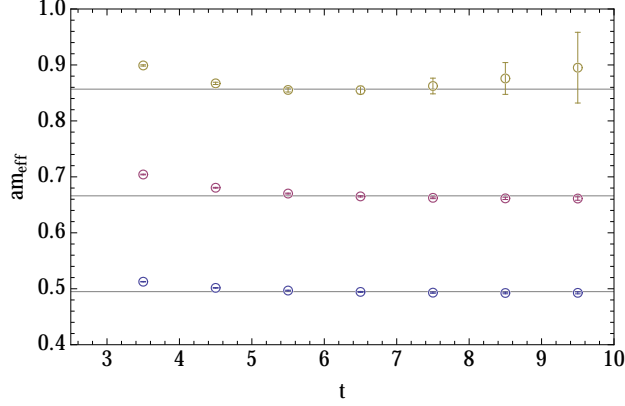
Figure 5.1: The effective mass for the lowest three energy levels of $\mathcal{E}_1$ ensemble.

ensemble. Contamination from higher energy levels is present in the early time slices, therefore we used a double exponential to extract the energy. The horizontal lines indicate the results of the fit. Note that the effective mass does not flatten out until later times. To extract the energy, we fit a double exponential function constrained to pass through 1 at $t = t_0$: $f_1(t) = Ae^{-E(t-t_0)} + (1 - A)e^{-E'(t-t_0)}$.

For the lowest $\boldsymbol{P} = 0$ state on ensemble $\mathcal{E}_3$ this fit form does not work, due to wrap-around effects in the time direction [67, 79]. We added a constant term to the fit form to accommodate this effect: $f_2(t) = Ae^{-E(t-t_0)} + (1 - A - C)e^{-E'(t-t_0)} + C$. We used this fit form with the other zero-momentum states in all the ensembles, but the constant term produced by minimizing χ^2 was compatible with zero. For the moving states, the wrap-around effect leads to a small, slowly decaying term with a rate controlled by the mass difference between the moving pion and the pion at rest $\delta E = \sqrt{m_\pi^2 + (2\pi/L)^2} - m_\pi$ [67]. For the states where this contribution was significant, we used the following fit form $f_3(t) = Ae^{-E(t-t_0)} + (1 - A - C)e^{-E'(t-t_0)} + Ce^{-\delta E(t-t_0)}$. The fitting details including the choice of t_0, fitting range, fit form, energy extracted, and quality of the fit are tabulated in Table C.1 in the Appendix.

We discuss now the choice of the interpolator fields and in particular we address the question whether our interpolating field basis overlaps well with the lowest three
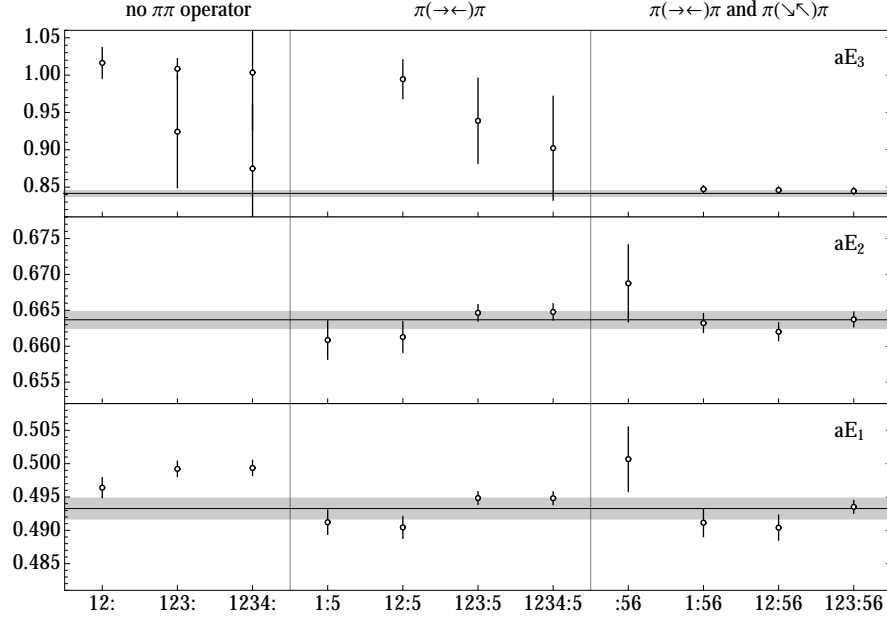
Figure 5.2: Energy spectrum for ensemble $\mathcal{E}_1$ with different interpolator basis combinations. The horizontal axis labels represent the operators listed in Tab. 4.1.

energy states in the A_2^- channel. To this end, we compare the energy spectrum extracted using different subsets of the interpolating fields basis. To simplify the discussion, we focus first on the $\mathcal{E}_1$ ensemble. The energy spectra extracted from different interpolating fields basis combinations are plotted in Fig. 5.2. The horizontal labels $\mathcal{O}_{1-4}$ are the $q\bar{q}$ interpolating fields, $\mathcal{O}_5$ is $\pi\pi_{100}$ and $\mathcal{O}_6$ is $\pi\pi_{011}$. The vertical axis represents the energy for the three lowest levels. Note that we use different scales for each level. The three horizontal bands show the energy values extracted from the 6×6 correlation matrix. In the first panel, we include only $q\bar{q}$ operators. While the ground state seems to be well approximated, the $q\bar{q}$ operators have little overlap with the first and second excited states which indicates that they are multi-hadron states. In the second column, we use the $\pi\pi_{100}$ operator together with various combinations of $q\bar{q}$ operators. The ground state and first excited state are well reproduced, even when using only one $q\bar{q}$ interpolator. However, the second excited state has large error bars even if we add three other $q\bar{q}$ operators, which indicates that it has a large
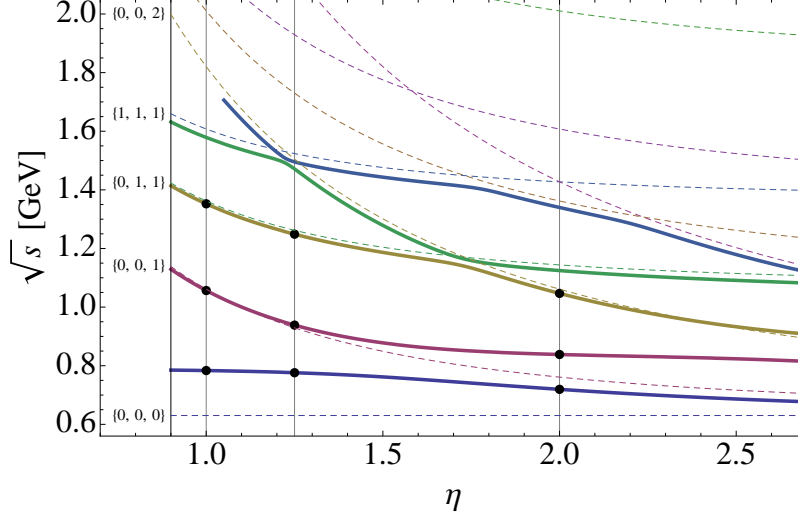
Figure 5.3: Energy spectrum with different elongation factor η from unitary chiral perturbation theory in the rest frame $\mathbf{P} = (0,0,0)$ (solid lines). The dashed lines indicate the non-interacting π-π energies.

multi-hadron component. In the third panel, we use two multi-hadron interpolators: $\pi\pi_{100}$ and $\pi\pi_{011}$. Once one $q\bar{q}$ operator is added to the basis, all three lowest energy states are well determined with small error bars. Adding more $q\bar{q}$ operators to the basis does not improve the extraction and we conclude that these lowest three states are well captured by our set of interpolators.

To confirm the conclusion above, we fit a model based on UχPT model (see Section 4.3 and Appendix B) to the energy levels extracted from ensemble $\mathcal{E}_1$ and use it to predict the energy levels for different box elongations. The expected energy levels are plotted in Fig. 5.3 as a function of the elongation. In this figure, η labels the elongation factor, in particular $\eta = 1.0, 1.25, 2.0$ are the ensembles we used for $m_\pi \approx 315\,\mathrm{MeV}$. Here, the $\eta = 1$ values are fitted and then eigenvalues for $\eta = 1.25$ and $\eta = 2$ are predicted. In the graph we also indicate the expected energy levels for two-pion states with different momentum in the absence of interactions. We see that for elongation $\eta = 1$ which corresponds to ensemble $\mathcal{E}_1$ the ground state is not in the vicinity of any two-pion state and thus it is mainly a $q\bar{q}$ state, whereas the first two excited states are close to non-interacting two-pion states, which indicates that

they have large two-hadron components. That is the reason why the multi-hadron operators $\pi\pi_{001}$ and $\pi\pi_{011}$ are required to extract these states reliably. For $\mathcal{E}_1$ and $\mathcal{E}_2$ these multi-hadron operators are sufficient. However, for $\eta = 2.0$, the second excited state is no longer near the non-interacting pions moving with back-to-back momentum $\boldsymbol{p} = (0, 1, 1)$, because the state with back-to-back momentum $\boldsymbol{p} = (0, 0, 2)$ has lower energy for this elongation. Note that this level crossing is kinematical in nature rather than due to a resonance. This is a peculiar feature of our geometry due to the fact that the ordering of levels with different transverse momenta changes when going from small elongations to large ones. Thus, in order to extract the second excited state reliably on $\mathcal{E}_3$ and $\mathcal{E}_6$ we need to add the $\pi\pi_{002}$ interpolating field to our basis. For these ensembles we use a 7×7 correlation matrix and extract four energy levels since the third excited state is very close the the second excited state and below the $4m_\pi$ threshold. As a result, we will have more data points to fit for the phase-shift pattern in the next section. The number of energy levels we extracted for each ensemble is listed in Table C.1 in Appendix C.1.

ρ resonance parameters[2]

We extract the resonance parameters by fitting the phase-shift data, or equivalently the energy levels, using two fitting forms: a simple Breit-Wigner form and the UχPT model discussed in Section 4.3. Note that when fitting the phase-shift data, the correlation between E_{cm} and $\delta(E_{\text{cm}})$ has to be taken into account. The Breit-Wigner form is used in most lattice studies of the ρ-resonance since it fits the phase shift well. This also offers a straightforward way to compare our results with the ones from other studies. The UχPT model provides an alternative parametrization which also captures well the phase-shift behavior in the ρ-resonance region. Its main advantage, and the reason we use it in our study, is that it can be used to fit the data sets at

---

[2]This section is originally from [80]. All the authors are agree the usage of the content from [80] in this thesis.
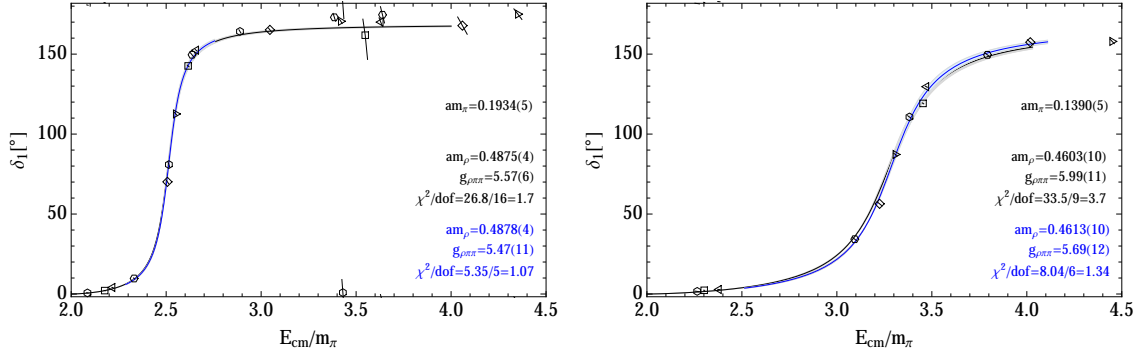
Figure 5.4: Phase shifts as a function of the center-of-mass energy.

different quark masses simultaneously, and it offers a reasonable way to extrapolate our results to the physical point.

The Breit-Wigner parametrization is described in Eq. 4.41. In Fig. 5.4 we show our phase shifts and the fitted curves. Here, the error bars are slanted along the direction of the Lüscher curves. On the left we have the $m_\pi = 315\,\text{MeV}$ data and on the right the $m_\pi = 226\,\text{MeV}$ data. The triangles, squares, and hexagons correspond to data extracted from $\mathcal{E}_1$, $\mathcal{E}_2$, $\mathcal{E}_3$ (left) and $\mathcal{E}_4$, $\mathcal{E}_5$, $\mathcal{E}_6$ (right) respectively. The black curves, error bands, and fit parameters correspond to Breit-Wigner fits to all data points in the elastic region, $E_{\text{cm}} < 4m_\pi$. Blue color indicates the fit to the data in $m_\rho \pm 2\Gamma_\rho$ region. Note that if we try to fit the entire elastic region, $E_{\text{cm}} < 4m_\pi$, the quality of the fit, as indicated by χ^2 per degree of freedom, is not very good. While the curve passes close to our points, our energy level determination is very precise and the Breit-Wigner form is not describing the entire energy range accurately. This is not a serious problem since the Breit-Wigner form is only expected to describe the data well near the resonance. Ideally, we would restrict the fit only to a narrow region around the resonance, but the number of data points included in our fit is also reduced and the fit is poorly constrained. As a compromise, we decided to fit the data points that fall in the range $E_{\text{cm}} \in [m_\rho - 2\Gamma_\rho, m_\rho + 2\Gamma_\rho]$. The fit quality is improved and the UχPT fits are very close to the blue Breit-Wigner curves. Therefore, we will use

m_π [MeV]	am_ρ	$g_{\rho\pi\pi}$	m_ρ[MeV]	Γ_ρ[MeV]	Γ'_ρ[MeV]
315	0.4878(4)	5.47(11)	795.5(0.7)(16)	35.7(1.4)(0.7)	124.4(5)(2.5)
226	0.4613(10)	5.69(12)	749.2(1.6)(15)	81.7(3.3)(1.6)	134.4(5)(2.7)

Table 5.2: Breit-Wigner form fits in the $m_\rho \pm 2\Gamma_\rho$ region.

the results of the narrower fits in the following discussion. The results for two pion masses are included in Table 5.2 where Γ_ρ is the width at the current pion mass and Γ'_ρ is the width extrapolated to the physical point. The widths are evaluated using Eq. 4.41 with $\Gamma_\rho = \Gamma_{BW}(m_\rho, m_\pi)$ and $\Gamma'_\rho = \Gamma_{BW}(m_\rho^{\text{phys}}, m_\pi^{\text{phys}})$. The first error is the stochastic error and the second one is the systematic error due to the lattice spacing determination.

We note that the Breit-Wigner fit parameters depend mildly on the range of the fit. The mass of the resonance is very well determined, with stochastic errors of the order of few parts per thousand, and it is insensitive to the fit range. This is because the place where the phase shift passes through $\pi/2$ is well constrained by the lattice data. The coupling $g_{\rho\pi\pi}$ is only constrained at the level of 2% and it is more sensitive to the fit range, showing a clear drift towards lower values as we narrow the fitting range.

If we are interested in capturing the phase-shift behavior in the entire energy range available, we could use slight variations of the Breit-Wigner parametrization. Indeed we found that the quality of the fit in the full elastic region is improved when adding barrier terms [81], especially on the larger pion mass ensemble. However, such fitting forms change the way the resonance mass and width are defined, making it harder to compare our results directly with other determinations, and we will not discuss these results here. We include all the relevant data for the extracted energies and their correlation matrix in Appendix C.1.

For the Breit-Wigner fit, we found that the quality of the fit changes significantly as we vary the pion mass within its error bounds. If the Breit-Wigner fit was known to

m_π [MeV]	$\hat{l}_1 \times 10^3$	$\hat{l}_2 \times 10^3$	m_ρ[MeV]	Γ_ρ[MeV]	χ^2/dof
315	1.5(5)	-3.7(2)	796(1)	35(1)	1
138			704(5)	110(3)	
226	2(1)	-3.5(2)	748(1)	77(1)	1.53
138			719(4)	120(3)	
combined 138	2.26(14)	-3.44(3)	720(1)	120.8(8)	1.26

Table 5.3: UχPT fits in the $m_\rho \pm 2\Gamma_\rho$ region and extrapolations to the physical point.

be the exact description of the phase shift in the elastic region, we could in principle use the pion mass as a fitting parameter in this fit to further constrain its value. Since this is not the case, we did not attempt to do this here.

We turn now to the discussion of the fit using the UχPT model. An important feature is that this model can be used to fit the lattice results for both quark masses *simultaneously*. In practice, one does not fit the phase shifts with the UχPT model but rather one fits directly the energy eigenvalues taking into account their correlations. With the fitted parameters, we can then extrapolate the physical observables such as the phase shift and the physical quantity such as the ρ mass m_ρ and decay width Γ_ρ to the physical point and also to assess the corrections due to the missing strange quark mass in our calculation. When considering only the π-π channel, the model requires as input the pion mass, the pion decay constant and two low-energy constants, $\hat{l}_{1,2}$. The pion mass and decay constants used are the ones in Table 5.1. Note that the model can take directly dimensionless input–am_π, af_π and the energies aE—so the systematic errors associated with the lattice spacings play no role in the extraction of dimensionless parameters $\hat{l}_{1,2}$. The error bars that appear in the tables below reflect just the stochastic error.

In Table 5.3 we show the results of fitting the UχPT model. In this table, the errors quoted are statistical. The upper two entries show the cases of heavy and light pion mass, both individually extrapolated to the physical point. The third entry shows the combined fit of both masses and its extrapolation. The UχPT model is similar to

the Breit-Wigner parametrization in the sense that it captures the broad features of the phase shift in the elastic region but the quality of the fit is not good when trying to fit the entire energy range. We restrict the fit range to $m_\rho \pm 2\Gamma_\rho$, as we did for the Breit-Wigner parametrization. In this range the quality of the fit is reasonable. The resonance mass is determined from the center-of-mass energy that corresponds to a $90°$ phase shift. The width corresponds to the imaginary value of the resonance pole in the complex plane. While these parameter definitions are not the same as the ones determined from the Breit-Wigner fit, the results are consistent, as can be seen from the table.

Fitting each quark mass separately produces consistent values for $\hat{l}_{1,2}$ which indicates that the dependence on the quark mass is well captured by this model. Since the model is consistent for both quark masses we can do a combined fit which allows us to pin down $\hat{l}_{1,2}$ with even better precision. As can be seen from the table, the combined fit quality is similar to the individual ones. We will use these parameters in the subsequent discussion.

Moreover, we can try to estimate the effects due to the absence of the strange quark using the UχPT model by turning on the coupling to the K$\bar{\text{K}}$ channel. We fix the $\pi\pi \to K\bar{K}$ and $K\bar{K} \to K\bar{K}$ transitions from a fit to the physical data, while keeping $\hat{l}_{1,2}$ for the $\pi\pi$ transition at the values we got from fitting our data. The pion decay constant is adjusted to match the values in Table 5.1. We report these estimates in Table 5.4. The first set of errors quoted are statistical; for $\hat{m}_\rho$ and $\hat{\Gamma}_\rho$ we also quote a set of systematic errors associated with model dependence. More details about the UχPT fit are included in Appendix B.

In Fig. 5.5 we plot our results for the resonance mass together with the UχPT extrapolation, in comparison with results from other lattice groups. The red curve corresponds to an extrapolation based on the UχPT model. The light-red curve corresponds to a simple $m_\rho = (m_\rho)_0 + \text{const} \times m_\pi^2$ fit [82]. The blue band corresponds

m_π [MeV]	m_ρ [MeV]	Γ_ρ [MeV]	$\hat{m}_\rho$ [MeV]	$\hat{\Gamma}_\rho$ [MeV]
315	795.2(7)	36.5(2)	846(0.3)(10)	54(0.1)(3)
226	747.6(6)	77.5(5)	793(0.4)(10)	99(0.3)(3)
138	720(1)	120.8(8)	766(0.7)(11)	150(0.4)(5)

Table 5.4: UχPT results for $N_f = 2$, m_ρ and Γ_ρ; $N_f = 2 + 1$ estimates, $\hat{m}_\rho$ and $\hat{\Gamma}_\rho$.
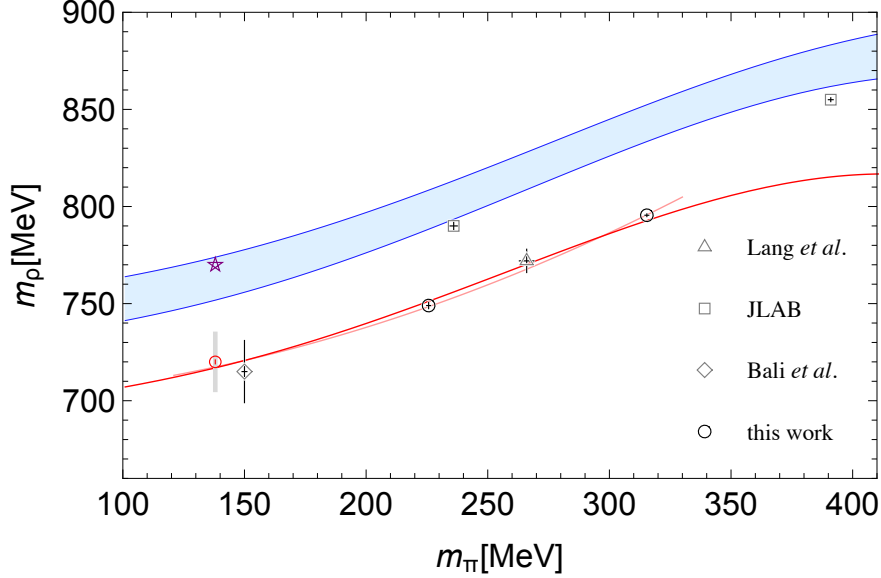
Figure 5.5: Resonance mass extrapolation to the physical point.

to an $N_f = 2 + 1$ estimate based on the UχPT model (see text). The other lattice data points are taken from Lang *et al* [10], JLab group studies [14, 16], and Bali *et al* [12]. The star corresponds to the physical result. The error bars shown with solid lines are stochastic. For the extrapolation the gray, thick error bar indicates the systematic error associated with the lattice spacing determination. It is clear that the extrapolation to the physical point in SU(2) is significantly below the experimental value, missing it by about 50 MeV which is about 8% of the resonance mass. The stochastic error for the extrapolated result is tiny compared with the shift. The systematic error due to the lattice spacing determination is larger, but even this cannot account for the discrepancy. The other possible sources of systematic errors are finite lattice spacing contributions, exponentially suppressed finite volume corrections,

quark mass extrapolation error, and systematics associated with the missing $K\bar{K}$ channel. The lattice artifacts errors are included in our estimate for the systematic error associated with the lattice spacing determination. To gauge the effect of the lattice volume corrections, we compare our results with the ones from a study by Lang *et al* [10]. This study was carried out on boxes of volume $(2\,\text{fm})^3$, whereas our study used boxes of about $(3\,\text{fm})^3$. We see in Fig. 5.5 that the results agree and we conclude that the finite volume corrections cannot account for the discrepancy either. The errors associated with the quark mass extrapolation are also expected to be small: in Fig. 5.5 we show the results of the extrapolation using a simple polynomial extrapolation which at leading order depends on m_π^2 [82][3]. The extrapolation agrees well with the prediction of UχPT in SU(2). Moreover, a recent calculation by Bali *et al* [12] close to the physical quark mass is also consistent with our extrapolation.

The likely reason for the discrepancy between the extrapolation and the physical result is the fact that the strange quark flavor is not included in our calculation. We note first that the results for UχPT in SU(2) agree very well with the results of the other $N_f = 2$ studies by Lang and Bali. The results when the strange quark is included are also shown in Fig. 5.5 (blue band indicating estimated model uncertainties as discussed in Appendix B). Note that the estimated shift is surprisingly large and it reduces the discrepancy substantially. The estimated resonance mass curve agrees quite well with a $N_f = 2+1$ lattice calculation recently reported by the Jlab group [16] that includes the $K\bar{K}$ channel. While these estimates are likely affected by systematic errors, we feel that they are accurate enough to indicate that the discrepancy is mostly generated by the absence of the strange quark in our calculation. We note that the magnitude of the shift in the resonance mass due to the inclusion of the $K\bar{K}$ channel is surprisingly large. The present work stresses the importance of taking into account $\pi\pi - K\bar{K}$ loops. A more detailed discussion of this point in the context of the UχPT

---

[3]There is lattice QCD evidence that the mass of ρ is well described by a linear dependence on m_π^2 near the physical quark mass below $370\,\text{MeV}$ [83].
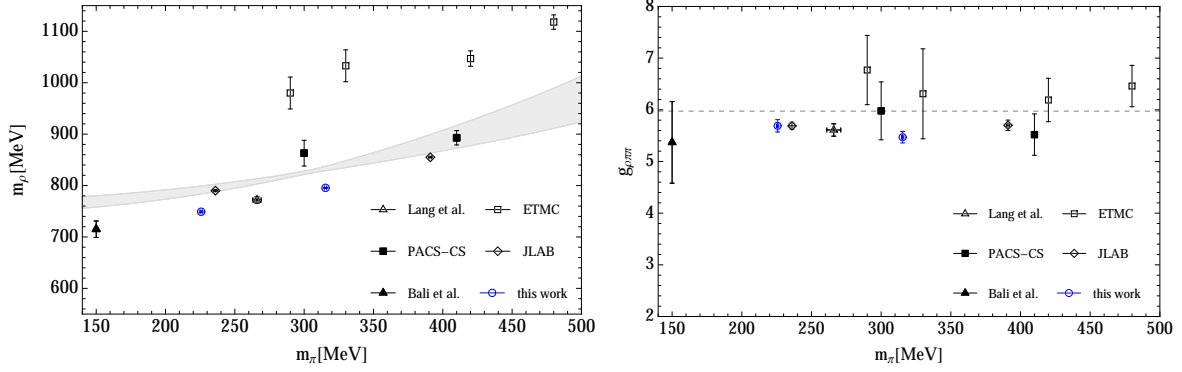
Figure 5.6: Comparison of different lattice calculations for the ρ resonance mass (left) and width parameter $g_{\rho\pi\pi}$ (right). The errors included here are only stochastic.

model is presented in Ref. [84].

Conclusions

We presented a high-precision calculation of the phase shift in the $I = 1$, $J = 1$ channel for $\pi\pi$ scattering. To scan the resonance region, we elongated the lattice in only one direction, which makes the generation of configurations less expensive.

The phase shifts are broadly described by a Breit-Wigner parametrization, as expected. However, our calculation is precise enough to show that more sophisticated models are required to describe the variation of the phase shift in the entire elastic region. It is hoped that our results can be used to validate these models and to constrain their parameters.

The resonance mass and $g_{\rho\pi\pi}$ coupling are extracted from fitting a Breit-Wigner parametrization in the energy region $m_\rho \pm 2\Gamma_\rho$. In Fig. 5.6 we compare our results with other lattice determinations. The results labeled ETMC are taken from [9] and PACS from [7]. The band in the left plot indicates a $N_f = 2 + 1$ expectation from a UχPT model constrained by some older lattice QCD data and some other physical input [85]. The dotted line in the right plot indicates the $g_{\rho\pi\pi}$ that corresponds to the physical ρ width [86]. Other than the ETMC study, the lattice data seems to

be split in two groups: $N_f = 2 + 1$ results (PACS [7] and Jlab [14, 16]) which are in agreement with $N_f = 2 + 1$ expectations from UχPT [85], and $N_f = 2$ lattice data (Lang *et al* [10], Bali *et al* [12], and this work) that agrees with a $N_f = 2$ UχPT model fit to our data.

For the resonance mass, we performed an extrapolation to the physical mass using a UχPT model, which we found can describe well the phase-shift data at both quark masses using the same parameters. The extrapolation results are consistent with extrapolations based on other models [82] and other $N_f = 2$ lattice calculations, as discussed before. The extrapolated results differ significantly from the physical one and we argue that this is due to the absence of the strange quark in our calculation.

For the quark masses used in this study, we did not find evidence of significant finite volume effects. However, as we lower the pion mass, larger volumes would most likely be required. The original LapH method might turn out to be too expensive to apply directly, but a stochastic variant was already developed and shown to work well [17]. Note that we did not include the data points from [17] in Fig. 5.6 because this study is using the same ensemble as the Jlab group study [16] and their results are compatible with the ones computed by the Jlab group, albeit with slightly larger error bars.

Turning to the future, as far as phase shifts in the ρ resonance channel are concerned, we seem to have moved beyond proof-of-principle calculations and toward precision determinations. We anticipate that in the near future precise calculations at the physical point might be possible that will give us access directly to phase shifts to be compared to values extracted from physical data. For example, it would be interesting to see whether phase shifts close to threshold match chiral perturbation theory expectations, which at leading order are controlled solely by m_π and f_π.
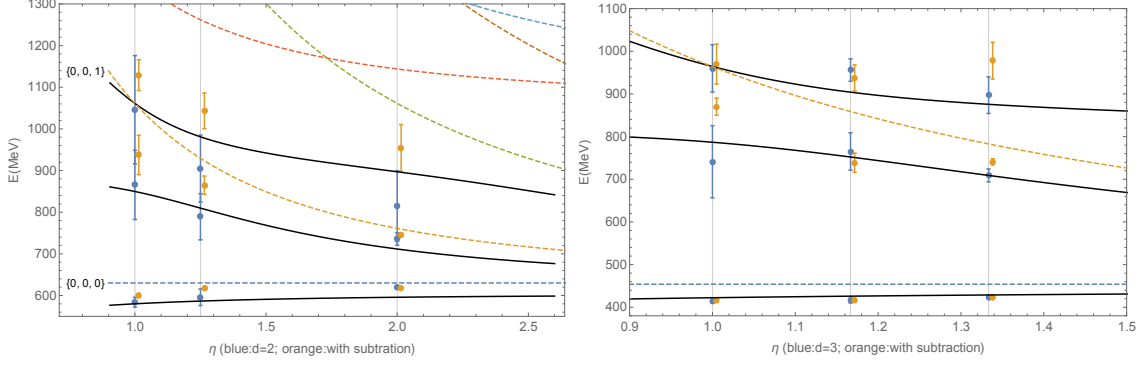
Figure 5.7: σ energy spectrum comparison with direct subtraction (orange) and shift correlator (blue) methods at two pion mass ensembles $m_\pi \approx 315\,\text{MeV}$ (left) and $m_\pi \approx 226\,\text{MeV}$ (right). Orange points are displaced slightly in the horizontal direction, for clarity. The curves are the prediction of the UχPT model with the parameters set from the fit to the ρ data.

5.3 σ resonance parameters

Energy spectrum in the A_1^+ irrep

Using the interpolator basis discussed in Section 4.4, we extract the energies of the lowest three or four energy levels in the A_1^+ channel in the elastic region. The only novel aspect in calculating the correlation matrix is that we need to subtract the vacuum contribution for the temporal disconnected diagrams. The results seem to be very sensitive to the method used to do the constant subtraction. To compare the two methods, we show the results extracted using the two methods in Fig. 5.7. In the figure, blue points are extracted using the shifted correlator method and orange points are extracted using the direct subtraction method. We note that the results from direct subtraction have smaller error bars, but they seem to be inconsistent with expectation: the ground-state energies indicate a much weaker interaction than the one extracted in other lattice studies of this channel [3], and the UχPT predictions when using the parameters for this model extracted from the ρ study. It turns out that energy levels extracted using this method are very sensitive to the value of the constant used to subtract the correlator, the vacuum expectation value of the

one-point functions generated by the interpolators. One possibility is that the values we computed are biased by wrap-around effects in the time direction. The shifted correlator method does not suffer from this problem, but it generates results with larger error bars. The reason for this is that, for the same fitting window as in the direct subtraction method, the correlators involved are noisier since the shifted values of the correlators correspond to later times. We decided to use the shifted correlator method for the zero-momentum states. For the moving states, we do not need any subtraction, since the one-point functions vanish in this case. Note that the results extracted from the moving states are consistent with the results extracted from the zero-momentum states, giving further support to our use of shifted correlators.

We also looked at the stability of our results with respect to varying the interpolator basis. Our conclusions were similar to the ones derived in our ρ study. The only noticeable difference is that for the moving states, we found that the energy levels are more sensitive to the presence of the $\mathcal{O}_2 = \gamma_i \nabla_i$ interpolator in our basis. We believe this is because the other $\bar{q}q$ operators have the same γ-matrix structure, all $\gamma = 1$, and thus O_2 provides a significantly different overlap with the relevant states.

The energy levels extracted for this channel both for zero-momentum and moving states and the details of the fitting parameters are listed in Appendix C.3.

σ resonance parameters

Using the energy levels extracted in the A_1^+ channel, we compute the phase shifts using the relevant Lüscher's formula in Eq. 4.30 where we assume that the contribution from $J > 0$ is negligible. In Fig. 5.8 we plot the results for the two quark masses. Note that the data are significantly noisier than for the ρ-channel. However, the quality is good enough to constrain the parameterizations and extract the pole mass for the σ meson. One surprising feature is that the data for the lower quark mass has smaller error bars, likely a consequence of the dynamics in this channel since the statistics are
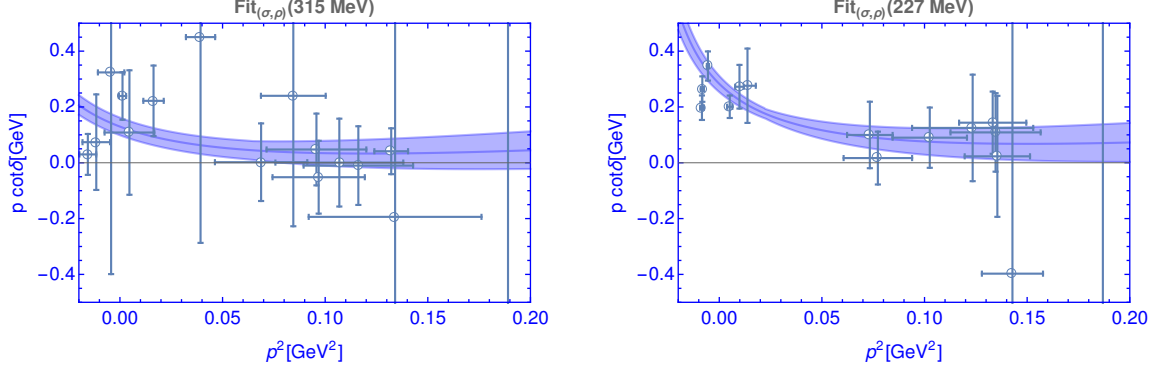
Figure 5.8: $p \cot \delta_0$ as a function of scattering momentum in the center-of-mass frame for the σ meson. The curve is the UχPT model with the parameters fixed to the combined σ and ρ channel fit (the highest-energy data point in $m_\pi = 315\,\mathrm{MeV}$ and the two highest-energy data points in $m_\pi = 227\,\mathrm{MeV}$ are excluded from the fit).

comparable.

To parameterize the σ meson resonance, we use both a conformal parameterization and a UχPT model. The reason we use different models is to find out how much the resonance parameters change with the model and to estimate the systematic error associated with the choice of parameterization. The conformal model parameterizes the resonance at given pion masses which, in our case, are $m_\pi = 315\,\mathrm{MeV}$ and $227\,\mathrm{MeV}$ without the possibility of chiral extrapolation. We report the fitting details including the free parameters B_0, B_1, B_2 from Eq. 4.43 of the conformal model in Table 5.5, where n is the number of data points we used to the model. As we can see from the value of the χ^2/ν, the conformal parametrization provides a good description of the data.

The resonance parameters can be calculated based on these three free parameters

$m_\pi[\mathrm{MeV}]$	B_0	B_1	n	χ^2/ν
227	11(1)	9(3)	14	0.7
315	6(1)	-1.6(3)	15	0.7

Table 5.5: Conformal model parameters fitted from different pion masses.

Fit	m_π	L_a	L_b	L_c	n	χ^2/ν
σ	227&315	-0.10 ± 0.16	0.07 ± 0.14	-0.010 ± 0.012	29	1.1

Table 5.6: UχPT model parameters fitted from data points at different pion masses.

with estimated parameters values shown in Table 5.8. We extract the position of the pole and list it in columns labelled Re $\sqrt{s_0}$ and Im $\sqrt{s_0}$, and the residue at the pole in columns labelled $|g|$, which is a measure of the strength between σ and $\pi\pi$. As we can see, while the conformal parametrization fits the lattice data well, the pole mass extracted from this model has very large stochastic errors.

For the UχPT model, we performed a combined fit to all energy levels including all the data for the two pion masses as we did for the ρ resonance. The results of the fit are listed in Table 5.6. The pole position and the residue at the pole are listed in Table 5.8. We see that the results are compatible with the fits based on the conformal parametrization, but with tighter error bars since now the fit includes the data for both quark masses.

To further constrain the parameters for the UχPT model, we perform a combined fit to the energy levels for both σ and ρ channels and for both quark masses. The energy levels fitted for the ρ channel are the same ones used in the fits discussed in Section 5.2. For the fit we perform a fully-correlated analysis, where the cross-correlations between the σ and ρ channels are included. The fitted values for these parameters are listed in Table 5.7. We see that we can accommodate both quark masses and both channels within the UχPT parametrization with a very good χ^2. In Table 5.8 we list the pole mass and residue corresponding to this fit. These values are almost unchanged with respect to the σ channel fit, but the error bars are significantly

Fit	m_π	$\hat{l}_1 \times 10^3$	$\hat{l}_2 \times 10^3$	$L_2 \times 10^3$	$L_8 \times 10^3$	n	χ^2/ν
$\sigma + \rho$	227&315	2.24 ± 0.03	-3.44 ± 0.01	1.16 ± 0.12	-0.1 ± 0.7	44	1.1

Table 5.7: Combined fit for ρ and σ channels for UχPT model.
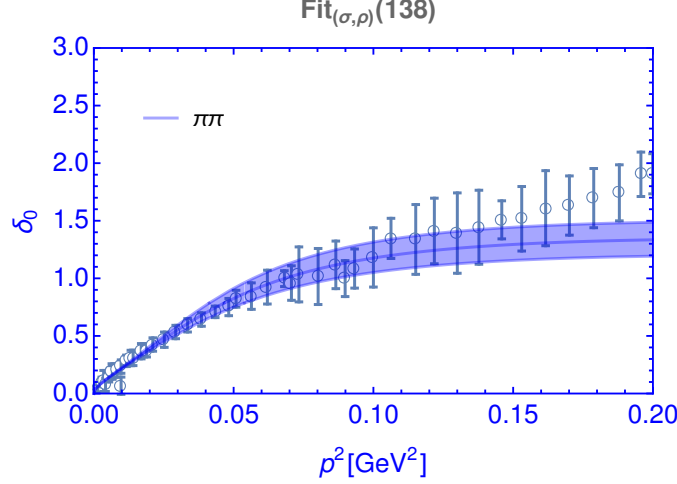
Figure 5.9: σ phase shift exptrapolation to physical point based on σ and ρ data.

smaller.

As discussed in Section 4.3, we can use UχPT to extrapolate the resonance parameters to the physical point. The extrapolated values to the physical point are included in the column labeled $m_\pi = 138\,\mathrm{MeV}$ in Table 5.8. In addition, we can do an extrapolation of the phase shifts to the physical point based on our lattice calculation with two unphysical pion masses. These extrapolated phase shifts are compared with the experimental ones in Fig. 5.9. Our extrapolated phase shifts are consistent with experimental data from [4] in the low-momentum region. At high momenta, the curve differs from experimental data, but this seems to be a feature of the UχPT model. This can be interpreted as the shoulder of the $f_0(980)$ resonance that has a strong $K\bar{K}$ component missing in the present two-flavor calculation and also the $U\chi PT$ model.

As a final test we compare our results with other lattice QCD studies. Since the UχPT parameterization can be used to extrapolate to different pion masses, we

Approach	138 MeV			227 MeV			315 MeV		
	Re$\sqrt{s_0}$	Im$\sqrt{s_0}$	$|g|$[GeV]	Re$\sqrt{s_0}$	Im$\sqrt{s_0}$	$|g|$[GeV]	Re$\sqrt{s_0}$	Im$\sqrt{s_0}$	$|g|$[GeV]
Conformal	-	-	-	460^{+30}_{-60}	-180^{+30}_{-30}	$3.16^{+0.1}_{-0.1}$	660^{+50}_{-70}	-150^{+50}_{-40}	$4.0^{+0.2}_{-0.2}$
UχPT(σ)	440^{+60}_{-90}	-240^{+40}_{-3}	$3.0^{+0.2}_{-0.6}$	490^{+100}_{-70}	-170^{+110}_{-40}	$3.0^{+0.7}_{-0.5}$	585^{+130}_{-120}	-80^{+80}_{-150}	$4.0^{+0.6}_{-2.0}$
UχPT($\sigma + \rho$)	440^{+10}_{-16}	-240^{+20}_{-20}	$2.97^{+0.02}_{-0.02}$	500^{+20}_{-20}	-160^{+15}_{-15}	$3.02^{+0.014}_{-0.04}$	600^{+30}_{-40}	-80^{+80}_{-20}	$3.9^{+0.5}_{-0.2}$

Table 5.8: σ resonance pole mass and pole residues for the fits discussed in the text.
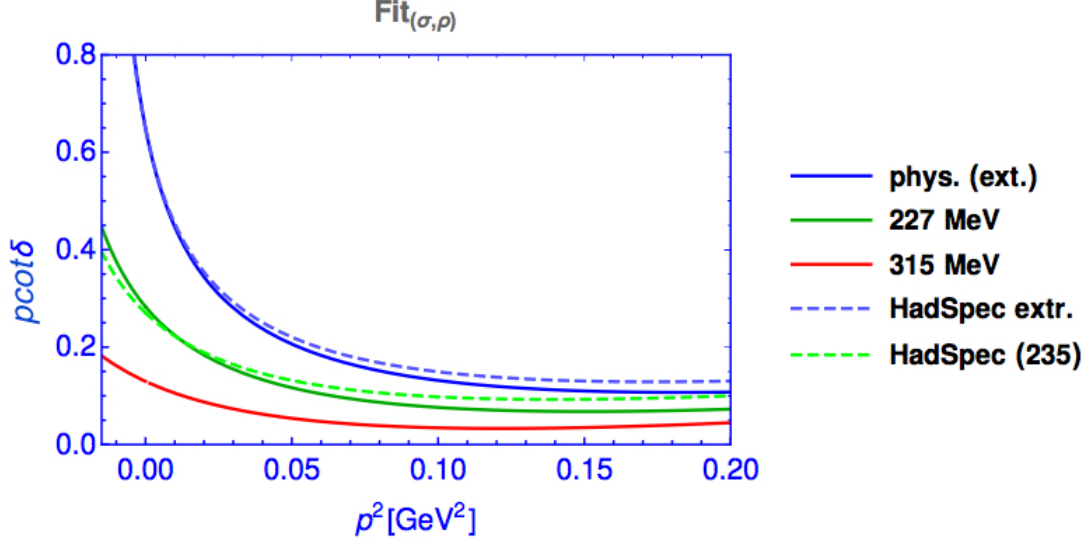
Figure 5.10: Comparison of the present result of the fit to the data to that of the HadronSpectrum collaboration [2, 3] and their extrapolation to the physical pion masses.

can compare the σ resonance properties calculated from different lattice groups. In Fig. 5.10 we compare our results to a recent lattice QCD study for σ meson done by Hadron Spectrum Collaboration (HadSpec) [3, 87]. The solid red and green curves are the $p \cot \delta$ parameterized by the UχPT model for the quark masses used in our study. The dashed green curve is the UχPT parameterization based on the HadSpec lattice calculation. We extrapolate HadSpec and our lattice calculations to the physical point noted by dashed blue and blue curves in Fig. 5.10. The extrapolation of $p \cot \delta$ to the physical point from these two different lattice calculations are nearly identical in the low-energy region and only slightly different in the higher-energy region.

Conclusions

We carried out a lattice QCD study of the σ resonance channel and extracted the phase shifts for pion-pion scattering in the $I = 0$, $J = 0$ channel for two different quark masses. Using a UχPT model, we extrapolated our results to the physical point and found a value for the pole mass of $W = (440^{+10}_{-16} - i240^{+20}_{-20})$ MeV. This is consistent

with the Particle Data Group experimental estimate [86] and other lattice studies of this channel [3, 87].

The errors quoted for the pole mass are purely statistical. The largest source of systematic errors is due to the model used to fit the phase shifts. Based on the standard deviation of the results from UχPT and conformal model, we estimate the systematic error to be about 5-10%. The other sources of systematic errors—lattice spacing, finite-volume correction, etc.—are subdominant.

Extracting the pole mass for the σ meson requires a parametrization for the phase shift. We feel confident in our use of the UχPT model, since the model is able to describe the data well in both σ and ρ channels. We note that we performed in this study the first simultaneous, fully-correlated fit to data extracted from lattice QCD for these two channels. This was possible because we could measure and include in the fit the relevant cross-correlations between the energies in these two channels.

The error bars for the energy levels extracted in this channel are significantly larger than in the ρ channel due to noise from the temporally disconnected diagrams listed in Eq. 4.69 and, surprisingly, worse for the heavier mass case. We plan to do a followup study using an increased set of interpolators to improve the signal. Two interesting directions are worth exploring: an improvement in the fitting strategy, in particular with respect to the method used to subtract the disconnected contributions, and adding tetraquark-like interpolators to the variational basis which are speculated to overlap better with the σ resonance.

Acknowledgements

A Numerical evaluation of zeta function

To compute the phase shift given in Eq. 4.27 and Eq.4.30, we need to numerically evaluate the zeta function. For the zero momentum case the relevant formulas for elongated boxes were derived in [60,88]. In the following we will show how to extend this to the non-zero momentum states, when the boost is parallel with the elongated direction of the box. We discuss first the evaluation of the zeta function for cubic boxes and then extend it to accommodate elongated boxes. For a boosted state with momentum $\boldsymbol{P} = \boldsymbol{d}2\pi/L$, the zeta function in a cubic box is

$$\mathcal{Z}^{\boldsymbol{d}}_{lm}(s;q,\gamma) = \sum_{\boldsymbol{n} \in P_{\boldsymbol{d}}(\gamma,\eta)} \frac{\mathcal{Y}_{lm}(\boldsymbol{n})}{(\boldsymbol{n}^2 - q^2)^s}, \tag{A.1}$$

with

$$P_{\boldsymbol{d}}(\gamma) = \left\{ \boldsymbol{n} \in \mathbb{R}^3 \middle| \boldsymbol{n} = \hat{\gamma}^{-1}\left(\boldsymbol{m} + \frac{\boldsymbol{d}}{2}\right), \boldsymbol{m} \in \mathbb{Z}^3 \right\}. \tag{A.2}$$

The series above is only convergent when $\operatorname{Re} s > l + 3/2$ but the zeta function needs to be evaluated at $s = 1$. The function defined by the series above can be analytically continued in the region $\operatorname{Re} s > 1/4$. The analytic continuation is done following Lüscher [59] and Rummukainen [61] using the heat kernel expansion

$$
\begin{aligned}
\mathcal{K}(t,\boldsymbol{x}) &= \frac{1}{(2\pi)^3} \sum_{\boldsymbol{n} \in P_{\boldsymbol{d}}(\gamma)} e^{i\boldsymbol{n}\cdot\boldsymbol{x} - t\boldsymbol{n}^2} \\
&= \frac{\gamma}{(4\pi t)^{\frac{3}{2}}} \sum_{\boldsymbol{n} \in P_{\boldsymbol{0}}(1/\gamma)} e^{i2\pi(\hat{\gamma}^{-1}\boldsymbol{n})\cdot\boldsymbol{d}/2} e^{-\frac{1}{4t}(\boldsymbol{x}+2\pi\boldsymbol{n})^2}.
\end{aligned} \tag{A.3}
$$

This relation is obtained using Poisson's summation formula

$$\sum_{n \in Z^3} f(\boldsymbol{n}) = \sum_{k \in Z^3} \int_{-\infty}^{\infty} f(\boldsymbol{x}) e^{i2\pi\boldsymbol{k}\cdot\boldsymbol{x}} d^3x. \tag{A.4}$$

The spherical projected kernel $\mathcal{K}_{lm}$ is defined as $\mathcal{K}_{lm} = \mathcal{Y}_{lm}(-i\nabla)\mathcal{K}$ which can be written as

$$
\begin{aligned}
\mathcal{K}_{lm}^{\boldsymbol{d}}(t, \boldsymbol{x}) &= (2\pi)^{-3/2} \sum_{\boldsymbol{n} \in P_{\boldsymbol{d}}} \mathcal{Y}_{lm}(\boldsymbol{n}) e^{(i\boldsymbol{n}\cdot\boldsymbol{x} - t\boldsymbol{n}^2)} \\
&= \frac{\gamma}{(4\pi t)^{3/2}} \frac{i^l}{(2t)^l} \sum_{\boldsymbol{n} \in Z^3} (-1)^{\boldsymbol{d}\cdot\boldsymbol{n}} \mathcal{Y}_{lm}(\boldsymbol{x} + 2\pi\hat{\gamma}\boldsymbol{n}) e^{-\frac{1}{4t}(\boldsymbol{x}+2\pi\hat{\gamma}\boldsymbol{n})^2} .
\end{aligned}
\tag{A.5}
$$

Using the truncated kernels $\mathcal{K}_{lm}^{\Lambda} = \mathcal{Y}_{lm}(-i\nabla)\mathcal{K}^{\Lambda}$ with

$$
\mathcal{K}^{\Lambda}(t, \boldsymbol{x}) \equiv \frac{1}{(2\pi)^3} \sum_{\boldsymbol{n} \in P_{\boldsymbol{d}}(\gamma), |\boldsymbol{n}| \leq \Lambda} e^{i\boldsymbol{n}\cdot\boldsymbol{x} - t\boldsymbol{n}^2} ,
\tag{A.6}
$$

we define the zeta function by separating the series terms in two groups, a finite set close to the origin that remains in the original form, and the rest that will be evaluated via an kernel integral:

$$
\begin{aligned}
&\mathcal{Z}_{lm}^{\boldsymbol{d}}(s; q, \gamma) \\
&= \sum_{\substack{\boldsymbol{n} \in P_{\boldsymbol{d}}(\gamma) \\ |\boldsymbol{n}| < \Lambda}} \frac{\mathcal{Y}_{lm}(\boldsymbol{n})}{(\boldsymbol{n}^2 - q^2)^s} + \frac{(2\pi)^3}{\Gamma(s)} \left\{ \frac{\delta_{l0}\delta_{m0}\gamma}{(4\pi)^2(s - 3/2)} \right. \\
&\quad + \int_0^1 dt\, t^{s-1} \left[e^{tq^2} \mathcal{K}_{lm}^{\Lambda}(t, \boldsymbol{0}) - \frac{\delta_{l0}\delta_{m0}\gamma}{(4\pi)^2 t^{3/2}} \right] \\
&\quad \left. + \int_1^{\infty} e^{tq^2} \mathcal{K}_{lm}^{\Lambda}(t, \boldsymbol{0}) \right\} .
\end{aligned}
\tag{A.7}
$$

For the integral on the $t \in [1, \infty]$ range, the heat kernel expansion in terms of $\exp(i\boldsymbol{n} \cdot \boldsymbol{x} - t\boldsymbol{n}^2)$ is used, and on the $t \in [0, 1]$ range, the expansion in terms of $\exp[-(\boldsymbol{x} + 2\pi\boldsymbol{n})^2/4t]$ is used. In both cases the series converges the slowest around $t = 1$: for the $t \in [1, \infty]$ range large $\boldsymbol{n}$ terms contribute $\exp(-t(\boldsymbol{n}^2 - q^2))$ and on the $t \in [0, 1]$ range they contribute $\exp[tq^2 - (2\pi\boldsymbol{n})^2/4t]$. It is clear that this series converges quickly for large $\boldsymbol{n}$ if we choose $\Lambda > \operatorname{Re} q^2$. For the A_2^- irrep we need to

evaluate $\mathcal{Z}^{\boldsymbol{d}}_{00}$ and $\mathcal{Z}^{\boldsymbol{d}}_{20}$. For $\mathcal{Z}^{\boldsymbol{d}}_{00}$, we have

$$
\begin{aligned}
\mathcal{Z}^{\boldsymbol{d}}_{00}&(s; q, \gamma)\\
&= \sum_{\substack{\boldsymbol{n} \in P_{\boldsymbol{d}}(\gamma) \\ |\boldsymbol{n}| \leq \Lambda}} \frac{\mathcal{Y}_{00}(\boldsymbol{n})}{(\boldsymbol{n}^2 - q^2)^s} + \frac{\pi\gamma}{2\Gamma(s)(s - 3/2)} \\
&+ \gamma \sum_{\boldsymbol{n} \in P_{\boldsymbol{0}}(1/\gamma)} e^{i2\pi(\hat{\gamma}^{-1}\boldsymbol{n})\cdot\boldsymbol{d}/2} \mathcal{Y}_{00}(\boldsymbol{n}) I_{00}(s, q, |\boldsymbol{n}|) \\
&- \sum_{\substack{\boldsymbol{n} \in P_{\boldsymbol{d}}(\gamma) \\ |\boldsymbol{n}| \leq \Lambda}} \mathcal{Y}_{00}(\boldsymbol{n}) \underline{J}_{00}(s, q, |\boldsymbol{n}|) \\
&+ \sum_{\substack{\boldsymbol{n} \in P_{\boldsymbol{d}}(\gamma) \\ |\boldsymbol{n}| > \Lambda}} \mathcal{Y}_{00}(\boldsymbol{n}) \bar{J}_{00}(s, q, \gamma, |\boldsymbol{n}|) \,,
\end{aligned}
\tag{A.8}
$$

where $\mathcal{Y}_{00}(\boldsymbol{n}) = \frac{1}{\sqrt{4\pi}}$ and the notation used is:

$$
\begin{aligned}
I_{00}(s, q, |\boldsymbol{n}|) &= \frac{(2\pi)^3}{\Gamma(s)} \int_0^1 dt\, t^{s-1} \frac{\left(e^{tq^2 - (2\pi\boldsymbol{n})^2/4t} - \delta_{|\boldsymbol{n}|0}\right)}{(4\pi t)^{3/2}} \,, \\
\underline{J}_{00}(s, q, |\boldsymbol{n}|) &= \frac{1}{\Gamma(s)} \int_0^1 dt\, t^{s-1} e^{tq^2} e^{-t\boldsymbol{n}^2} \,, \\
\bar{J}_{00}(s, q, |\boldsymbol{n}|) &= \frac{1}{\Gamma(s)} \int_1^\infty dt\, t^{s-1} e^{tq^2} e^{-t\boldsymbol{n}^2} \\
&= \frac{1}{(\boldsymbol{n}^2 - q^2)^s} - \underline{J}_{00}(s, q, |\boldsymbol{n}|) \,.
\end{aligned}
\tag{A.9}
$$

These functions can be expressed in terms of Euler gamma function and exponential integral function

$$
\Gamma(s, z) = \int_z^\infty t^{s-1} e^{-t} dt \,, \quad E_n(z) = \int_1^\infty \frac{e^{-zt}}{t^n} dt \,.
\tag{A.10}
$$

We have

$$
\begin{aligned}
\underline{J}_{00}(s, q, |\boldsymbol{n}|) &= \frac{1}{(\boldsymbol{n}^2 - q^2)^s} \left(1 - \frac{\Gamma(s, \boldsymbol{n}^2 - q^2)}{\Gamma(s, 0)}\right) \,, \\
\bar{J}_{00}(s, q, |\boldsymbol{n}|) &= E_{1-s}(\boldsymbol{n}^2 - q^2) \text{ for } \mathbf{n}^2 > q^2 \,.
\end{aligned}
\tag{A.11}
$$

Therefore, the zeta function can be simplified to

$$\mathcal{Z}_{00}^{d}(s;q,\gamma) = \frac{\pi\gamma}{2\Gamma(s)(s-3/2)} + \sum_{\boldsymbol{n}\in P_{\boldsymbol{n}}(\gamma)} \mathcal{Y}_{00}(\boldsymbol{n})\bar{J}_{00}(s,q,|\boldsymbol{n}|)$$

$$+ \gamma \sum_{\boldsymbol{n}\in P_{\boldsymbol{0}}(1/\gamma)} e^{i2\pi(\hat{\gamma}^{-1}\boldsymbol{n})\cdot\boldsymbol{d}/2} \mathcal{Y}_{00}(\boldsymbol{n}) I_{00}(s,q,|\boldsymbol{n}|),$$

$$\mathcal{Z}_{20}^{d}(s;q,\gamma) = \gamma \sum_{\boldsymbol{n}\in P_{\boldsymbol{0}}(1/\gamma)} e^{i2\pi(\hat{\gamma}^{-1}\boldsymbol{n})\cdot\boldsymbol{d}/2} \mathcal{Y}_{20}(\boldsymbol{n}) I_{20}(s,q,|\boldsymbol{n}|)$$

$$+ \sum_{\boldsymbol{n}\in P_{\boldsymbol{d}}(r)} \mathcal{Y}_{20}(\boldsymbol{n})\bar{J}_{00}(s,q,|\boldsymbol{n}|).$$

(A.12)

For the case of interest, $s=1$, the J_{00} and I_{00} integrals are

$$\bar{J}_{00}(1,q,|\boldsymbol{n}|) = \frac{e^{-(\boldsymbol{n}^2-q^2)}}{\boldsymbol{n}^2-q^2},$$

$$I_{00}(1,q,0) = 2\pi^{3/2}[1-e^{q^2}-\sqrt{\pi}iq\operatorname{erf}(iq)],$$

$$I_{00}(1,q,|\boldsymbol{n}|\neq 0) = \frac{\pi}{|\boldsymbol{n}|}Re[e^{2\pi iq|\boldsymbol{n}|}(1-\operatorname{erf}(iq+\pi|\boldsymbol{n}|))].$$

(A.13)

Similarly, for $s=1$, the I_{20} integral can simplify to

$$I_{20}(1,q,|\boldsymbol{n}|) = -\frac{(3+2\boldsymbol{n}^2)e^{q^2-(\pi\boldsymbol{n})^2}}{2|\boldsymbol{n}|^4\sqrt{\pi}}$$

$$+ Re\frac{e^{2\pi iq|\boldsymbol{n}|}[-3+2\pi q|\boldsymbol{n}|(3i+2\pi q|\boldsymbol{n}|)][1-\operatorname{erf}(iq+\pi|\boldsymbol{n}|)]}{4|\boldsymbol{n}|^5\pi}$$

(A.14)

where the error function is defined as

$$\operatorname{erf}(z) = \frac{2}{\sqrt{\pi}}\int_0^z e^{-t^2}dt.$$

(A.15)

All the relations above work for $\boldsymbol{n}^2-q^2\neq 0$. The series are divergent at the points where $\boldsymbol{n}^2=q^2$. To avoid this trivial divergence these points are removed from the

summation, that is

$$\mathcal{Z}^{\boldsymbol{d}}_{lm}(s;q,\gamma) = \sum_{\substack{\boldsymbol{n}\in P_{\boldsymbol{d}}(\gamma) \\ \boldsymbol{n}^2 \neq q^2}} \frac{\mathcal{Y}_{lm}(\boldsymbol{n})}{(\boldsymbol{n}^2 - q^2)^s} \,. \tag{A.16}$$

This basically amounts to replacing $1/(\boldsymbol{n}^2 - q^2)$ with 0 when $\boldsymbol{n}^2 = q^2$. In the simplified expressions above this is equivalent to setting

$$\bar{J}_{lm}(s,q,|\boldsymbol{n}|) = -\frac{1}{s\Gamma(s)} \tag{A.17}$$

when $q^2 = |\boldsymbol{n}|^2$. This is because the convergent counterpart $\underline{J}_{lm}(s,q,|\boldsymbol{n}|) = 1/s\Gamma(s)$ for $s > 0$ when $q^2 = \boldsymbol{n}^2$ and the sum of $\bar{J}_{lm}$ and $\underline{J}_{lm}$ is $1/(\boldsymbol{n}^2 - q^2)$ which is replaced with 0.

For the elongated box case the zeta functions also depend on the elongation factor η. The only difference is the domain of the summation which becomes

$$P_{\boldsymbol{d}}(\gamma,\eta) = \left\{ \boldsymbol{n} \in \mathbb{R}^3 \,\middle|\, \boldsymbol{n} = \hat{\gamma}^{-1}\hat{\eta}^{-1}(\boldsymbol{m} + \frac{\boldsymbol{d}}{2}), \boldsymbol{m} \in \mathbb{Z}^3 \right\}, \tag{A.18}$$

where $\hat{\gamma}$ and $\hat{\eta}$ are defined in Eq. 4.33 and Eq. 4.36. In sum, they can be calculated as

$$\begin{aligned}
\mathcal{Z}^{\boldsymbol{d}}_{00}(s;q,\gamma,\eta) &= \mathcal{Z}^{\boldsymbol{d}}_{00}(s;q,\gamma\eta)\,, \\
\mathcal{Z}^{\boldsymbol{d}}_{20}(s;q,\gamma,\eta) &= \mathcal{Z}^{\boldsymbol{d}}_{20}(s;q,\gamma\eta)\,.
\end{aligned} \tag{A.19}$$

B Unitarized chiral perturbation theory model

B.1 Single channel

In the context of the Inverse Amplitude method [89–93], the T-matrix is given by

$$T = [I - VG]^{-1}V \tag{B.1}$$

where

$$V = V_2[V_2 - V_4]^{-1}V_2 \,. \tag{B.2}$$

where V_2 and V_4 are potentials evaluated from the $\mathcal{O}(p^2)$ and $\mathcal{O}(p^4)$ Lagrangians of the χPT expansion. In Eq. B.1, G is a diagonal matrix whose elements are the two-meson loop functions, evaluated in our case in dimensional regularization in contrast to the cut-off-scheme used in the original model of Ref. [94]:

$$
\begin{aligned}
G_{ii}^{DR}(E) \quad &= i \int \frac{d^4q}{(2\pi)^4} \frac{1}{q^2 - m_1^2 + i\epsilon} \frac{1}{(P-q)^2 - m_2^2 + i\epsilon} \\
&= \frac{1}{16\pi^2} \left\{ a(\mu) + \ln \frac{m_1^2}{\mu^2} + \frac{m_2^2 - m_1^2 + E^2}{2E^2} \ln \frac{m_2^2}{m_1^2} \right. \\
&\quad + \frac{p_i}{E} \left[\ln(\ E^2 - (m_1^2 - m_2^2) + 2p_iE) \right. \\
&\quad + \ln(\ E^2 + (m_1^2 - m_2^2) + 2p_iE) \\
&\quad - \ln(-E^2 + (m_1^2 - m_2^2) + 2p_iE) \\
&\quad \left. \left. - \ln(-E^2 - (m_1^2 - m_2^2) + 2p_iE) \right] \right\} ,
\end{aligned}
\tag{B.3}
$$

where $p_i = \frac{\sqrt{(E^2 - (m_1+m_2)^2)(E^2 - (m_1-m_2)^2)}}{2E}$ for the channel i, E is the center-of-mass energy, and $m_{1,2}$ refers to the masses of the mesons $1, 2$ in the i channel. Throughout this study we use $\mu = 1$ GeV and a natural value of the subtraction constant $a(\mu) = -1.28$.

For the case of the π-π interaction with $(I = 1; L = 1)$, the kernel of Eq. B.1, $V(\pi\pi)$, can be expressed as [94]

$$V(\pi\pi) = \frac{-2\,p^2}{3(f_\pi^2 - 8\,\hat{l}_1 m_\pi^2 + 4\,\hat{l}_2 E^2)} \,, \tag{B.4}$$

where specific combinations of LECs have been introduced, $\hat{l}_1 \equiv 2\,L_4 + L_5$ and $\hat{l}_2 \equiv 2\,L_1 - L_2 + L_3$. Note that these are not identical to the SU(2) CHPT low-energy constants. The one-channel reduction given by Eq. B.4, which contains the lowest- and

next-to-leading order contributions, constitutes the fit model for the $N_f = 2$ lattice data of this study.

For the case of isospin $I = 0$ channel of π-π interaction, the leading order, V_2 and the next higher order potential, V, potentials projected in s-wave are,

$$V_2 = \frac{m_\pi^2 - 2s}{2f_\pi^2},$$

$$V = \frac{3(m_\pi^2 - 2s)^2}{6f^2(m_\pi^2 - 2s) + 8(L_a m_\pi^4 + s(L_b m_\pi^2 + L_c s))}. \tag{B.5}$$

The combination of LECs, L_a, L_b and L_c which enter in the next leading order term are,

$$\begin{aligned}
L_a/4 &= -9\,\hat{l}_1 + 50\,L_1 - 14\,\hat{l}_2 + 25\,L_3 + 30\,L_6 + 15\,L_8\,, \\
L_b/4 &= 3\,\hat{l}_1 + 10\left(-4\,L_1 + \hat{l}_2 - 2\,L_3\right), \\
L_c &= 50\,L_1 - 14\,\hat{l}_2 + 25\,L_3\,.
\end{aligned} \tag{B.6}$$

B.2 Coupled channel case $\left(\pi\pi - K\overline{K}\right)$

In this section we describe the meson-meson interaction in terms of the partial-wave decomposition of the amplitude and apply it to the case of the $\pi\pi - K\overline{K}$ system with quantum numbers $(L = 1; I = 1)$. The partial wave decomposition of the scattering amplitude of two spinless mesons with definite isospin I can be written as

$$T_I = \sum_J (2J+1)T_{IJ}P_J(\cos\theta)\,. \tag{B.7}$$

where

$$T_{IJ} = \frac{1}{2}\int_{-1}^{1} P_J(\cos\theta)T_I(\theta)\,\mathrm{d}\cos\theta\,. \tag{B.8}$$

In the case of two coupled channels, T_{IJ} is a 2×2 matrix whose elements $(T_{IJ})_{ij}$ are related to S matrix elements through the equations (omitting the I, J labels from

here on)

$$(T)_{11} = -\frac{8\pi E}{2ip_1}[(S)_{11} - 1], \quad (T)_{22} = -\frac{8\pi E}{2ip_2}[(S)_{22} - 1],$$
$$(T)_{12} = (T)_{21} = -\frac{8\pi E}{2i\sqrt{p_1 p_2}}(S)_{12}, \tag{B.9}$$

with p_1, p_2 the center-of-mas momenta of the mesons in channel 1 $(\pi\pi)$ or 2 $(K\overline{K})$ respectively, that is $p_i = \sqrt{(E/2)^2 - m_i^2}$. The S-matrix can be parametrized as

$$S = \begin{pmatrix} \eta e^{2i\delta_1} & i(1-\eta^2)^{1/2}e^{i(\delta_1+\delta_2)} \\ i(1-\eta^2)^{1/2}e^{i(\delta_1+\delta_2)} & \eta e^{2i\delta_2} \end{pmatrix}. \tag{B.10}$$

The interaction in the $\pi\pi - K\overline{K}$ system, is evaluated from the $\mathcal{O}(p^2)$ and $\mathcal{O}(p^4)$ Lagrangians of the χPT expansion [64,65]. The potentials, V_2 and V_4, projected in $I = 1$ and $L = 1$ are [94]

$$V_2(E) = -\begin{pmatrix} \frac{2p_\pi^2}{3f_\pi^2} & \frac{\sqrt{2}p_K p_\pi}{3f_K f_\pi} \\ \frac{\sqrt{2}p_K p_\pi}{3f_K f_\pi} & \frac{p_K^2}{3f_K^2} \end{pmatrix} \tag{B.11}$$

$$V_4(E) = -1\times$$
$$\begin{pmatrix} \frac{8p_\pi^2(2\hat{l}_1 m_\pi^2 - \hat{l}_2 E^2)}{3f_\pi^4} & \frac{8p_\pi p_K(L_5(m_K^2+m_\pi^2)-L_3 E^2)}{3\sqrt{2}f_\pi^2 f_K^2} \\ \frac{8p_\pi p_K(L_5(m_K^2+m_\pi^2)-L_3 E^2)}{3\sqrt{2}f_\pi^2 f_K^2} & \frac{4p_K^2(10\hat{l}_1 m_K^2 + 3(L_3-2\hat{l}_2)E^2)}{9f_K^4} \end{pmatrix}. \tag{B.12}$$

The two-channel T-matrix is evaluated by means of Eq. B.1. Note that the channel transitions in Eqs. B.11 and B.12 depend on four low energy constants, $\hat{l}_1$, $\hat{l}_2$, L_3 and L_5.

B.3 Meson-meson energies in the finite volume from UχPT model

In Refs. [66, 95, 96], a formalism has been developed that is equivalent to the Lüscher framework up to exponentially suppressed corrections. The formalism is summarized in this section. Given the two-meson-interaction potential, as the V with the $\mathcal{O}(p^2)$ and $\mathcal{O}(p^4)$ terms in the χPT expansion, that is Eqs. B.2, B.11 and B.12, the scattering amplitude in the finite volume can be written as,

$$\tilde{T} = [I - V\tilde{G}]^{-1}V\,, \tag{B.13}$$

or $\tilde{T} = [V^{-1} - \tilde{G}]^{-1}$, similarly to Eq. B.1 in the infinite-volume limit. In the case of boxes with asymmetry η in the z direction, $\tilde{G}$ can be evaluated as,

$$\tilde{G}(E) = \frac{1}{\eta L^3} \sum_{\boldsymbol{q}} I(E, \boldsymbol{q})\,, \tag{B.14}$$

where the channel index has been omitted. Here,

$$I(E, \mathbf{q}) = \frac{\omega_1(\boldsymbol{q}) + \omega_2(\boldsymbol{q})}{2\omega_1(\boldsymbol{q})\omega_2(\boldsymbol{q})} \frac{1}{E^2 - (\omega_1(\boldsymbol{q})^2 + \omega_2(\boldsymbol{q})^2)}\,, \tag{B.15}$$

where $\boldsymbol{q} = \frac{2\pi}{L}(n_x, n_y, n_z/\eta)$. The sum over the momenta is cut off at q_{max}. The formalism can also be made independent of q_{max} and related to the subtraction constant in the dimensional-regularization method, α (as in the continuum limit), see Ref [97],

$$\tilde{G} = G^{DR} +$$
$$\lim_{q_{\mathrm{max}} \to \infty} \left(\frac{1}{\eta L^3} \sum_{q < q_{\mathrm{max}}} I(E, \boldsymbol{q}) - \int_{q < q_{\mathrm{max}}} \frac{d^3q}{(2\pi)^3} I(E, \boldsymbol{q}) \right) \tag{B.16}$$
$$\equiv G^{DR} + \lim_{q_{\mathrm{max}} \to \infty} \delta G\,,$$

114

where G^{DR} stands for the two-meson loop function given in Eq. B.3. For energies E_i which correspond to poles of $\tilde{T}$, i.e., the energy eigenvalues in the finite volume, we can obtain the T matrix in the infinite volume,

$$T = [\tilde{G}(E) - G(E)]^{-1} \tag{B.17}$$

which is independent of the renormalization of the individually divergent expressions.

In the general multi-channel case, the energy spectrum in a box, predicted by UχPT, is found as solution of the equation

$$\text{Det}[V^{-1}(E) - \tilde{G}(E)] = 0 \ . \tag{B.18}$$

As has been shown in Ref. [66], the formalism of Refs. [66, 95, 96] is equivalent to the Lüscher approach up to contributions which are exponentially suppressed with the volume. In what follows, we refer to Ref. [98] for the generalization of the formalism to moving frames. The formalism of Ref. [98] is generalized to include partial wave mixing and coupled channels, but in the current study the F wave is neglected.

For an equal-mass system interacting in p-wave and moving with $\boldsymbol{P} = \frac{2\pi}{\eta L}(0, 0, 1)$ in the direction of the elongation of the box, we find the following relations,

$$A_2^- : \qquad -1 + V(\pi\pi)\tilde{G}_{10,10} = 0 \tag{B.19}$$

$$E^- : \qquad -1 + V(\pi\pi)\tilde{G}_{11,11} = 0 \ , \tag{B.20}$$

with $\tilde{G}_{lm,l'm'}$ given in Ref. [98] but modified as in Eqs. B.15 and B.16 by the elongation factor η. Above, $V(\pi\pi)$ is from Eq. B.4. The above relations are used to fit $\hat{l}_1$, $\hat{l}_2$ directly to the energy levels in the finite volume.

We have also checked that the numerical results for the phase shifts derived from Eq. B.19 are very similar to those in Appendix A when the argument of the integrand
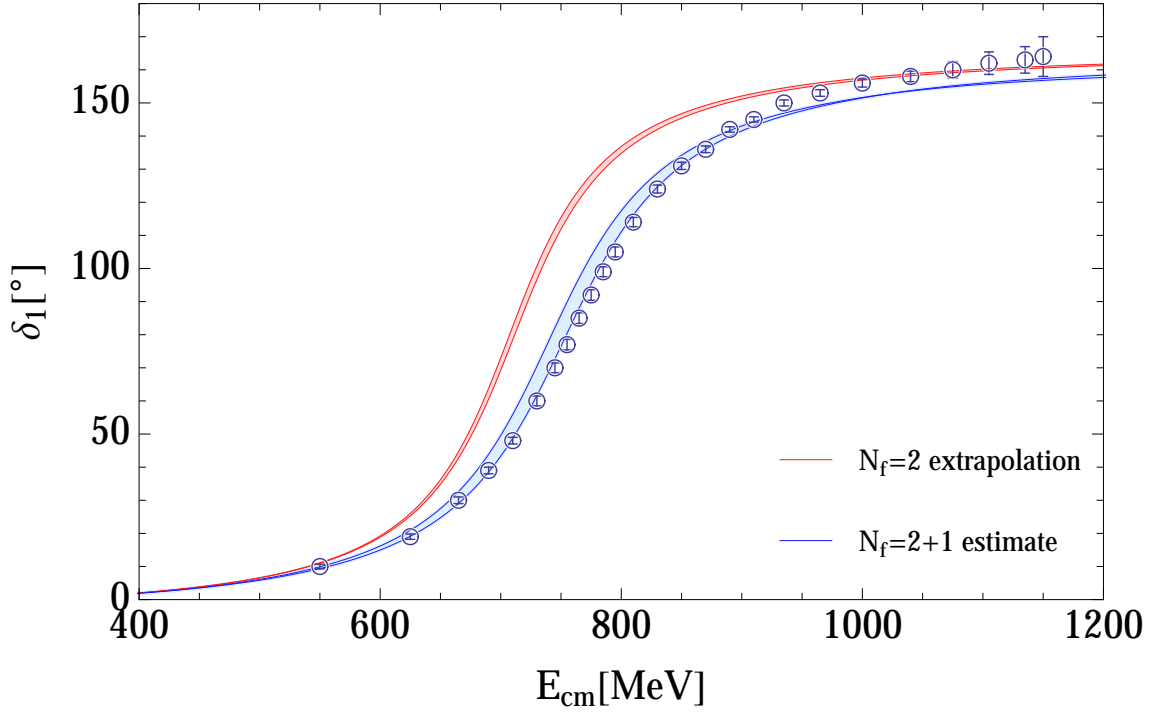
Figure B.1: Chiral extrapolation of the phase shift to the physical mass (red band), obtained from the simultaneous fit to lattice eigenvalues at both considered pion masses. The blue band shows the phase shifts extrapolated to the physical point.

$I(E, \boldsymbol{q})$ from Eq. B.15 is replaced as described in Ref. [66], $I(E, \boldsymbol{q}) \rightarrow (2E)^{-1}(p^2 - \boldsymbol{q}^2)^{-1}$, to remove exponentially suppresed contributions and ensure comparability with the Lüscher formalism. See also Eq. 18 of Ref. [98] for the replacement in case of moving frames. In any case, these exponentially suppressed contributions are small in the present case.

B.4   Additional UχPT fit results for ρ resonance

The combined UχPT fit to eigenvalues at both pion masses is discussed in Sec. 5.2. We do not display the fit because it is almost indistinguishable from the blue curves in Fig. 5.4. The result of the chiral extrapolation is shown in Fig. B.1 with the red band indicating the statistical uncertainties. The blue band shows the estimated phase shift

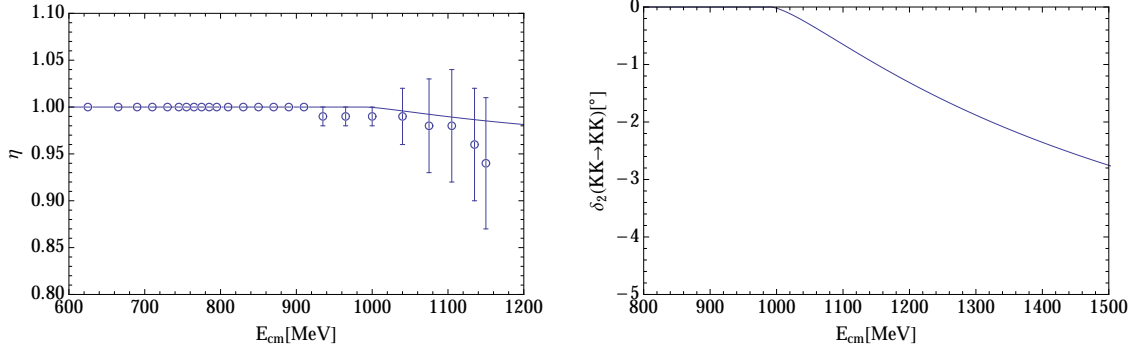Figure B.2: Left: Elasticity of $\pi\pi \to \pi\pi$ at physical pion masses compared with experimental determinations [4]. Right: Phase shift $\delta_2(K\overline{K} \to K\overline{K})$.

when including also the $K\overline{K}$ channel in the two variants mentioned in the text. To keep the figure simple, statistical uncertainties are not indicated for these cases. They are of the same size as the red band. Open circles indicate phase shifts extracted from experiment [4]. The experimental data of Ref. [4] are depicted with circles. As one can see, the $N_f = 2$ extrapolation remains far from the experimental data.

The two-channel UχPT formalism allows to estimate the effect of the missing strange quark in terms of the $K\overline{K}$ channel. For this, the T-matrix scattering amplitude, Eq. B.1, is evaluated with the kernel V from Eqs. B.2, B.11 and B.12. The LECs in the $\pi\pi \to \pi\pi$ transition $\hat{l}_1$ and $\hat{l}_2$ are fixed at their values from the combined fit to the $N_f = 2$ lattice data (see Table 5.3).

The combinations of LECs appearing in the $\pi\pi \to K\overline{K}$ and the $K\overline{K} \to K\overline{K}$ transitions of Eq. B.12 are different from those of $\pi\pi \to \pi\pi$ and taken from a global fit to $\pi\pi$ and πK experimental phase shift data, similar as in Ref. [99]. Statistical uncertainties from this source are not considered, because they are smaller than those from lattice data. The relevant values from this fit are $L_3 = -3.01(2) \times 10^{-3}$ and $L_5 = 0.64(3) \times 10^{-3}$, $\hat{l}_1 = 0.26(5) \times 10^{-3}$, $\hat{l}_2 = -3.96(4) \times 10^{-3}$.

However, note that $\hat{l}_1$ and $\hat{l}_2$ also appear in the $\pi\pi \to K\overline{K}$ and the $K\overline{K} \to K\overline{K}$ transitions (see Eq. B.12). It is then not clear which values of $\hat{l}_i$ to use in these

117

transitions. We have tested two variants:

1. Evaluate the $\pi\pi \to K\overline{K}$ and $K\overline{K} \to K\overline{K}$ transitions with the $\hat{l}_1$ and $\hat{l}_2$ from the fit to $N_f = 2$ lattice data.

2. Set all the LECs involved in the $\pi\pi \to K\overline{K}$ and $K\overline{K} \to K\overline{K}$ transitions to the LECs from the mentioned fit to experimental data.

As Table 5.3 shows, the $\hat{l}_i$ from the fit to $N_f = 2$ lattice data are similar to the ones quoted above, but not entirely compatible.

The result of the $2 \to 3$ flavor extrapolation with these two variants is shown in Fig. B.1 with the two blue curves connected by the blue band. The difference between these two strategies leads to about 20 MeV difference in the mass of the $\rho(770)$ meson which gives an estimation of the uncertainties from model consistency.

Even though the $K\overline{K}$ channel has a significant impact on the mass of the ρ, the elasticity remains close to unity when this channel is open. This is shown in Fig. B.2 (left). The $K\overline{K}$-phase shift is small and negative, as shown in Fig. B.2 (right). We only show the result of variant 2 discussed in the text (results for variant 1 are very similar). It has the same sign as determined in Ref. [16] at an unphysical pion mass.

In summary, even with the discussed theoretical uncertainty, the shift of the ρ mass by the $K\overline{K}$ channel is significant and leads to a surprisingly good post-diction of experiment.

C   Extracted energies and correlation matrices

C.1 ρ meson

In this section, we tabulate the details about fitting—fitting ansatz and fitting windows—for each energy level and for each ensemble used in this study. These details are reported in Table C.1. The ansatz labels the fitting function used; referring to

Section 3.5 we have: d stands for double exponential function $f_1(t)$, dc is a double exponential function plus a constant term $f_2(t)$, and dt stands for its boosted variant $f_3(t)$. Q is the confidence level of the fit, that is the probability under ideal conditions that the χ^2 is larger than the fit result.

m_π(MeV)	$\mathbf{P}$	η	n	ansatz	t_0	fit window	aE	χ^2/dof	Q
315	$(0,0,0)$	1.0	1	d	3	$3-20$	0.4932(16)	0.65	0.83
			2	d	3	$5-15$	0.6612(14)	0.61	0.77
			3	d	3	$4-10$	0.842(4)	0.61	0.65
		1.25	1	d	3	$4-15$	0.4847(14)	1.5	0.13
			2	d	3	$5-14$	0.5891(14)	1.5	0.16
			3	d	3	$4-12$	0.785(5)	0.82	0.55
		2.0	1	dc	3	$4-16$	0.4508(6)	0.96	0.47
			2	d	3	$6-17$	0.5098(18)	1.23	0.27
			3	d	3	$5-15$	0.6547(13)	0.92	0.49
			4	d	3	$3-12$	0.704(2)	0.09	0.99
	$(0,0,1)$	1.0	1	dt	3	$5-17$	0.5024(8)	0.64	0.77
			2	d	3	$5-16$	0.5768(15)	0.47	0.89
			3	d	3	$3-13$	0.7492(15)	0.30	0.96
		1.25	1	dt	3	$7-15$	0.4701(9)	0.69	0.63
			2	d	3	$5-16$	0.547(2)	0.95	0.47
			3	d	3	$3-13$	0.717(2)	0.30	0.97
		2.0	1	dt	3	$3-20$	0.4241(7)	0.95	0.50
			2	d	3	$5-20$	0.5036(9)	1.36	0.17
			3	d	3	$5-17$	0.574(1)	0.38	0.96
			4	d	3	$3-13$	0.676(1)	0.37	0.94
226	$(0,0,0)$	1.0	1	d	3	$3-15$	0.4598(15)	0.82	0.61
			2	d	3	$3-12$	0.6184(15)	0.09	0.99
			3	d	3	$3-8$	0.820(8)	0.08	0.97
		1.17	1	d	3	$3-12$	0.448(2)	1.06	0.39
			2	d	3	$3-12$	0.558(2)	1.24	0.28
			3	d	3	$3-10$	0.744(18)	0.05	0.99
		1.33	1	d	3	$3-13$	0.4300(15)	0.44	0.90
			2	d	3	$3-14$	0.527(2)	0.35	0.96
			3	d	3	$3-11$	0.71(2)	0.08	0.99
	$(0,0,1)$	1.0	1	d	3	$6-18$	0.4217(9)	0.68	0.75
			2	d	3	$5-16$	0.5489(13)	0.68	0.73
			3	d	3	$3-12$	0.706(2)	0.19	0.99
		1.17	1	d	3	$6-20$	0.391(1)	0.32	0.99
			2	d	3	$3-12$	0.530(1)	0.88	0.52
			3	d	3	$3-10$	0.672(3)	0.70	0.63
		1.33	1	dt	3	$6-20$	0.371(1)	0.31	0.98
			2	d	3	$3-13$	0.5095(11)	0.97	0.46
			3	d	3	$3-11$	0.656(2)	0.17	0.98
			4	d	3	$3-11$	0.665(17)	1.09	0.26

Table C.1: Extracted energies and fitting details for ρ meson.

$$
\begin{pmatrix}
24.8 & 1.76 & 5.95 & 3.34 & 2.43 & 3.47 \\
 & 20.4 & 14.7 & 4.04 & 6.74 & 12.4 \\
 & & 164 & 4.01 & 5.22 & 25.6 \\
 & & & 6.8 & 2.67 & 4.16 \\
 & & & & 23.4 & 3.74 \\
 & & & & & 24.4
\end{pmatrix} \times 10^{-7}
\qquad
\begin{pmatrix}
24.0 & -3.91 & -34.0 & 4.0 & 3.6 & -2.52 \\
 & 23.8 & 71.0 & 3.57 & 4.02 & 10.0 \\
 & & 760 & -3.77 & 23.5 & 59.0 \\
 & & & 8.71 & 1.18 & 3.17 \\
 & & & & 15.9 & -2.22 \\
 & & & & & 41.0
\end{pmatrix} \times 10^{-7}
$$

$$
\begin{pmatrix}
19.5 & -2.03 & -0.256 & 3.44 & 8.23 & -2.92 \\
 & 21.1 & 11.2 & 2.04 & 7.80 & 66.7 \\
 & & 234 & 5.11 & 4.36 & 51.6 \\
 & & & 8.34 & 2.63 & 0.536 \\
 & & & & 30.0 & 0.269 \\
 & & & & & 41.8
\end{pmatrix} \times 10^{-7}
\qquad
\begin{pmatrix}
33.9 & -14.7 & -44.4 & 1.09 & 5.67 & -10.8 \\
 & 43.1 & 145 & 1.60 & 2.56 & 22.3 \\
 & & 2720 & 11.4 & 12.9 & 144 \\
 & & & 9.73 & 0.885 & 2.98 \\
 & & & & 12.1 & -0.436 \\
 & & & & & 68.2
\end{pmatrix} \times 10^{-7}
$$

$$
\begin{pmatrix}
3.62 & 2.24 & 1.54 & 1.87 & 3.16 & 3.10 & 1.90 & 1.74 \\
 & 32.4 & 0.195 & 3.15 & 1.71 & 8.42 & 2.34 & 0.884 \\
 & & 15.8 & 9.77 & 3.04 & -0.063 & 9.99 & 6.21 \\
 & & & 41.8 & 2.96 & 1.40 & 7.16 & 16.2 \\
 & & & & 4.29 & 1.48 & 2.97 & 2.20 \\
 & & & & & 9.57 & 0.90 & 0.222 \\
 & & & & & & 10.1 & 4.62 \\
 & & & & & & & 9.78
\end{pmatrix} \times 10^{-7}
\qquad
\begin{pmatrix}
22.8 & -5.91 & -63.6 & 4.54 & 5.92 & -3.50 & -24.6 \\
 & 42.8 & 108 & 3.80 & 5.21 & 18.6 & 32.9 \\
 & & 5430 & 93.7 & -29.2 & 32.6 & 1690 \\
 & & & 19.3 & 2.78 & 1.62 & 57.4 \\
 & & & & 14.2 & 2.45 & -31.6 \\
 & & & & & 39.9 & -24.2 \\
 & & & & & & 2820
\end{pmatrix} \times 10^{-7}
$$

Table C.2: Covariance matrices for the energies extracted from each ensembles for ρ meson.

As we discussed in Section 3.5, to determine resonance parameters by fitting a functional description to our phase shifts we need to take into account cross-correlations between the extracted energies. The energies extracted from different ensembles are uncorrelated, but there will be correlations between the levels extracted from the same ensemble. We computed these covariance matrices using a jackknife procedure. These matrices are listed in Table C.2. In the left column from top down we list the ensembles $\mathcal{E}_{1,2,3}$ corresponding to $m_\pi \approx 315\,\mathrm{MeV}$ and on the right $\mathcal{E}_{4,5,6}$ corresponding to $m_\pi \approx 226\,\mathrm{MeV}$. The order of the levels in each matrix corresponds to the order they appear in Table C.1.

C.2 $\quad \sigma$ meson

In this section we list the fit result and the corresponding fit quality for each energy level and for each ensemble in Table C.3. In this table, d stands for the time interval of shifted correlator. In the rest frame ($\boldsymbol{P} = (0,0,0)$), we need to have $d \neq 0$ to subtract the vacuum contribution. In the boost frame where the total momentum in

our study is $\boldsymbol{P} = (0,0,1)$, we use the normal correlator to extract the energy spectrum. Therefore, we set the d to zero in this case. The definition of χ^2/dof and Q is the same as in Table C.1.

m_π(MeV)	$\boldsymbol{P}$	η	n	d	t_0	fit window	aE	χ^2/dof	Q
315	$(0,0,0)$	1.0	1	2	2	$3-13$	0.355(9)	0.99	0.44
			2	2	2	$2-8$	0.54(3)	0.89	0.47
			3	2	2	$2-7$	0.66(2)	0.91	0.44
		1.25	1	2	2	$3-12$	0.363(15)	0.92	0.49
			2	2	2	$2-8$	0.50(2)	0.88	0.47
			3	2	2	$2-9$	0.59(2)	0.86	0.48
		2.0	1	2	2	$4-21$	0.378(7)	1.02	0.43
			2	2	2	$2-7$	0.457(8)	1.05	0.37
			3	2	2	$3-9$	0.54(2)	0.84	0.50
	$(0,0,1)$	1.0	1	0	2	$2-9$	0.492(5)	0.27	0.93
			2	0	2	$2-7$	0.693(3)	0.46	0.71
		1.25	1	0	2	$4-13$	0.447(16)	1.4	0.20
			2	0	2	$2-8$	0.60(3)	0.65	0.62
		2.0	1	0	2	$4-21$	0.410(2)	0.70	0.77
			2	0	2	$4-8$	0.54(2)	0.92	0.40
			3	0	2	$2-6$	0.60(1)	0.07	0.93
226	$(0,0,0)$	1.0	1	3	3	$3-14$	0.256(2)	0.97	0.46
			2	3	3	$2-9$	0.48(3)	0.98	0.43
			3	3	3	$3-11$	0.60(2)	1.03	0.40
		1.17	1	3	3	$4-13$	0.256(3)	0.23	0.98
			2	3	3	$2-8$	0.44(3)	0.61	0.65
			3	3	3	$2-6$	0.54(2)	0.37	0.69
		1.33	1	3	3	$2-15$	0.264(2)	0.77	0.68
			2	3	3	$2-14$	0.44(1)	0.28	0.99
			3	3	3	$2-8$	0.53(2)	0.78	0.54
	$(0,0,1)$	1.0	1	0	2	$5-15$	0.409(7)	0.09	0.91
			2	0	2	$2-8$	0.59(3)	0.81	0.51
		1.17	1	0	2	$6-17$	0.379(5)	0.81	0.60
			2	0	2	$3-8$	0.575(16)	1.08	0.36
		1.33	1	0	2	$4-15$	0.353(3)	0.38	0.94
			2	0	2	$3-11$	0.55(3)	0.38	0.94
			3	0	2	$3-9$	0.648(4)	1.08	0.36

Table C.3: Extracted energies and fitting details for σ meson.

Similar to the ρ meson case, we compute the covariance matrices and list them in Table C.4. In the left column we list the ensembles $\mathcal{E}_{1,2,3}$ (ordered from top down) corresponding to $m_\pi \approx 315\,\text{MeV}$ and on the right $\mathcal{E}_{4,5,6}$ corresponding to $m_\pi \approx 226\,\text{MeV}$. The order of the levels in each matrix corresponds to the order they appear in Table C.3.

$$\begin{pmatrix} 75.1 & -29.4 & -7.2 & -2.37 & -7.14 \\ & 1137 & 653.6 & -23.2 & 63.6 \\ & & 1345 & -6.37 & 30.3 \\ & & & 57.6 & 116.5 \\ & & & & 1025.1 \end{pmatrix} \times 10^{-6} \qquad \begin{pmatrix} 5.19 & -7.5 & 5.97 & 1.29 & -4.27 \\ & 806.6 & 377.4 & -5.84 & -60.0 \\ & & 1068 & -7.43 & -44.4 \\ & & & 56.5 & -37.9 \\ & & & & 790 \end{pmatrix} \times 10^{-6}$$

$$\begin{pmatrix} 193 & -37.2 & -56.3 & 16.13 & -7.89 \\ & 1130 & 1253 & -11.1 & -67.4 \\ & & 2848 & -8.55 & 61.8 \\ & & & 414.0 & 265.5 \\ & & & & 1552 \end{pmatrix} \times 10^{-6} \qquad \begin{pmatrix} 7.06 & -2.64 & 0.601 & 0.561 & 1.65 \\ & 820.5 & 403.6 & -2.34 & -49.2 \\ & & 432 & 3.13 & -38.6 \\ & & & 17.5 & -12.8 \\ & & & & 465.5 \end{pmatrix} \times 10^{-6}$$

$$\begin{pmatrix} 163.8 & -70.4 & 156.6 & -1.003 & -2.66 & -5.65 \\ & 137.6 & 117.6 & 1.57 & -0.846 & -0.682 \\ & & 966.1 & -0.226 & 30.8 & -29.6 \\ & & & 10.4 & 14.6 & 2.95 \\ & & & & 479.6 & -51.8 \\ & & & & & 104.2 \end{pmatrix} \times 10^{-6} \qquad \begin{pmatrix} 2.31 & 5.24 & 1.23 & 0.868 & 1.91 & -0.118 \\ & 373.5 & 263.8 & 3.78 & -38.1 & -2.20 \\ & & 513.2 & 0.927 & -16.04 & -3.33 \\ & & & 7.63 & 4.31 & 1.39 \\ & & & & 1648 & 26.04 \\ & & & & & 15.6 \end{pmatrix} \times 10^{-6}$$

Table C.4: Covariance matrices for the energies extracted from each ensembles for σ meson.

Bibliography

[1] J. R. Pelaez, *Phys. Rept.* **658** (2016) 1, [arXiv:1510.0065].

[2] M. Döring, B. Hu, and M. Mai, [arXiv:1610.1007].

[3] R. A. Briceno, J. J. Dudek, R. G. Edwards, and D. J. Wilson, *Phys. Rev. Lett.* **118** (2017), no. 2 022002, [arXiv:1607.0590].

[4] S. D. Protopopescu, M. Alston-Garnjost, A. Barbaro-Galtieri, S. M. Flatte, J. H. Friedman, T. A. Lasinski, G. R. Lynch, M. S. Rabin, and F. T. Solmitz, *Phys. Rev.* **D7** (1973) 1279.

[5] R. R. Akhmetshin *et. al.* (**CMD-2** Collaboration), *Phys. Lett.* **B648** (2007) 28–38, [hep-ex/0610021].

[6] C. Patrignani *et. al.* (**Particle Data Group** Collaboration), *Chin. Phys.* **C40** (2016), no. 10 100001.

[7] S. Aoki *et. al.* (**PACS** Collaboration), *Phys. Rev.* **D84** (2011) 094505, [arXiv:1106.5365].

[8] M. Göckeler, R. Horsley, Y. Nakamura, D. Pleiter, P. E. L. Rakow, G. Schierholz, and J. Zanotti (**QCDSF** Collaboration), *PoS* **LATTICE2008** (2008) 136, [arXiv:0810.5337].

[9] X. Feng, K. Jansen, and D. B. Renner, *Phys.Rev.* **D83** (2011) 094505, [arXiv:1011.5288].

[10] C. Lang, D. Mohler, S. Prelovsek, and M. Vidmar, *Phys.Rev.* **D84** (2011), no. 5 054503, [arXiv:1105.5636].

[11] C. Pelissier and A. Alexandru, *Phys.Rev.* **D87** (2013), no. 1 014503, [arXiv:1211.0092].

[12] G. S. Bali, S. Collins, A. Cox, G. Donald, M. Göckeler, C. B. Lang, and A. Schäfer, [arXiv:1512.0867].

[13] J. Frison *et. al.* (**Budapest-Marseille-Wuppertal** Collaboration), *PoS* **LATTICE2010** (2010) 139, [arXiv:1011.3413].

[14] J. J. Dudek, R. G. Edwards, and C. E. Thomas (**Hadron Spectrum** Collaboration), *Phys.Rev.* **D87** (2013), no. 3 034505, [arXiv:1212.0830].

[15] T. Metivet (**Budapest-Marseille-Wuppertal** Collaboration), *PoS* **LATTICE2014** (2015) 079, [arXiv:1410.8447].

[16] D. J. Wilson, R. A. Briceño, J. J. Dudek, R. G. Edwards, and C. E. Thomas, [arXiv:1507.0259].

[17] J. Bulava, B. Fahy, B. Hörz, K. J. Juge, C. Morningstar, and C. H. Wong, *Nucl. Phys.* **B910** (2016) 842–867, [arXiv:1604.0559].

[18] C. Alexandrou, L. Leskovec, S. Meinel, J. Negele, S. Paul, M. Petschlies, A. Pochinsky, G. Rendon, and S. Syritsyn, *Phys. Rev.* **D96** (2017), no. 3 034525, [arXiv:1704.0543].

[19] M. Gell-Mann and M. Levy, *Nuovo Cim.* **16** (1960) 705.

[20] M. G. Alford and R. L. Jaffe, *Nucl. Phys.* **B578** (2000) 367–382, [`hep-lat/0001023`].

[21] N. Mathur, A. Alexandru, Y. Chen, S. J. Dong, T. Draper, I. Horváth, F. X. Lee, K. F. Liu, S. Tamhankar, and J. B. Zhang, *Phys. Rev. D* **76** (Dec, 2007) 114505.

[22] S. Prelovsek, T. Draper, C. B. Lang, M. Limmer, K.-F. Liu, N. Mathur, and D. Mohler, *Phys. Rev. D* **82** (Nov, 2010) 094507.

[23] Z. Fu, *JHEP* **07** (2012) 142, [`arXiv:1202.5834`].

[24] M. Wakayama, T. Kunihiro, S. Muroya, A. Nakamura, C. Nonaka, M. Sekiguchi, and H. Wada, *Phys. Rev.* **D91** (2015), no. 9 094508, [`arXiv:1412.3909`].

[25] K. G. Wilson, *Phys. Rev. D* **10** (Oct, 1974) 2445–2459.

[26] H. J. Rothe, *Lattice Gauge Theories an introduction.* World Scientific, 2005.

[27] C. Gattringer and C. B. Lang, *Quantum Chromodynamics on the lattice.* Springer, 2010.

[28] T. DeGrand, *Lattice Methods for Quantum Chromodynamics.* World Scientific, 2006.

[29] *Hadronic Physics from Lattice QCD.* World Scientific, 2004.

[30] P. A. Dirac, *Physikalische Zeitschrift der Sowjetunion. 3: 64–72* (1933).

[31] R. P. Feynman and A. R. Hibbs, *Quantum Mechanics and Path Integrals.* New York: McGraw-Hill, 1965.

[32] K. G. Wilson, in *New Phenomena in Subnuclear Physics: Proceedings, International School of Subnuclear Physics, Erice, Sicily, Jul 11-Aug 1 1975. Part A*, p. 99, 1975. [,0069(1975)].

[33] K. Symanzik, *Nucl. Phys.* **B226** (1983) 187–204.

[34] B. Sheikholeslami and R. Wohlert, *Nucl. Phys.* **B259** (1985) 572.

[35] M. Luscher and P. Weisz, *Nucl. Phys.* **B479** (1996) 429–458, [`hep-lat/9606016`].

[36] M. Luscher, S. Sint, R. Sommer, and P. Weisz, *Nucl. Phys.* **B478** (1996) 365–400, [`hep-lat/9605038`].

[37] G. P. Lepage and P. B. Mackenzie, *Phys. Rev.* **D48** (1993) 2250–2264, [`hep-lat/9209022`].

[38] R. Hoffmann, A. Hasenfratz, and S. Schaefer, *PoS* **LAT2007** (2007) 104, [`arXiv:0710.0471`].

[39] M. Lüscher and P. Weisz, *Commun.Math.Phys.* **97** (1985) 59.

[40] M. G. Alford, W. Dimm, G. Lepage, G. Hockney, and P. Mackenzie, *Phys.Lett.* **B361** (1995) 87–94, [`hep-lat/9507010`].

[41] A. Hasenfratz and F. Knechtli, *Phys. Rev.* **D64** (2001) 034504, [`hep-lat/0103029`].

[42] M. Albanese *et. al.* (**APE** Collaboration), *Phys. Lett.* **B192** (1987) 163–169.

[43] L. Lellouch, R. Sommer, B. Svetitsky, A. Vladikas, and L. F. Cugliandolo, eds., *Modern perspectives in lattice QCD: Quantum field theory and high performance computing. Proceedings, International School, 93rd Session, Les Houches, France, August 3-28, 2009*, 2011.

[44] M. Luscher, in *Modern perspectives in lattice QCD: Quantum field theory and high performance computing. Proceedings, International School, 93rd Session, Les Houches, France, August 3-28, 2009*, pp. 331–399, 2010, [`arXiv:1002.4232`].

[45] N. Metropolis, A. W. Rosenbluth, M. N. Rosenbluth, A. H. Teller, and E. Teller, *The Journal of Chemical Physics* **21** (1953), no. 6 1087–1092, [https://doi.org/10.1063/1.1699114].

[46] W. K. Hastings, *Biometrika* (1970) 97–109.

[47] S. Duane, A. Kennedy, B. Pendleton, and D. Roweth, *Phys.Lett.* **B195** (1987) 216–222.

[48] A. Hasenfratz, R. Hoffmann, and S. Schaefer, *JHEP* **0705** (2007) 029, [hep-lat/0702028].

[49] M. Hamermesh, *Group Theory and its Application to Physical Problems*. Dover Publication, Inc., 1989.

[50] M. Peardon, J. Bulava, J. Foley, C. Morningstar, J. Dudek, R. G. Edwards, B. Joo, H.-W. Lin, D. G. Richards, and K. J. Juge (**Hadron Spectrum** Collaboration), *Phys. Rev.* **D80** (2009) 054506, [arXiv:0905.2160].

[51] C. Morningstar, J. Bulava, J. Foley, K. J. Juge, D. Lenkner, *et. al.*, *Phys.Rev.* **D83** (2011) 114505, [arXiv:1104.3870].

[52] M. Lüscher and U. Wolff, *Nucl.Phys.* **B339** (1990) 222–252.

[53] B. Blossier, M. Della Morte, G. von Hippel, T. Mendes, and R. Sommer, *JHEP* **0904** (2009) 094, [arXiv:0902.1265].

[54] T. A. DeGrand and D. Toussaint, eds., *From actions to answers. Proceedings, Theoretical Advanced Study Institute in Elementary Particle Physics, Boulder, USA, June 5-30, 1989*, 1990.

[55] B. Efron, *Ann. Statist.* **7** (01, 1979) 1–26.

[56] R. G. MILLER, *Biometrika* **61** (1974), no. 1 1–15.

[57] L. Maiani and M. Testa, *Phys. Lett.* **B245** (1990) 585–590.

[58] L. Lellouch and M. Luscher, *Commun. Math. Phys.* **219** (2001) 31–44, [hep-lat/0003023].

[59] M. Lüscher, *Nucl.Phys.* **B354** (1991) 531–578.

[60] X. Feng, X. Li, and C. Liu, *Phys.Rev.* **D70** (2004) 014505, [hep-lat/0404001].

[61] K. Rummukainen and S. A. Gottlieb, *Nucl. Phys.* **B450** (1995) 397–436, [hep-lat/9503028].

[62] F. J. Yndurain, R. Garcia-Martin, and J. R. Pelaez, *Phys. Rev.* **D76** (2007) 074034, [hep-ph/0701025].

[63] I. Caprini, *Phys. Rev.* **D77** (2008) 114019, [arXiv:0804.3504].

[64] J. Gasser and H. Leutwyler, *Annals Phys.* **158** (1984) 142.

[65] J. Gasser and H. Leutwyler, *Nucl. Phys.* **B250** (1985) 465–516.

[66] M. Doring, U.-G. Meissner, E. Oset, and A. Rusetsky, *Eur. Phys. J.* **A47** (2011) 139, [arXiv:1107.3988].

[67] J. J. Dudek, R. G. Edwards, and C. E. Thomas, *Phys.Rev.* **D86** (2012) 034031, [arXiv:1203.6041].

[68] D. C. Moore and G. T. Fleming, *Phys.Rev.* **D73** (2006) 014504, [hep-lat/0507018].

[69] B. B. Brandt, A. Jüttner, and H. Wittig, *JHEP* **11** (2013) 034, [arXiv:1306.2916].

[70] P. Fritzsch, F. Knechtli, B. Leder, M. Marinkovic, S. Schaefer, R. Sommer, and F. Virotta, *Nucl. Phys.* **B865** (2012) 397–429, [arXiv:1205.5380].

[71] M. Lüscher, *JHEP* **1008** (2010) 071, [`arXiv:1006.4518`].

[72] S. Borsanyi, S. Durr, Z. Fodor, C. Hoelbling, S. D. Katz, *et. al.*, [`arXiv:1203.4469`].

[73] M. Bruno and R. Sommer (**ALPHA** Collaboration), *PoS* **LATTICE2013** (2014) 321, [`arXiv:1311.5585`].

[74] R. Sommer, *Nucl.Phys.* **B411** (1994) 839–854, [`hep-lat/9310022`].

[75] Y.-B. Yang, Y. Chen, A. Alexandru, S.-J. Dong, T. Draper, *et. al.*, [`arXiv:1410.3343`].

[76] Y. Aoki *et. al.* (**RBC, UKQCD** Collaboration), *Phys. Rev.* **D83** (2011) 074508, [`arXiv:1011.0892`].

[77] A. Walker-Loud, *PoS* **LATTICE2008** (2008) 005, [`arXiv:0810.0663`].

[78] S. Durr, Z. Fodor, C. Hoelbling, S. Katz, S. Krieg, *et. al.*, *JHEP* **1108** (2011) 148, [`arXiv:1011.2711`].

[79] S. Prelovsek and D. Mohler, *Phys. Rev.* **D79** (2009) 014503, [`arXiv:0810.1759`].

[80] D. Guo, A. Alexandru, R. Molina, and M. Döring, *Phys. Rev.* **D94** (2016), no. 3 034501, [`arXiv:1605.0399`].

[81] F. von Hippel and C. Quigg, *Phys. Rev. D* **5** (Feb, 1972) 624–638.

[82] P. C. Bruns and U.-G. Meissner, *Eur. Phys. J.* **C40** (2005) 97–119, [`hep-ph/0411223`].

[83] Y. Chen, A. Alexandru, T. Draper, K.-F. Liu, Z. Liu, and Y.-B. Yang, [`arXiv:1507.0254`].

[84] B. Hu, R. Molina, M. Döring, and A. Alexandru, *Phys. Rev. Lett.* **117** (2016), no. 12 122001, [`arXiv:1605.0482`].

[85] J. R. Pelaez and G. Rios, *Phys. Rev.* **D82** (2010) 114002, [`arXiv:1010.6008`].

[86] K. A. Olive *et. al.* (**Particle Data Group** Collaboration), *Chin. Phys.* **C38** (2014) 090001.

[87] R. A. Briceno, J. J. Dudek, R. G. Edwards, and D. J. Wilson, [`arXiv:1708.0666`].

[88] X. Li and C. Liu, *Phys.Lett.* **B587** (2004) 100–104, [`hep-lat/0311035`].

[89] T. N. Truong, *Phys. Rev. Lett.* **61** (1988) 2526.

[90] A. Dobado, M. J. Herrero, and T. N. Truong, *Phys. Lett.* **B235** (1990) 134.

[91] A. Dobado and J. R. Pelaez, *Phys. Rev.* **D47** (1993) 4883–4888, [`hep-ph/9301276`].

[92] A. Dobado and J. R. Pelaez, *Phys. Rev.* **D56** (1997) 3057–3073, [`hep-ph/9604416`].

[93] J. Nebreda and J. R. Pelaez., *Phys. Rev.* **D81** (2010) 054035, [`arXiv:1001.5237`].

[94] J. A. Oller, E. Oset, and J. R. Pelaez, *Phys. Rev.* **D59** (1999) 074001, [`hep-ph/9804209`]. [Erratum: Phys. Rev.D75,099903(2007)].

[95] M. Doring, J. Haidenbauer, U.-G. Meissner, and A. Rusetsky, *Eur. Phys. J.* **A47** (2011) 163, [`arXiv:1108.0676`].

[96] M. Doring, C. Hanhart, F. Huang, S. Krewald, and U. G. Meissner, *Phys. Lett.* **B681** (2009) 26–31, [`arXiv:0903.1781`].

[97] A. Martinez Torres, L. R. Dai, C. Koren, D. Jido, and E. Oset, *Phys. Rev.* **D85** (2012) 014027, [arXiv:1109.0396].

[98] M. Doring, U. G. Meissner, E. Oset, and A. Rusetsky, *Eur. Phys. J.* **A48** (2012) 114, [arXiv:1205.4838].

[99] M. Döring, U.-G. Meißner, and W. Wang, *JHEP* **10** (2013) 011, [arXiv:1307.0947].
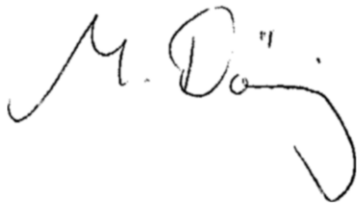
Thesis Endorsement

References

- D. Guo, A. Alexandru, R. Molina and M. Doering. *Rho Resonance Parameters from Lattice QCD*, **Phys. Rev. D 94, 034501**

I certify that the contribution of Dehua Guo to these works was substantial and original.

I agree to his including materials from these works in present thesis.

Author:

Date:

1/5/2018

Andrei Alexandru

Thesis Endorsement

References

- D. Guo, A. Alexandru, R. Molina and M. Doering. *Rho Resonance Parameters from Lattice QCD*, **Phys. Rev. D 94, 034501**

I certify that the contribution of Dehua Guo to these works was substantial and original.

I agree to his including materials from these works in present thesis.

Author: Date: January 4, 2018

Michael Doering

Thesis Endorsement

References

- D. Guo, A. Alexandru, R. Molina and M. Doering. *Rho Resonance Parameters from Lattice QCD*, **Phys. Rev. D 94, 034501**

I certify that the contribution of Dehua Guo to these works was substantial and original.

I agree to his including materials from these works in present thesis.

Author: Date: 01/07/2018

Raquel Molina